Master's Thesies

Performance of Pion, Kaon and Proton Identification with the Ring Imaging Čerenkov Counter of HERMES

Kentaro Suetsugu

February 2001

Abstract

HERMES is an experiment which is designed to study the spin structure of the nucleon using HERA storage ring at the DESY laboratory in Hamburg, Germany. A polarized electron(positron) beam in the storage ring is scattered on the internal gas targets(H,He,D). The beam energy is 27.5 GeV/c. One of the aims of this experiment is to extract the polarization of quarks in the nucleon by measuring the spin asymmetries of hadron production in deep-inelastic scattering(DIS).

In order to study the strange quark distribution function in particular, it is necessary to identify kaons which consist of strange quarks (e.g. $K^+(u\bar{s})$,$K^-(\bar{u}s)$). The Ring Imaging Čerenkov Counter (RICH) of HERMES is designed to identify hadrons produced in DIS in the momentum range of 2-15 GeV/c. The HERMES RICH is a dual radiator RICH. The radiators are the C_4F_{10} gas and the silica aerogel. The refractive index of the C_4F_{10} gas is $n_{\rm gas} = 1.00137$. Very strong conditions on the uniformity of the refractive index of the aerogel are required in order to successfully use it for RICH. The measured refractive index of the aerogel is $n_{\rm aerogel} = 1.0303$ and its standard deviation of the tile-to-tile difference is 2.5×10^{-4}. These values satisfy the requirements to evaluate the Čerenkov angle. The RICH with aerogel is used for the first time in an actual experiment at HERMES.

We have upgraded the Monte Carlo(MC) simulation. The Čerenkov photons are refracted at the boundary between the aerogel and the C_4F_{10} gas. Because of the difference of the refractive indices of the two radiators, the Čerenkov angle is measured to be larger than the predicted value. The effect of the refraction at the boundary is taken into account. The other improvements are as follows: properties of the aerogel, the reflectivity of the mirror and the detection efficiency of photon detectors. After MC was upgraded, the Čerenkov angle θ, its resolution σ and the number of detected photons N agree with experimental results. θ, σ and N are essential quantities to perform the particle identification (PID).

Particle types of hadrons ($\pi^{\pm}, {\rm K}^{\pm}, {\rm p}(\bar{\rm p})$) are identified with algorithm using a likelihood technique. A likelihood L_h for each of the hypothesis $h = \pi, {\rm K}, {\rm p}$ is calculated based on the number of detected photons N and the Čerenkov angle θ. The PID performance is evaluated from the point of view of the "efficiency" and "purity". The efficiency and purity can be determined from MC and decaying particle analysis ($\phi \to K^+K^-$, $\rho \to \pi^+\pi^-$, $\Lambda \to p\pi^-$, etc.). The efficiencies studied with both analysis methods are consistent.

This analysis provides a firm basis on how to extract the spin asymmetries of true hadrons from the measured asymmetries.

Contents

1 Introduction **3**
- 1.1 Deep Inelastic Scattering (DIS) . . . 3
- 1.2 The Unpolarized Cross-Section . . . 4
- 1.3 The Polarized Cross-Section . . . 5
- 1.4 Cross-Section Asymmetries . . . 6
- 1.5 Semi-Inclusive Measurement of Deep Inelastic Scattering . . . 8

2 The HERMES Experiment **10**
- 2.1 The HERA Storage Ring . . . 11
- 2.2 The HERMES Targets . . . 11
- 2.3 The HERMES Spectrometer . . . 12
  - 2.3.1 Tracking Systems . . . 13
  - 2.3.2 Particle Identification Method for Lepton-Hadron Separation 14

3 The Ring Imaging Čerenkov Counter (RICH) **18**
- 3.1 Čerenkov Counter . . . 18
- 3.2 The RICH Counter of HERMES . . . 20
  - 3.2.1 Components and Geometry . . . 21
  - 3.2.2 Characteristics of Silica Aerogel . . . 24
  - 3.2.3 Mirrors . . . 31
  - 3.2.4 Photon Detectors and Readout System . . . 31
- 3.3 The Monte Carlo Simulation for the RICH . . . 33
  - 3.3.1 RICH Improvements in HMC . . . 34
  - 3.3.2 Effects of the RICH Apparatus Included in HMC . . . 36
- 3.4 Čerenkov Angle Resolutions and the Number of Fired PMTs after MC Upgraded . . . 39
- 3.5 Results of DIS MC Production . . . 43

4 Particle Identification with the HERMES RICH **44**
- 4.1 Geometry and Basic Principles . . . 46
- 4.2 Identification Methods . . . 47
- 4.3 Likelihood Technique . . . 51
  - 4.3.1 IRT Likelihood Algorithm . . . 52
  - 4.3.2 DRT Likelihood Algorithm . . . 53
  - 4.3.3 Quality Parameter . . . 54

5 The Performance of the Čerenkov Ring Reconstruction 55
5.1 The Performance of the Experimental Data 56
5.2 The Performance of the MC Simulation 66

6 PID Efficiency and Purity 69
6.1 How to Calculate P- and Q- Matrix 69
6.1.1 General Formalism 70
6.1.2 Monte Carlo Analysis 71
6.1.3 Decaying Particle Analysis 72
6.2 Unfolding the Counts of Identified Hadrons 72
6.3 PID Efficiency and Purity Study with MC 73
6.3.1 PID Efficiency from MC Data 73
6.3.2 Factors Influencing PID Efficiency 74
6.4 Purity from MC 81
6.5 Comparison of MC and Experimental Results 83
6.5.1 PID Efficiency from Decaying Particle Analysis 83
6.5.2 Comparison of DIS MC and Decaying Particle Analysis for Efficiency 84

7 Interpretation of the Results 87
7.1 Dips at the Čerenkov Thresholds 87
7.2 Disagreement between MC and Decaying Particle Analysis 88
7.3 Relation of the P- and Q-matrix via the Flux Factor 89
7.4 Advantage of the Q-matrix 90

8 Summary 92

A Statistical Error of P- and Q- Matrix 95

B Projected Performance of the RICH 96

C Momentum Distributions of the Statistics for the Two Binnings 100

D Difference Between Positive and Negative Charged Particles 103

E Momentum Distributions of the Efficiencies 105

F Momentum Distributions of the Q-matrix 107

G Comparison DIS MC and Decaying Particle Analysis 110

Chapter 1

Introduction

1.1 Deep Inelastic Scattering (DIS)

Deep inelastic scattering (DIS) has played an essential role in the study of quarks and gluons. The lepton and hadron scattering with high momentum transfer produces one or more hadrons. Hence, it is described as:

$$e + N \rightarrow e' + h + X \tag{1.1}$$

where e is the initial lepton, N is the target nucleon and e' is the scattered lepton, h is one or more hadrons, X other hadrons.

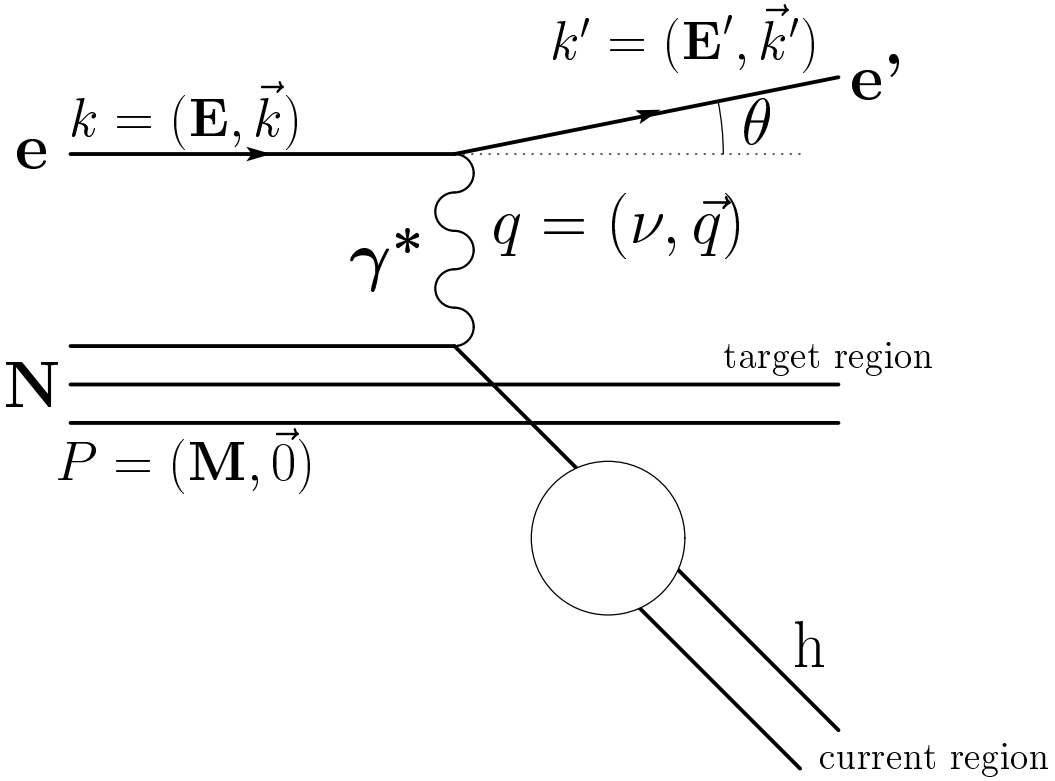

Figure 1.1: Diagram of a deep inelastic scattering.

Fig.(1.1) describes a schematic diagram of deep inelastic scattering. The initial lepton has four-momentum k and the final lepton has k'. Assuming one photon exchange with the nucleon as a target, the differential cross section for the final lepton detected in the solid angle $d\Omega$ and in the final energy range $(E, E' + dE')$ is written as

$$\frac{d^2\sigma}{d\Omega dE'} = \frac{\alpha 2}{2Mq^4}\frac{E'}{E}L_{\mu\nu}W^{\mu\nu} \tag{1.2}$$

where $q = k - k'$ and α is the fine structure constant. The other kinematic variables are summarized bellow:

$$\begin{aligned}
&Q^2 = -\boldsymbol{q}^2 = -(\boldsymbol{k} - \boldsymbol{k}') \simeq 4EE' \sin^2\frac{\theta}{2} && \\
&\nu = \frac{\vec{P}\cdot\vec{q}}{M} = E - E' && \text{energy transfer} \\
&x = -\frac{\vec{q}^2}{2\vec{P}\cdot\vec{q}} = \frac{Q^2}{2M\nu} && \text{momentum fraction} \\
&y = \frac{\vec{P}\cdot\vec{q}}{\vec{P}\cdot\vec{k}} = \frac{\nu}{E} && \text{energy fraction} \\
&W^2 = (\vec{P} + \vec{q})^2 = M^2 + 2M\nu - Q^2 && \text{invariant mass for the final state hadrons}
\end{aligned} \tag{1.3}$$

1.2 The Unpolarized Cross-Section

The inclusive DIS cross-section can be expressed in terms of the lepton and hadron tensors, $L^{\mu\nu}$ and $W_{\mu\nu}$:

$$\frac{d^2\sigma}{d\Omega dE'} = \frac{\alpha^2}{Q^4}\frac{E'}{E}L^{\mu\nu}W_{\mu\nu} \tag{1.4}$$

where $\alpha = \frac{1}{137.04}$ is the fine structure constant. The lepton tensor is calculated from the spinors according to the Feynman rules:

$$L^{\mu\nu} = \sum_{s_l'}(\bar{u}(k', s_l')\gamma^\mu u(k, s_l)) \cdot (\bar{u}(k, s_l)\gamma^\nu u(k', s_l')) \tag{1.5}$$

When the beam and target are unpolarized, the initial spins s_l are averaged and the leptonic tensor becomes:

$$L^{\mu\nu} = 2\left[k^{\mu'}k^\nu + k^\mu k^{\nu'} + (m_e^2 - k\cdot k')g^{\mu\nu}\right] \tag{1.6}$$

where m_e is the electron mass and can be neglected. $g^{\mu\nu}$ is the metric tensor. The hadronic tensor reflects the structure of the nucleon and can be reduced to two real functions, W_1 and W_2:

$$W_{\mu\nu} = W_1(Q^2, \nu)(-g_{\mu\nu} + \frac{q_\mu q_\nu}{q^2}) + \frac{W_2(Q_2, \nu)}{M^2}(p_\mu - \frac{p\cdot q}{q^2}q_\mu)(p_\nu - \frac{p\cdot q}{q^2}q_\nu) \tag{1.7}$$

If we introduce dimensionless structure functions:

$$F_1(x, Q^2) = MW_1(Q^2, \nu) \tag{1.8}$$

$$F_2(x, Q^2) = \nu W_2(Q^2, \nu) \tag{1.9}$$

The unpolarized cross-section becomes:

$$\frac{d^2\sigma}{d\Omega dE'} = \frac{4\pi\alpha^2}{Q^4} \cdot \left\{ y^2 F_1(x, Q^2) + \left(1 - y - \frac{Mxy}{2E}\right) \frac{F_2(x, Q^2)}{x} \right\} \tag{1.10}$$

The measurement of the structure functions of proton reveals that they depend only very weakly on Q^2, which is called Bjorken scaling. This indicates that proton consists of point like sub-particles called partons. Furthermore, the Callen-Gross relation

$$F_2(x) = 2xF_1(x) \tag{1.11}$$

is measured to be valid to high degree. This relation is a direct consequence of the spin-$\frac{1}{2}$ property of the quarks inside the proton because the relation is only true for the scattering of point-like spin-$\frac{1}{2}$ particles by exchange of a vector boson.

The unpolarized cross-section can alternatively be described in terms of absorption cross-section for longitudinally σ_L and transversely σ_T polarized photons:

$$\frac{d^2\sigma}{d\Omega dE'} = \Gamma \left(\sigma_T + \epsilon\sigma_L\right) \tag{1.12}$$

Γ denotes the flux of virtual photons.

1.3 The Polarized Cross-Section

Consider the deep inelastic scattering of polarized leptons and polarized nucleons. The polarized cross-section contains additional terms in order to take into account the azimuthal angle ϕ:

$$\frac{d^3\sigma}{d\cos\theta d\phi dE'} = \frac{\alpha^2}{Q^4}\frac{E'}{E} L^{\mu\nu} W_{\mu\nu} \tag{1.13}$$

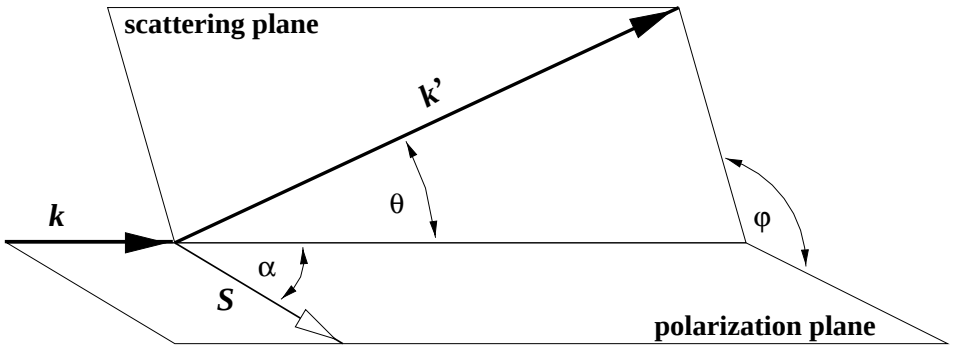

Figure 1.2: Scattering angles in polarized DIS. The four-momentum vectors, k and k' are for the incident and scattered leptons. The angles θ, ϕ and α are defined as the angles between k and k'.

The lepton tensor in Eq.(1.5) becomes:

$$L^{\mu\nu} = 2\left[k^{\mu'}k^{\nu} + k^{\mu}k^{\nu'} - k\cdot k' g^{\mu\nu} - i\epsilon^{\mu\nu\alpha\beta}q_{\alpha}s_{l\,\beta}\right] \tag{1.14}$$

where $s_{l\,\beta}$ is the spin four-vector of the incoming lepton and $\epsilon^{\mu\nu\alpha\beta}$ is the totally anti-asymmetric Levi-Civita tensor. The general form of the hadronic tensor in the polarized case is

$$\begin{aligned} W_{\mu\nu} &= W_1(Q^2,\nu)(-g_{\mu\nu} + \frac{q_\mu q_\nu}{q^2}) + \frac{W_2(Q^2,\nu)}{M^2}(p_\mu - \frac{p\cdot q}{q^2}q_\mu)(p_\nu - \frac{p\cdot q}{q^2}q_\nu) \\ &\quad + G_1(Q^2,\nu)Mi\epsilon_{\mu\nu\lambda\sigma}q^{\lambda}s_h^{\sigma} + \frac{G_2(Q^2,\nu)}{M}i\epsilon_{\mu\nu\lambda\sigma}q^{\lambda}(p\cdot q s_h^{\sigma} - s_h\cdot q p^{\sigma}) \end{aligned} \tag{1.15}$$

where s_h is the axial polarized vector of a spin-$\frac{1}{2}$ target. Because of the symmetries of the leptonic and hadronic tensors, the polarization asymmetry of the cross-section is completely determined by the anti-asymmetric part of $W_{\mu\nu}$.

In analogy to the unpolarized case, two dimensionless spin structure functions are introduced:

$$g_1(x,Q^2) = M^2\nu G_1(Q^2,\nu) \tag{1.16}$$

$$g_s(x,Q^2) = M\nu^2 G_2(Q^2,\nu) \tag{1.17}$$

With these definitions, the spin-dependent part of the polarized DIS cross-section is given by

$$\begin{aligned} \frac{d^3\left(\sigma(\alpha) - \sigma(\pi+\alpha)\right)}{dxdyd\phi} &= \frac{e^4}{4\pi^2Q^2}\left[\cos\alpha\left(\left[1 - \frac{y}{2} - \frac{y^2}{4}\gamma^2\right]g_1(x,Q^2) - \frac{y}{2}\gamma^2 g_2(x,Q^2)\right)\right. \\ &\quad \left. - \sin\alpha\cos\phi\sqrt{\gamma^2\left[1 - y - \frac{y^2}{4}\gamma^2\right]}\left(\frac{y}{2}g_1(x,Q^2) + g_2(x,Q^2)\right)\right] \end{aligned} \tag{1.18}$$

where γ is defined as $\gamma = \sqrt{Q^2}/\nu$ and α is defined in Fig.(1.2).

1.4 Cross-Section Asymmetries

The experimentaly measured asymmetries $A_{\parallel}$ and $A_{\perp}$ are obtained by reversing the spin of the longitudnally and transversely polarized target:

$$A_{\parallel} = \frac{\sigma^{\uparrow\downarrow} - \sigma^{\uparrow\uparrow}}{\sigma^{\uparrow\downarrow} + \sigma^{\uparrow\uparrow}} \tag{1.19}$$

$$A_{\perp} = \frac{\sigma^{\uparrow\rightarrow} - \sigma^{\uparrow\leftarrow}}{\sigma^{\uparrow\rightarrow} + \sigma^{\uparrow\leftarrow}} \tag{1.20}$$

These cross-section asymmetries are related to the asymmetries of the virtual photon by

$$A_{\parallel} = \mathcal{D}\cdot(A_1 + \eta\cdot A_2) \tag{1.21}$$

$$A_{\perp} = d\cdot(A_2 - \xi\cdot A_1) \tag{1.22}$$

The kinematic factors are defined as follows:

$$\mathcal{D} = \frac{y(2-y)}{y^2 + 2(1-y(1+R))} \tag{1.23}$$

$$\eta = \frac{2\gamma(1-y)}{2-y} \tag{1.24}$$

$$d = \mathcal{D}\sqrt{\frac{2\epsilon}{1+\epsilon}} \tag{1.25}$$

$$\xi = \eta\frac{1+\epsilon}{2\epsilon} \tag{1.26}$$

where ϵ is the degree of transverse polarization of the virtual photon and $R(x, Q^2)$ is the ratio of cross-section for longitudinally and transversely polarized photons. $\mathcal{D}$ is the depolarization factor, measuring the depolarization of the photon relative to the polarization of the scattered lepton.

A_1 and A_2 have relations to g_1 and g_2. They are written as:

$$A_1 = \frac{g_1 - \gamma^2 g_2}{F_1} \tag{1.27}$$

$$A_2 = \frac{\gamma(g_1 + g_2)}{F_1} \tag{1.28}$$

Eliminating g_2 from Eq.(1.27) and Eq.(1.28) yields the relation between A_1 and the structure function ratio g_1/F_1:

$$A_1 = (1+\gamma^2)\frac{g_1}{F_1} - \gamma A_2 \tag{1.29}$$

Inverting the Eq.(1.22) yields the formula to determine A_1 from measured raw asymmetry $A_{\|}$:

$$A_1 = \frac{A_{\|}}{\mathcal{D}} - \eta A_2 \tag{1.30}$$

Eliminating A_1 from Eq.(1.29) and Eq.(1.30) yields the formula to determine g_1/F_1 from the measured raw asymmetry $A_{\|}$:

$$\frac{g_1}{F_1} = \frac{1}{1+\gamma^2}\left[\frac{A_{\|}}{\mathcal{D}} + (\gamma - \eta)A_2\right] \tag{1.31}$$

Using the relation between F_1 and F_2:

$$\frac{1+R(x,Q^2)}{1+\gamma^2} = \frac{F_2(x,Q^2)}{2xF_1(x,Q^2)} \tag{1.32}$$

where R is the ratio of longitudinal and transverse cross sections: $R = \sigma_L/\sigma_T$, the Eq.(1.31) is replaced by F_2 structure function which has already been measured

with high accuracy. Finally one obtains the formula to determine the g_1 structure function from the measured asymmetry $A_{\parallel}$:

$$g_1 = \frac{F_2}{2x(1+R)}\left[\frac{A_{\parallel}}{\mathcal{D}} + \gamma\frac{y}{2-y}A_2\right] \tag{1.33}$$

The approximate determination of $A_1(x,Q^2)$ and $g_1(x,Q^2)$ by only measuring $A_{\parallel}$ is possible by assuming $\gamma A_2 \simeq 0$.

$$A_1 = \frac{A_{\parallel}}{\mathcal{D}} \tag{1.34}$$

$$g_1 = \frac{F_2}{2x(1+R)}\frac{A_{\parallel}}{\mathcal{D}} \tag{1.35}$$

1.5 Semi-Inclusive Measurement of Deep Inelastic Scattering

In Fig.(1.1), the scattered lepton e' is measured in coincidence with the hadrons h. The scattered lepton has the information of the scattered quark kinematics while the hadrons have the flavor of the struck quark. This kind of flavor tagging works on the statistical basis and requires knowledge of the hadronization.

The quark parton model will be extended by a fragmentation model which allows to relate the appearance of certain hadrons h in the final state to the parton distribution functions for different flavors by so called "fragmentation functions". Fig.(1.1) shows the semi-inclusive measurement of the DIS process. The cross-section of the semi-inclusive measurement with a hadron h in the final state is given by

$$\frac{d^3\sigma_h}{dxdQ^2dz}(x,Q^2,z) = \frac{\sum_q e_q^2(x)D_q^h(z)}{\sum_q e_q^2 q(x)} \cdot \frac{d^2\sigma}{dxdQ^2}(x,Q^2) \tag{1.36}$$

where $D_q^h(z)$ is the fragmentation function defined as the number density to produce a hadron with the energy $z = E_h/\nu$ after a quark of flavor q is struck.

The kinematical variables of semi-inclusive measurements are summarized as:

$$\begin{array}{ll}
z = \dfrac{E_h}{\nu} & \text{Fractional energy of a hadron in lab. frame} \\
\boldsymbol{p}_{\parallel} = \dfrac{\boldsymbol{p}_h\boldsymbol{q}}{\sqrt{\boldsymbol{q}^2}} & \text{Parallel momentum of hadron in } \gamma N \text{ frame} \\
\boldsymbol{p}_T = \boldsymbol{p} - \boldsymbol{p}_{\parallel} & \text{Transverse momentum of hadron in } \gamma N \text{ frame} \\
x_F = \left(\dfrac{2||\boldsymbol{p}^2||}{\sqrt{W^2}}\right)_{c.m.} & \text{Feynman's scaling variable}
\end{array} \tag{1.37}$$

The fragmentation functions do not depend on any kinematical variable characteristics of the inclusive measurement (e.g. x and Q^2). This fact expresses the assumption that the two measurements are independent of each other and is

called factorization. The factorization is a direct consequence of quasi-free partons in the quark parton model. The mean hadron multiplicity n^h per event is calculated as:

$$\frac{d^3n^h}{dxdQ^2dz}(x,Q^2,z) = \frac{\sum_q e_q^2(x)D_q^h(z)}{\sum_q e_q^2 q(x)} \tag{1.38}$$

The measured semi-inclusive asymmetry of a hadron h is defined as

$$A_\parallel^h = \frac{\sigma_h^{\uparrow\downarrow} - \sigma_h^{\uparrow\uparrow}}{\sigma_h^{\uparrow\downarrow} + \sigma_h^{\uparrow\uparrow}} \tag{1.39}$$

Furthermore, we define

$$g_1^h(x,z) = \frac{1}{2}\sum_q e_q^2 D_q^h(z)\Delta q \tag{1.40}$$

and

$$F_2^h(x,z) = 2x\frac{1}{2}\sum_q e_q^2 D_q^h(z)\Delta q \tag{1.41}$$

We can use the relation Eq.(1.31) analogously to derive the relation between the spin asymmetry of the hadron $A_\parallel^h$ and the polarized and unpolarized parton distribution functions using Eq.(1.40) and Eq.(1.41):

$$\frac{\sum_q e_q^2 D_q^h(z)\Delta q}{\sum_{q'} e_{q'}^2 D_{q'}^h(z)\Delta q'}\left[1 + R(x,Q^2)\right] = \frac{A_\parallel^h}{\mathcal{D}} \tag{1.42}$$

The measured longitudinal asymmetries corrected with the depolarization factor $\mathcal{D}$ is written as:

$$A^h(x,z) = \frac{A_\parallel^h}{\mathcal{D}} \tag{1.43}$$

If we have enough informations on the asymmetries, it is possible to decompose the polarized parton distribution functions Δq for each flavor. The simple solution is to identify the hadrons (e.g. π,K and p) in the final state hadrons.

Chapter 2

The HERMES Experiment

The HERMES spectrometer (as shown in Fig.(2.1)) is designed to measure the kinematics of scattered leptons and hadrons produced in DIS with high accuracy. Aiming at experimental studies of the spin structure of the nucleon, both nucleon and probe lepton are required to be polarized. Nucleon and lepton collider can provide enough energy to access the DIS kinematic region. But there is no facility that uses both polarized nucleon and lepton beams. The possible solution to this restriction is to use the polarized lepton beam and the polarized fixed targets. The DESY laboratory in Hamburg, Germany has a suitable polarized lepton beam.

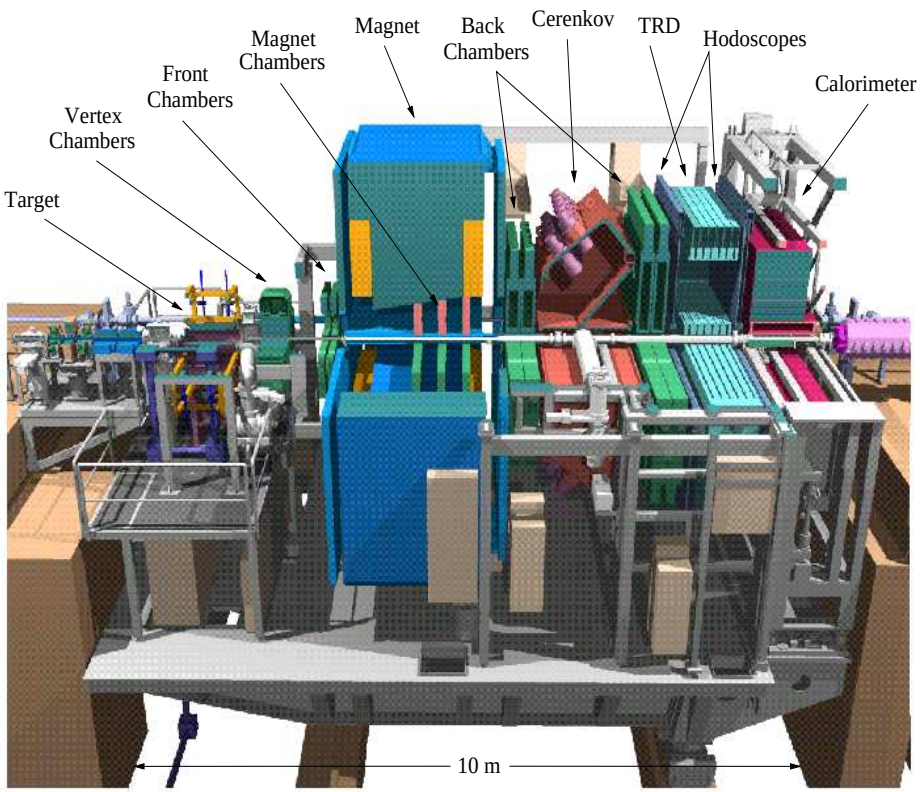

Figure 2.1: 3D-view of the HERMES spectrometer.

2.1 The HERA Storage Ring

The HERMES experiment uses the HERA storage ring at DESY. HERA stores about 35 mA of positron or electron at 27.5 GeV. HERMES is located at the East Hall of the HERA ring. The proton beam for the collider experiments also passes through the HERMES. It is 72 cm apart from the lepton beam, shielded to avoid interactions with the detectors and targets.

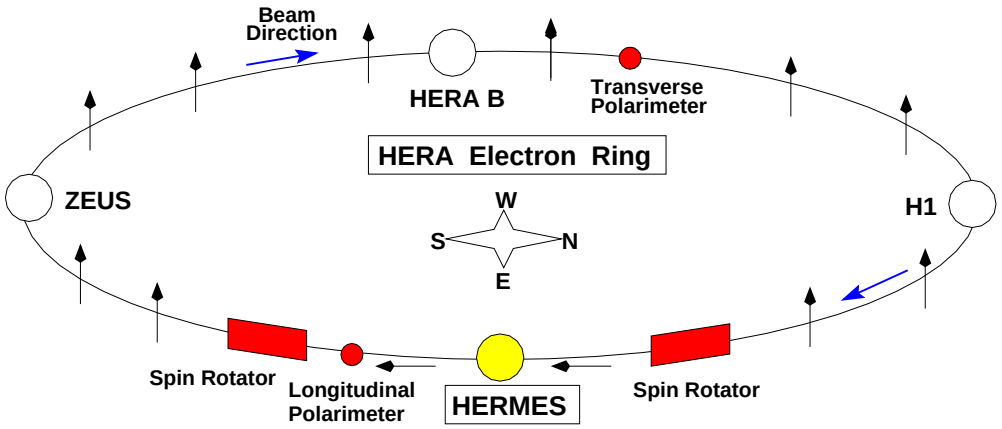

Figure 2.2: Location of HERMES at the HERA storage ring. The other experiments H1, HERA-B and ZEUS, the HERMES spin rotators and polarimeters are superimposed. HERA is about 2 km in diameter.

The polarization of lepton is caused by a small asymmetry in the synchrotron radiation, known as Sokolov-Ternov effect [1]. The maximum polarization predicted by the theory is 92.4% and the polarization is transverse. At HERA the polarization reaches about 55% approximately in 40 minutes in practice.

Two spin rotators have been installed in the HERA ring because the HERMES experiment needs the longitudinal polarized beam to probe quarks in the nucleon. The spin rotators are located upstream and downstream of HERMES. The beam polarization is measured with two laser backscattering Compton polarimeters. The transverse polarimeter is located in the West Hall and the longitudinal polarimeter is inside the spin rotator at the East Hall. The polarization measured with these polarimeters is typically 55%.

2.2 The HERMES Targets

It is technically impossible to polarize the nucleon of a pure solid material to a high degree and use them as a target in a lepton beam. Instead, HERMES uses internal gas targets. HERMES uses the storage cell technique to enhance the target density.

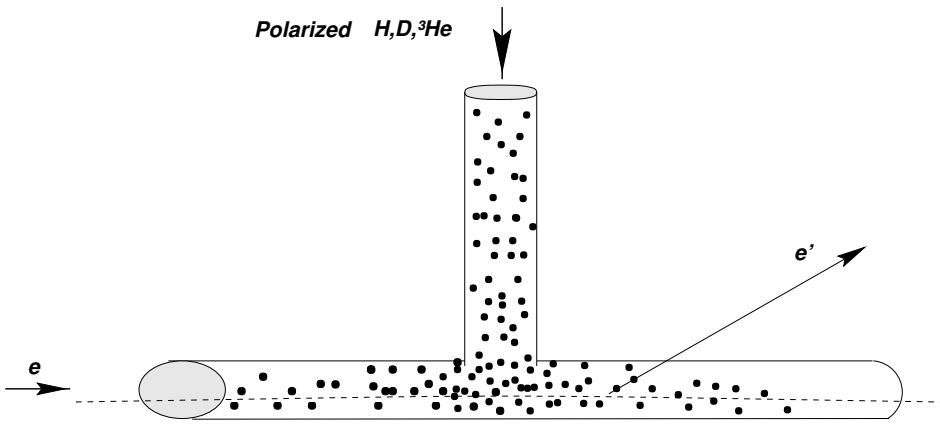

Figure 2.3: Schematic view of the HERMES storage cell.

Fig.(2.3) shows the schematic view of the target. From one side the gas atoms are injected into a thin-walled, T-shaped tube which is called "storage cell". The storage cell is made of aluminum with its length of 400 mm and its wall thickness of 0.125 mm. The target atoms remain inside the cell for typically 3 ms and cross the interaction region many times. When the target atoms are in the target cell, the following interactions are assumed:

- Recombination: the atoms inside the target cell hit the cell walls and form molecules.
- Wall depolarization: the atoms attached to the wall by collision lead to a relaxation of the atom polarization by the interaction with surface magnetic fields.
- Spin exchange collisions: a collision of the atoms may lead to a spin exchange between the hyperfine states of the atoms and cause exchange of electron and proton.

Now the target thickness achieved is 7×10^{13} atoms/cm^2, which is more than two order of magnitude higher compared to the target thickness by a free jet target, usually 2×10^{11} atoms/cm^2.

2.3 The HERMES Spectrometer

The HERMES spectrometer is designed to detect scattered leptons and hadrons produced in DIS. To cover a large kinematic range, the detector needs to have a large angular acceptance. The HERMES spectrometer consists of two identical apparatus, above and below the beam lines. The beam lines are shielded from the magnetic field of the spectrometer by a septum plate. The HERMES spectrometer is a forward detector with a minimal vertical angle of 40 mrad, a maximal vertical angle of 140 mrad and a horizontal acceptance of $\pm$170 mrad.

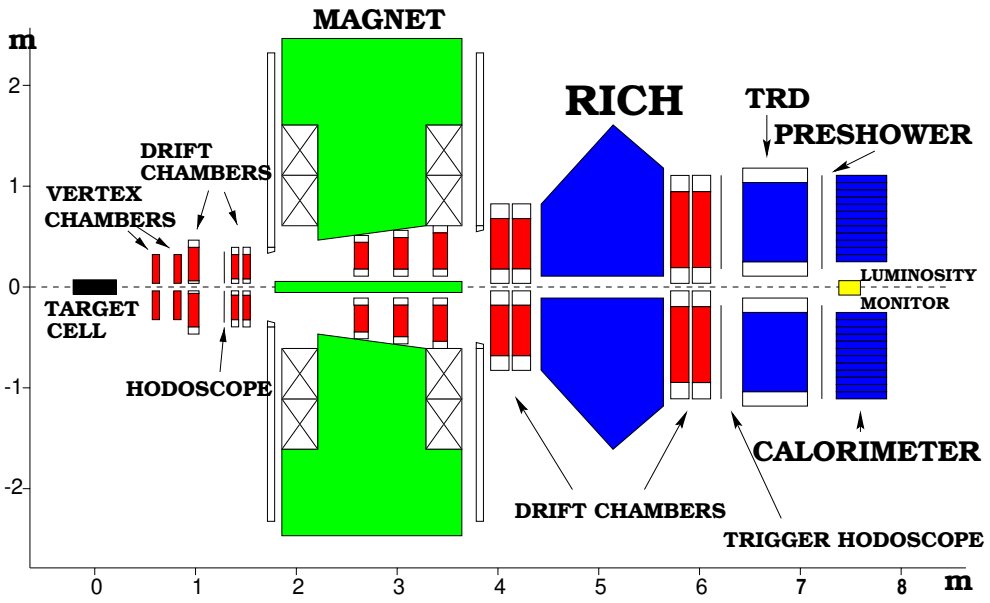

Figure 2.4: Schematic side view of the HERMES spectrometer.

2.3.1 Tracking Systems

The tracking system consists of several chambers in order to satisfy performance requirements as listed below [2].

- Determine the event vertex in the target cell to ensure the reconstruction of the track.
- Measure the scattering angles for the kinematic reconstruction.
- Measure the particle momentum from the track deflection in the spectrometer dipole magnet.

The tracking chambers are divided into three groups. They are roughly located at forward, back and inside of the magnet.

The forward region consists of two detectors; the vertex chambers(VC) and the front drift chambers(FC). The vertex chambers are a micro-strip gas detectors and they provide high-precision measurements of the scattering angle and the vertex position.

The back region consists of the back chambers(BC). They are drift chambers. The back chambers, together with the front chambers, measure the angle of deflection of a particle in the spectrometer magnet and thus its momentum.

The inside region of the magnet consists of the magnet chambers(MC). They are the proportional wire chambers located in the gap of the magnet. The magnet chambers are responsible for matching the tracks from the front chambers and the back chambers, and they can resolve multiple tracks in case of high multiplicity events.

horizontal angular acceptance	$\lvert\theta_x\rvert < 170$ mrad
vertical angular acceptance	$40 < \lvert\theta_y\rvert < 140$ mrad
horizontal fiducial cut at the Calorimeter	$\lvert x\rvert < 175$ cm
vertical fiducial cut at the Calorimeter	$\lvert y\rvert < 30$ cm

Table 2.1: Angular acceptance of the HERMES spectrometer.

The angular acceptance in the front region covered by the opening of the magnet gap is $40 < |\theta_y| < 140$ mrad vertically and $|\theta_x| < 170$ mrad horizontally. The horizontal acceptance in the back region has recently been increased to 270 mrad so that particles with a momentum of > 2 GeV/c can be reconstructed. A particle with momentum of < 0.4 GeV/c might be bent by the dipole magnet and absorbed in the iron yoke of the magnet. The angular acceptance of the spectrometer is summarized in Tab.(2.1).

2.3.2 Particle Identification Method for Lepton-Hadron Separation

The particle identification system should cover the full angular acceptance of the HERMES spectrometer as summarized in Tab.(2.1). The detectors of HERMES are designed to provide a clean measurement of the scattered lepton, as well as a good identification of the final state hadron. All HERMES particle identification (PID) detectors are located downstream the magnet. The PID system consists of the calorimeter, the preshower hodoscopes, the Čerenkov counter and the transition radiation detectors(TRD). The lead glass calorimeter and the preshower hodoscopes allow the measurement of the losing energy of hadrons due to hadronic showers. A ratio of the deposited energy E to the momentum p measured by the track which was bent in the magnetic field allows to separate leptons and hadrons. The TRD allows the separation of highly relativistic particles. The hodoscopes have a role as the first level trigger, but it is also possible to measure the masses of low-energy particles by the time-of-flight method.

The responses of the PID detectors can be converted into a conditional probability L_D^i that the response of the detector D was caused by a particle of the type i. These conditional probability can be derived by comparing the detector response functions for leptons and hadrons generated from either test beam data or from clean particle samples obtained from hard cuts on the other PID detectors.

The conditional probability from several PID detectors can be combined into an overall conditional probability.

$$\mathcal{L}^i = \Pi_D \mathcal{L}_D^i \tag{2.1}$$

The probability $\mathcal{P}^i$ that a particle has a particle type i is related to the conditional probabilities $\mathcal{L}_D^i$ by the incident particle fluxes ϕ^i:

$$\mathcal{P}^i = \frac{\phi^i \mathcal{L}^i}{\sum_j \phi^j \mathcal{L}^j} \tag{2.2}$$

where j runs over all incident particle types.

In this case it is equivalent to create a PID likelihood parameter from the ratio of the lepton and hadron probabilities defined as:

$$PID = \log_{10} \frac{\mathcal{P}^e}{\mathcal{P}^h} \tag{2.3}$$

The quantity is related to the true probabilities $\mathcal{P}^e$ and $\mathcal{P}^h$ by

$$PID = \log_{10} \frac{\mathcal{L}^e}{\mathcal{L}^h} + \log_{10} \frac{\phi^e}{\phi^h} \tag{2.4}$$

The ratio ϕ^e/ϕ^h is approximately independent of the kinematics. The effect of the flux factor introduces a global shift of the $\log_{10} \mathcal{L}^e/\mathcal{L}^h$ distribution against the PID parameter distribution by $\log_{10} \phi^e/\phi^h$. Thus, the PID parameter for each detector D is re-defined as:

$$PID_D = \log_{10} \frac{\mathcal{L}^e}{\mathcal{L}^h} \tag{2.5}$$

The $PID2$ is defined as:

$$PID2 = \log_{10} \frac{\mathcal{L}^e_{Cal} \cdot \mathcal{L}^e_{Pre}}{\mathcal{L}^h_{Cal} \cdot \mathcal{L}^h_{Pre}} \tag{2.6}$$

The $PID5$ is defined as the TRD response parameter.

$$PID5 = \log_{10} \frac{\mathcal{L}^e_{TRD}}{\mathcal{L}^h_{TRD}} \tag{2.7}$$

These variables provide a simple interpretation of the particle identification. Particles with positive PID are likely to be leptons, while with negative PID are likely to be hadrons. In this analysis, $PID2 + PID5$ is used to separate leptons and hadrons with a cut as:

$$PID2 + PID5 > 2.0 \text{ for lepton} \tag{2.8}$$

$$PID2 + PID5 < 0.0 \text{ for hadron} \tag{2.9}$$

Inclusive properties of the charged tracks have been studied extensively in the spin structure of the nucleon. The TRD, the calorimeter and the preshower counter can separate electrons and hadrons produced in DIS. Its performance is 99% electron identification efficiency with less than 1% hadron contamination. Charged $\pi^{\pm}$,$K^{\pm}$ and $p/\bar{p}$ are counted as a function of x_{bj} to obtain the polarized quark distribution function.

The upper limit in momentum required for hadron identification is determined by hadron spectrum as shown in Fig.(2.5). In the distribution of hadrons, 99% has $p < 20$ GeV/c. The distribution of hadrons determines the lower momentum limit. The momentum distribution suggests that a limit of $p > 1$ GeV/c is sufficient.

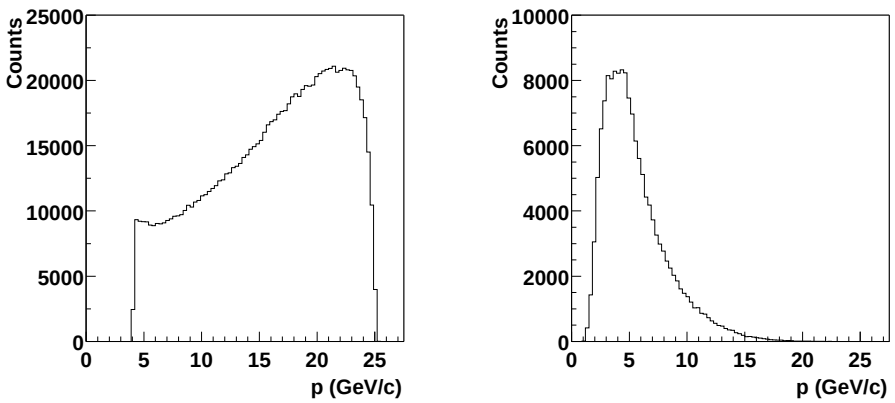

Figure 2.5: The experimental results of the momentum distributions for DIS leptons and hadrons at the acceptance of HERMES. The left plot is the distribution for DIS leptons, the right plot for hadrons measured with DIS leptons.

The distribution of reconstructed DIS leptons is plotted in the $x - Q^2$ plane in Fig.(2.6). The lines are kinematical and acceptance cuts introduced by their labels. θ_{min} and θ_{max} can be calculated with the horizontal acceptance of $40 < |\theta_y| < 140$ mrad and the vertical acceptance of $|\theta_x| < 170$ mrad as:

$$\begin{aligned} \theta_{min} &= \tan^{-1}(\sqrt{\tan^2 0.0 + \tan^2 0.04}) \\ \theta_{max} &= \tan^{-1}(\sqrt{\tan^2 0.14 + \tan^2 0.17}) \end{aligned} \tag{2.10}$$

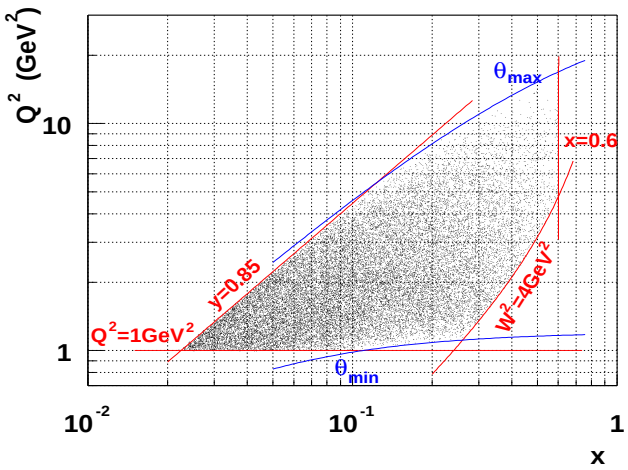

Figure 2.6: The event distributions in the kinematic plane.

HERMES can measure hadrons produced in DIS in the range of $0.02 < x < 0.6$ and $1 < Q^2 < 10\text{GeV}/c^2$. Because kaons consist of sea quarks(e.g. $K^+(u\bar{s})$,$K^-(\bar{u}s)$), it is important to identify π, K and p to study the spin structures of sea quarks in the nucleon. The newly installed HERMES Čerenkov

counter is a dual radiator Ring Imaging Čerenkov Counter which allows the identification of hadrons (π, K and p) in the momentum range of 2-15 GeV/c. The HERMES RICH is the first to use an aerogel as a radiator of the ring imaging Čerenkov counter in an actual experiment.

Chapter 3

The Ring Imaging Čerenkov Counter (RICH)

3.1 Čerenkov Counter

A charged particle moving with velocity β in an optical medium of the refractive index n will emit Čerenkov radiation[3] when the velocity is large enough as explained below. The half-angle θ of the Čerenkov cone has a relation:

$$\cos\theta = \frac{1}{n\beta} \tag{3.1}$$

The azimuthal angle ϕ has a flat distribution from 0 to 2π.

The number of photoelectrons $N_{p.e.}$ is given by

$$\frac{dN_{p.e.}}{dE} = \frac{\alpha}{\hbar c} \cdot Z^2 L \sin^2\theta \tag{3.2}$$

where $dN_{p.e.}$ is the number of photoelectrons with photon energy from E to $E+dE$, L is the path length, α is the electromagnetic fine structure constant and Z is the charge of the particle. At a constant Čerenkov angle θ, the integration of Eq.(3.2) over E, taking into account the detection efficiency ϵ, becomes

$$N = N_0 Z^2 L \sin^2\theta \tag{3.3}$$

where N_0 is a detector response parameter

$$N_0 = (\frac{\alpha}{\hbar c})\epsilon\Delta E \tag{3.4}$$

with

$$\epsilon\Delta E = \int (QTR)dE \tag{3.5}$$

ΔE is the photon energy averaged between minimum E_{min} and maximum E_{max}. Q, T and R are detector efficiencies (Q=efficiency of photon detectors, T=transmission of radiators, R=mirror reflectivity).

From Eq.(3.1), the minimal momentum p_t at which Čerenkov radiation can take place is calculated at $\theta = 0$:

$$p_t = \frac{m}{\sqrt{n^2 - 1}} \tag{3.6}$$

where m is the mass of the charged particle.

With a threshold Čerenkov counter a simple decision on the particle identification is made based on whether the particle is above/below the Čerenkov threshold velocity $\beta_t = 1/n$. The resolution of the pulse height information is evaluated from Eq.(3.3),

$$\frac{\sigma_N}{N} = \frac{1}{\sqrt{N}} = 2\cot\theta\sigma_\theta \tag{3.7}$$

From Eq.(3.1),

$$\sigma_\theta = \cot\theta\frac{\sigma_\beta}{\beta} \tag{3.8}$$

Hence, the resolution of β, σ_β/β, is obtained from the pulse amplitude N:

$$\frac{\sigma_\beta}{\beta} = \frac{\tan^2\theta}{2\sqrt{N}} \tag{3.9}$$

The particle velocity β ranges from n^{-1} to 1, hence $\Delta\beta = 1 - n^{-1}$. It is necessary to use the pulse height in order to measure β with a good precision.

Now I describe the Ring Imaging Čerenkov (RICH) counter. The RICH is mainly constructed from two components. One is a Čerenkov radiator and the other is a photon detector(Fig.(3.1)). Čerenkov photons emitted in the radiator are detected at the surface of the photon detectors. The Čerenkov angle θ and the number of photoelectrons are measured from informations of the ring image on the surface.

The resolution of a RICH counter for a single photoelectron is given by Eq.(3.1). For N photoelectrons the resolution of β becomes

$$\frac{\sigma_\beta}{\beta} = \tan\theta\frac{\sigma_\theta}{\sqrt{N}} \tag{3.10}$$

where σ_θ is the resolution of the Čerenkov angle. RICH counters measure the Čerenkov angle θ directly. An important advantage of RICH counters is that the Čerenkov angle has Gaussian distribution without any backgrounds.

The particle momentum p is written as

$$p = mc\beta\gamma \tag{3.11}$$

where m and β are the particle mass and velocity, c is the speed of light in vacuum and γ is expressed as $1/\sqrt{1-\beta^2}$. From Eq.(3.1) and Eq.(3.11), the number of standard deviation n_σ to discriminate mass m_2 from m_1 is as a function of $u \equiv \cos^2\theta$:

$$n_\sigma = \frac{u_2 - u_1}{\sigma_u/\sqrt{N}} = \frac{m_2^2 - m_1^2}{p^2 n^2}\frac{\sqrt{N}}{\sigma_u} \tag{3.12}$$

where σ_u is the error in u per a single photoelectron and $\sigma_u/\sqrt{N}$ is the error for N photoelectrons. The maximum momentum p_{max} at which the particle identification with n_σ standard deviation is attained is:

$$p_{max} = \sqrt{\frac{m_2^2 - m_1^2}{2\kappa_r n_\sigma}} \tag{3.13}$$

where κ_r is the RICH counter constant defined as:

$$\kappa_r = \frac{n\beta\sigma_\theta}{\sqrt{N_0 L}} = \tan\theta \frac{\sigma_\theta}{\sqrt{N}} \tag{3.14}$$

From Eq.(3.10) and Eq.(3.14), the resolution of β becomes:

$$\frac{\sigma_\beta}{\beta} = \kappa_r \tag{3.15}$$

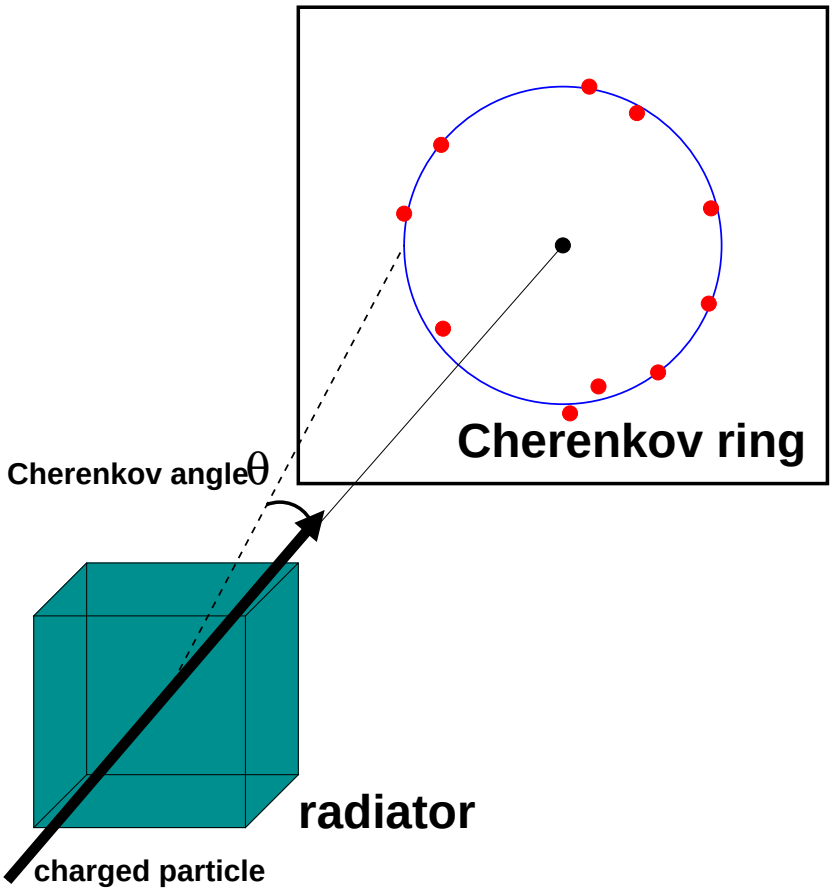

Figure 3.1: Schematic view of the ring imaging Čerenkov counter.

3.2 The RICH Counter of HERMES

The HERMES spectrometer has some detectors to separate electron-hadron such as TRD, calorimeter and preshower counters. It is known that hadrons produced

in HERMES ranges from 1 to 20 GeV/c and most of them lie in the low momentum region as shown in Fig.(2.5). The threshold Čerenkov counter was used from the first year (1995), which was able to identify pions within the limited range of momentum.

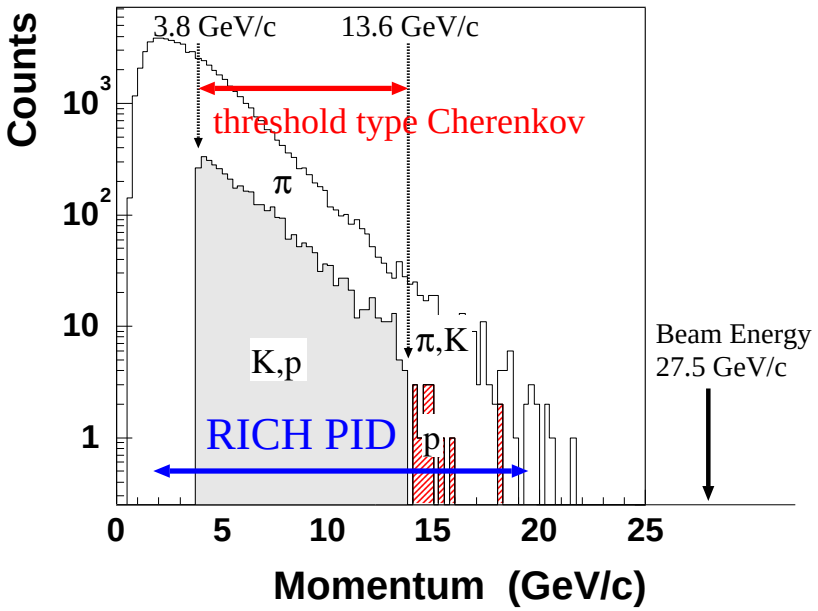

Figure 3.2: The hadron momentum distribution at HERMES.

A clear solid or liquid radiator is useful to identify hadrons in low momentum region (< 2 GeV/c) because of its high refractive index (i.e. low Čerenkov threshold). We can obtain a clear and quadrilateral silica aerogel due to a recent development technique. We have developed a newly Dual-radiator Ring Imaging Čerenkov counter (RICH) in 1997/98 within 13 months after its approval [4].

Fig.(3.2) shows the hadron momentum distribution at HERMES. Pions in the momentum range of $3.8 < p < 13.6$ GeV/c are identified with the threshold Čerenkov counter, while the RICH can identify pions, kaons and protons with the momentum range from 2 to 15 GeV/c due to the two radiators which can identify 80% hadrons produced in DIS.

3.2.1 Components and Geometry

The HERMES RICH is located behind the dipole magnet downstream of the target(Fig.(2.4)). Its hardware design is summarized in Tab.(3.1). It consists of aluminum box and two identical detectors, above and below the beam pipe. Both detectors cover the full angular acceptance of the HERMES spectrometer, from 40 to 140 mrad in the vertical acceptance and from -170 to +170 mrad in the horizontal acceptance.

As a clue to image the outlook of the HERMES RICH, an open section of one of the RICH counters is shown in Fig.(3.3). Fig.(3.4) shows the RICH counter before the aerogel panel is installed.

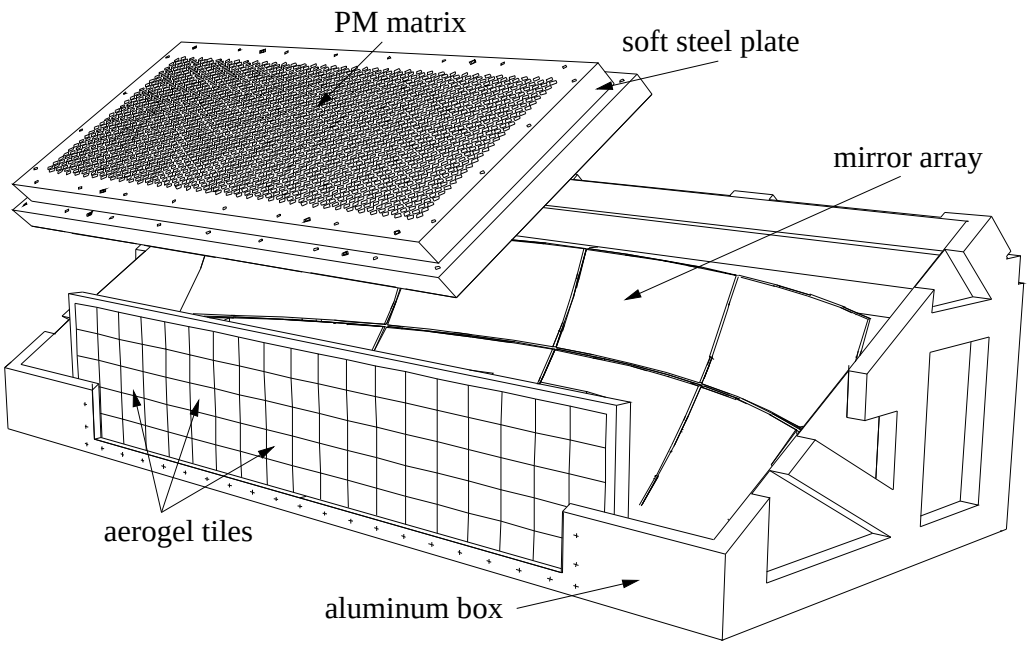

Figure 3.3: The outlook of the HERMES dual-radiator RICH. The silica aerogel panel is installed in front of the detector, which covers an area of $200 \times 60\text{cm}^2$. The RICH housing box is filled with the C_4F_{10} gas.

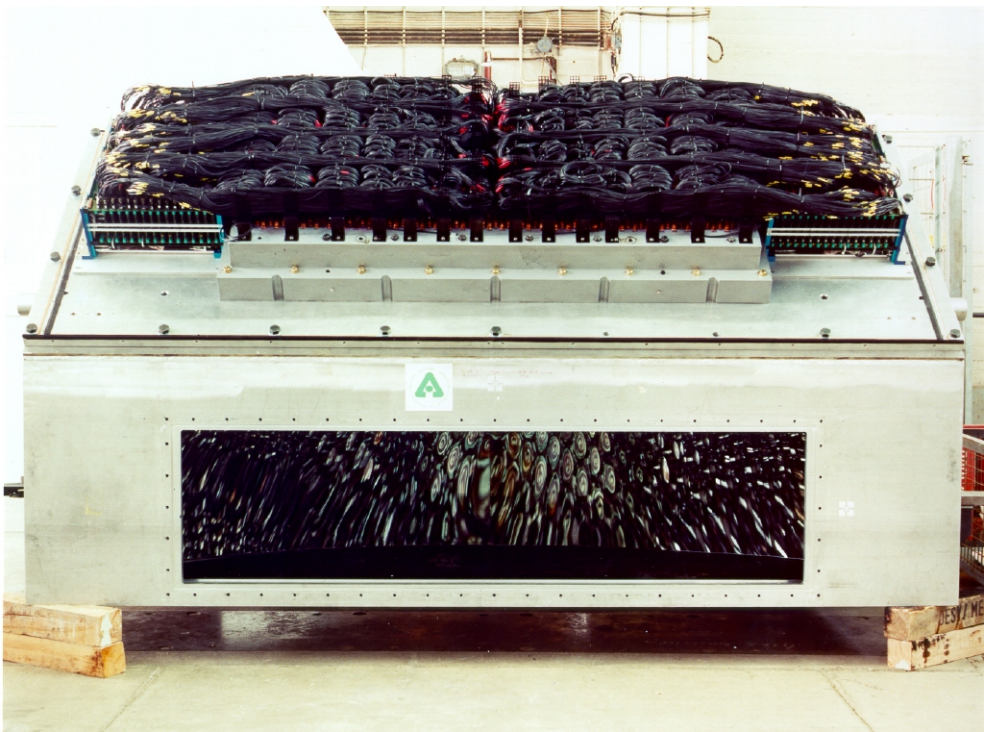

Figure 3.4: A photograph of the RICH before the aerogel panel is installed.

The geometry which is adopted for the Čerenkov radiators and mirror systems is shown in Fig.(3.5). The box of each detector half is comprised of two radiator

systems; the C_4F_{10} gas and the aerogel cover the high and low momentum regions respectively in order to perform the identification of hadrons. Čerenkov photons from these radiators are reflected on the mirror and go into the photon detector plane. Each hit position is measured in two dimensions by the PMT array and used to reconstruct a Čerenkov angle with respect to each extrapolated track [5][6].

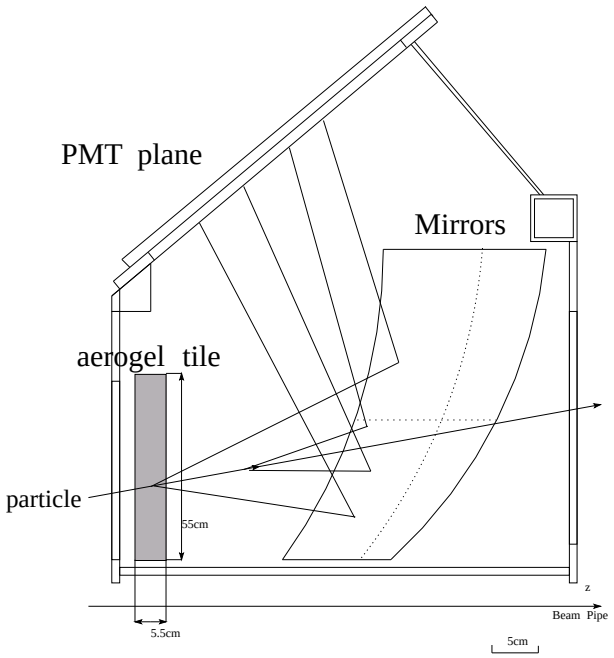

Figure 3.5: Schematic side view of the RICH

The size of an individual aerogel tile is roughly $11 \times 11 \times 1.0$ cm^3 and its refractive index is 1.0303. An aerogel wall is fabricated by the $425(= 17 \times 5 \times 5)$ aerogel tiles per a detector half. A photograph of the aerogel wall is shown in Fig.(3.6). A dry N_2 flows through the aerogel tiles to avoid humidity in the box. Each tile is separated by the black tedlar foil to suppress the refraction at the edge of the aerogel tiles. A front window of the aerogel wall is made by an aluminum plate. On the contrary, the back window is a kind of plastic (lucite) to allow Čerenkov photons to penetrate. The lucite window filters out the short (< 350nm) wavelength Čerenkov light. It is convenient to suppress needless photons out of the active region of the photon detectors by the lucite plate due to Rayleigh scatterings. Further properties of aerogel will be explained in detail in the following section.

The RICH housing box is filled with the C_4F_{10} gas. The gas radiator is contained within the volume of a length of 60cm between the lucite window and the mirror.

Components	Characteristics
Housing Box	$2 \times 2 \times 1.3\text{m}^3$
Radiators	
C_4F_{10} gas	n=1.00137
aerogel	n=1.0303
	size:$11 \times 11\text{cm}^2$ surface $\times 1.0$cm thickness
	number of tiles:$17 \times 5 \times 5 = 425$
Mirrors	radius:220cm
	size:$\sim 60 \times 40\text{cm}^2$
	number of mirrors:8
Photon Detectors	$1934 \times$ 2PMTs
	active area:$145 \times 60\text{cm}^2$
PMT	diameter:3/4"
Readout system	LeCroy PCOS4

Table 3.1: Table of the HERMES RICH components.

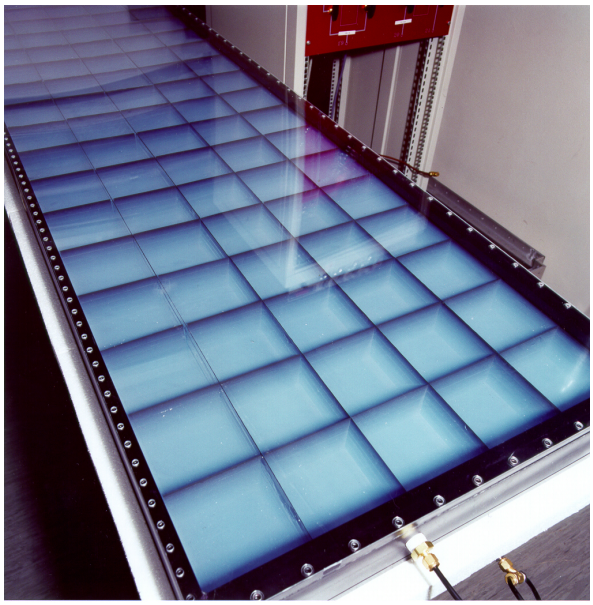

Figure 3.6: A photograph of the aerogel wall to be installed in the RICH.

3.2.2 Characteristics of Silica Aerogel

In general, a gas has a small refractive index ($n \sim 1.001$). It covers the momentum range of > 10 GeV/c for kaon-proton identification. On the contrary, a liquid or a solid material has a large refractive index ($n > 1.1$), which covers low momentum region of < 1 GeV/c.

The momentum distribution of hadrons at HERMES shows that 99% of hadrons are in $2 - 20$ GeV/c (Fig.(2.5)). Therefore, we selected the silica aero-

gel having a refractive index of 1.0303 to be able to identify hadrons in this momentum region.

Figure 3.7: A photograph of the aerogel produced using the new technique.

With the recent technologies, aerogel tiles can be fabricated at Matsushita Electric Works [7]. Fig.(3.7) is a photograph of the aerogel tile. A silica aerogel of 11×11 (surface) $\times 1.1$ (thickness) cm^3 with $n = 1.0303$ has been produced. The following hydrolysis and condensation of silicon alkoxides are proceeded [8][9]:

$$\begin{aligned} m\mathrm{Si(OR)}_4 + 4m\mathrm{H_2O} &\rightarrow m\mathrm{Si(OH)}_4 + 4m\mathrm{ROH} \\ m\mathrm{Si(OH)}_4 &\rightarrow (\mathrm{SiO_2})_m + 2m\mathrm{H_2O} \end{aligned} \tag{3.16}$$

In this successive reactions, the solution becomes colloidal. The production methods are as follows: At first, two solutions are prepared. One is made by adding an oligomer in ethyl alcohol as a solvent, and the other is distilled water with ethyl alcohol. These two solutions are mixed in a polystyrene container at room temperature. After a few minutes, the gelatin is formed and the alcogel is made. The alcogel is put into a sealed vessel in order to suppress evaporation of the ethyl alcohol and is kept at room temperature for one week. Then, the sealed vessel, in which the alcogel has been placed, is filled with ethyl alcohol vapor in order to proceed the formation of a three-dimensional network of $\mathrm{SiO_2}$. After that, alcogel is moved into a stainless-steel bag from a polystyrene container and is left in ethyl alcohol for one week. To make alcogel hydrophobic, a special treatment is taken. The silanol groups on the surface of $\mathrm{SiO_2}$ is likely to be changed and contacting other ions. It is thus replaced into $\mathrm{Si(CH_3)_3}$ groups by adding hydrophobic agent, for example, hexamethyldisilazane, into ethyl alcohol, as shown in Fig.(3.8) [10].

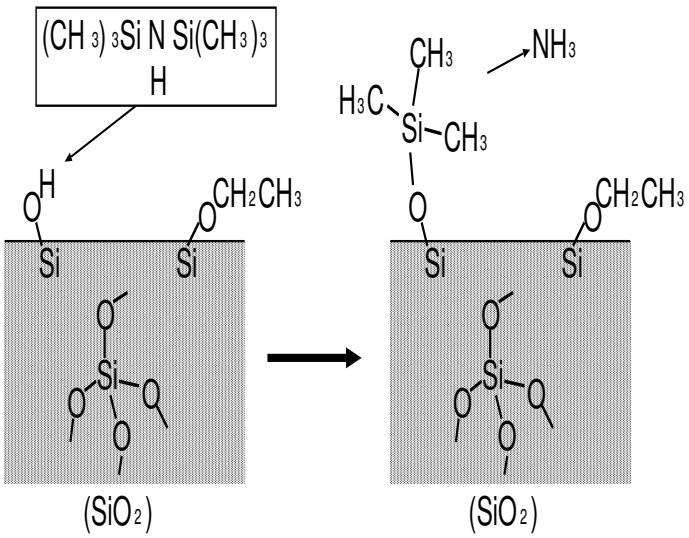

Figure 3.8: The chemical composition of the aerogel.

We checked cracks inside the volume or on its surface, and measured the size and the refractive index of each aerogel tile. One condition is that the average of the refractive index is between 1.028 and 1.032, and the standard deviation of the refractive index is ± 0.002. We selected $17 \times 5 \times 5 = 425$ pieces of good aerogel tiles for each RICH counter half [11].

Geometries

The condition on the size of the aerogel tiles is that the distributions of the longitudinal and transverse sizes are less than ± 0.5 mm [11]. We measured the size of the aerogel tiles. The distributions for all three dimensions are shown in Fig.(3.9). The averaged size is $11 \times 11 \times 1.1\text{cm}^3$, and its deviation is ± 0.4mm.

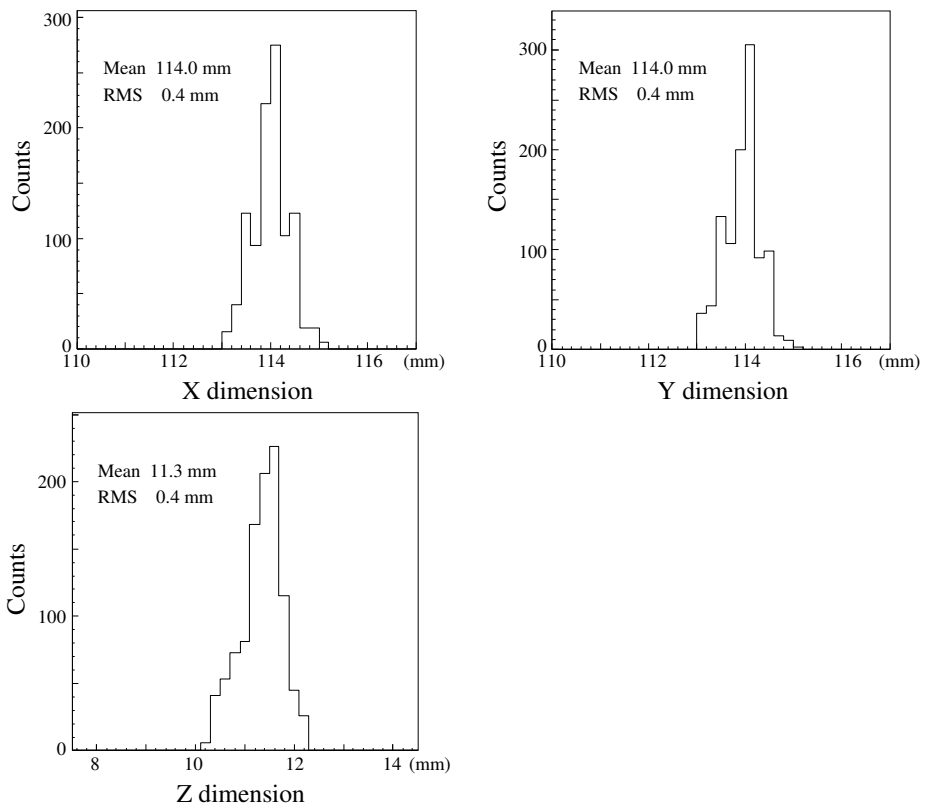

Figure 3.9: Distributions of the size of the aerogel tiles.

The tile is thicker at the edge than in the central region because the side of the tiles is drawn up by the vessel due to its surface tension. A fine measurement of the shape at the edge is performed and the result is shown in Fig.(3.10), which is the fitted with a function along the distance from the center of the aerogel tile.

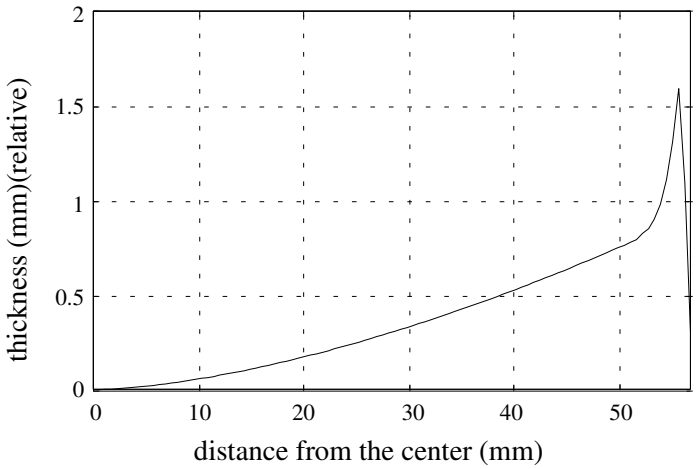

Figure 3.10: The shape of the surface and the edge of the aerogel tile.

The aerogel tiles have sharply curved surfaces near the edge. The Čerenkov photons refracted in this region go in an unpredictable direction. To suppress

these scattered photons, each tile is separated with the black tedlar foil.

The Refractive Index

To use the aerogel as a radiator of the RICH, there are some conditions on the refractive index to be satisfied. In order to satisfy that the PID efficiency is above 95%, the accuracy of the Čerenkov ring should be $\Delta R/R \sim 0.5\%$. (R is the radius of the Čerenkov ring.) Hence, the accuracy of the refractive index n must be $\Delta(n-1)/(n-1) \sim 1.0\%$, which gives the R.M.S$\sim 3\times10^{-4}$. The average of the refractive index is between 1.028 and 1.032, and the standard deviation has to be less than 3.0×10^{-4} [11].

The individual refractive indices of the aerogel tiles are measured using an optical method with a He-Ne laser beam of $\lambda = 632.8$ nm. Fig.(3.11) shows a geometry of the measurement.

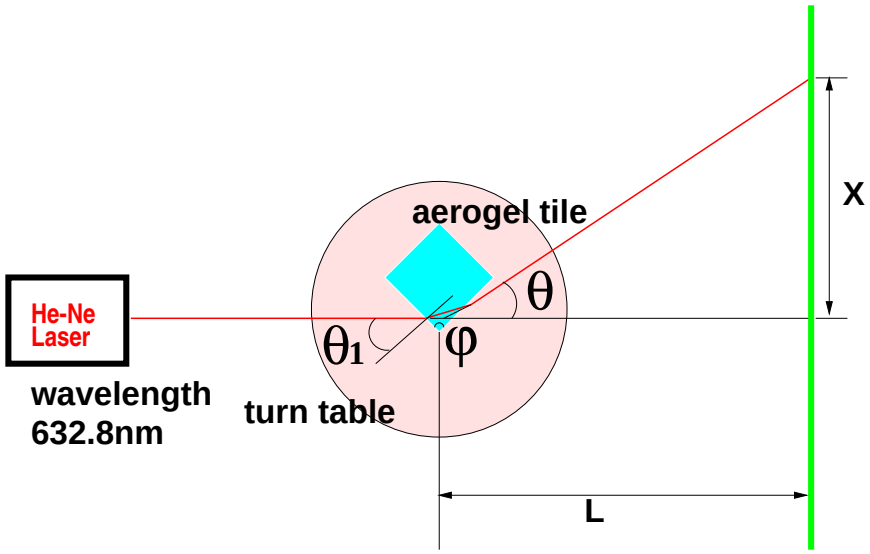

Figure 3.11: Measurements of the aerogel refractive index with He-Ne laser (a schematic top view).

A laser($\lambda = 632.8$nm) from the He-Ne laser device is refracted at the corner(ϕ) twice and makes a spot on the screen. The shift X of the light from an extrapolated incident light has a relation with the angle θ and the distance L between the corner and the screen as:

$$\theta \simeq \tan^{-1}\frac{X}{L} \tag{3.17}$$

We can apply the Snell's law to the incidence angle θ_1 on an edge of the aerogel tile and obtain:

$$\theta = \theta_1 + \sin^{-1}\left(n \cdot \sin\left(\phi - \sin^{-1}\frac{\sin\theta_1}{n}\right)\right) \tag{3.18}$$

By turning the table to the right or the left, we can find the minimal value of X. The angle θ also has a minimal value at the same time:

$$\frac{d\theta}{d\theta_1} = 0 = 1 + (\tfrac{\cos\theta_1}{n}) \cdot \left(-\sqrt{1 - \left(\tfrac{\sin\theta_1}{n}\right)^2} \right)^{-1} \cdot \left(n \cdot \cos\left(\phi - \sin^{-1}\left(\tfrac{\sin\theta_1}{n}\right)\right)\right) \times \left(\sqrt{1 - \left(n \cdot \sin\left(\phi - \sin^{-1}\left(\tfrac{\sin\theta_1}{n}\right)\right)\right)^2} \right)^{-1} \tag{3.19}$$

then we obtain

$$\theta_1 = \sin^{-1}\left(n \cdot \sin\frac{\phi}{2} \right) \tag{3.20}$$

and

$$\theta = 2\sin^{-1}\left(n \sin\frac{\phi}{2} \right) - \phi \tag{3.21}$$

The minimal value of X is measured and it is simply transformed to θ using Eq.(3.17). We can obtain the refractive index n as

$$n = \frac{\sin\frac{\theta_1 \phi}{2}}{\sin\frac{\phi}{2}} \tag{3.22}$$

where ϕ is the angle of the corner of the aerogel tile. It is measured to be 90 degrees.

Fig.(3.12) shows the distributions of the refractive indices for each RICH counter half. The result of the measurement is that the averaged value is 1.0303 and the standard deviation is 2.5×10^{-4}. These values satisfy the requirements on the refractive index.

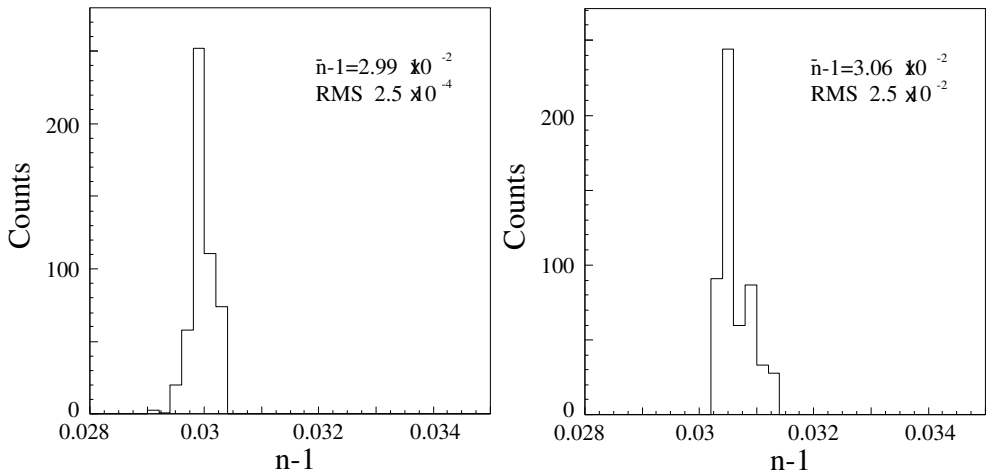

Figure 3.12: Distributions of the refractive indices for each detector half. The left plot shows the distribution of the refractive indices installed in the upper RICH, and the right plot shows those in the lower RICH.

Fig.(3.13) shows the averaged refractive indices over the stacked aerogel tiles in 5 layers. The location where each aerogel should be placed is determined using a computer in order to have the same refractive indices along the y-axis. However, the refractive indices along the x-axis are different. In the upper RICH, the refractive index at $x = 0$ is small and increases along the x-axis. On the contrary, in the lower RICH, the refractive index at $x = 0$ is large and decreases along the x-axis. This configuration allows us to check the effect of the position dependence of the refractive index.

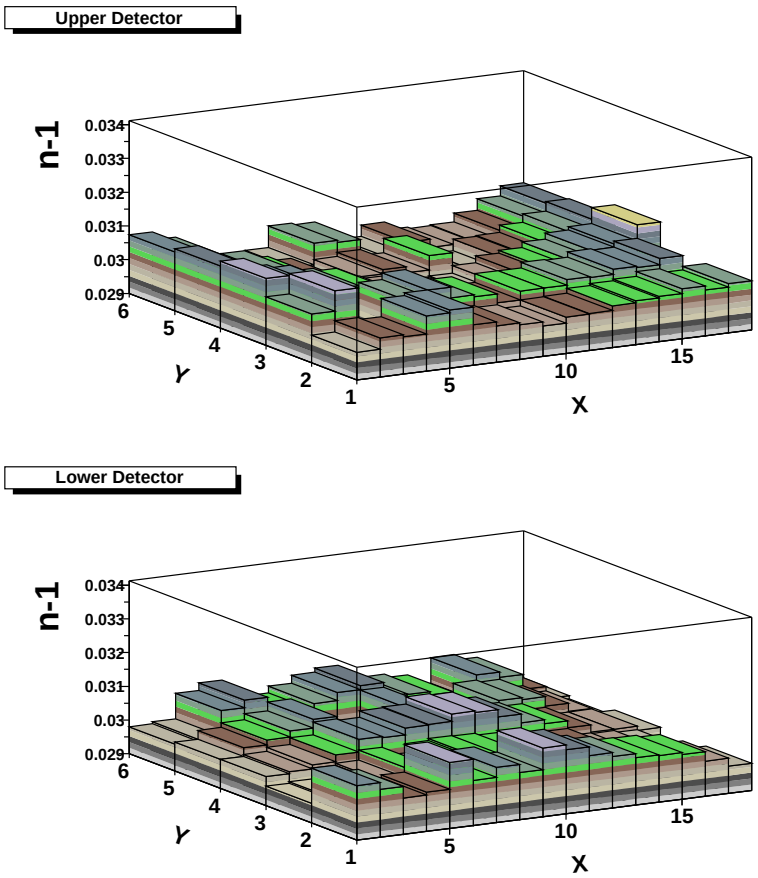

Figure 3.13: Averaged refractive indices of aerogel tiles for each RICH detector half. Aerogel tiles are stacked in 5 layers.

Transmission of the Aerogel Tile

The transmission T of the aerogel is a function of wavelength λ as:

$$T = A \cdot \exp\left(-\frac{C \cdot t}{\lambda^4}\right) \tag{3.23}$$

where t is the thickness of the aerogel tile. A and C are the Hunt parameters. These parameters are related to the size and uniformity of microscopic pores

of the aerogel. C denotes an amount of the Rayleigh scattering. The fitted parameters are $C \cdot t = 0.0094(\mu\text{m})^4$ and $A = 0.964$ [12]. The transmission of the aerogel has achieved above 90%.

3.2.3 Mirrors

The space restriction requires an optical focusing system based on a mirror. The mirror of the RICH counter half consists of eight segments of a mirror. The size of each mirror is approximately $\sim 60 \times 40\text{cm}^2$. The mirrors are made of aluminized carbon fiber in order to minimize the radiation length of the material crossed by particles. The weight is less than 13 kg. The reflectivity of one of the mirrors is already measured before the RICH was installed.

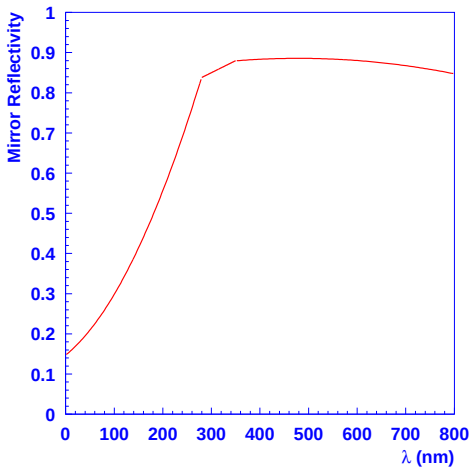

Figure 3.14: The wavelength dependence of the mirror reflectivity for Čerenkov photon.

Fig.(3.14) shows the result of the mirror reflectivity versus the wavelength. The reflectivity is above 85% for the wave-length range of 300-600 nm. This reflectivity is measured for only one mirror segment and we adapt this reflectivity to the other segments.

3.2.4 Photon Detectors and Readout System

The photomultiplier (PMT) plane has a size of $145 \times 60\text{cm}^2$ and contains an array of PMTs which are Philips XP1911 with a diameter of 3/4"(18.6mm). There are 1934 PMTs in each RICH counter half. Each RICH counter half has 73 columns of alternately 26 and 27 PMTs each. The minimum active photocathode diameter is 15 mm. This PMT has a broad quantum efficiency curve that matches the Čerenkov light spectrum of the aerogel. It is also good for the Čerenkov light from the C_4F_{10} gas because the efficiency extends into the UV region. The elementary cell of the PMT array is a hexagon with a PMT at the center. The distance between two adjacent cell centers is 23.3mm.

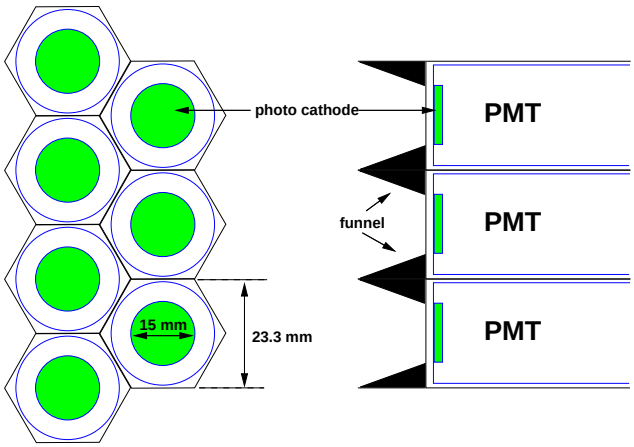

Figure 3.15: Schematic view of the PMT array.

The PMT photo-cathodes cover only 38% of the area of the focal plane. In order to increase the coverage of PMTs, a light-gathering cone, made of an aluminized plastic funnel, was put onto each photo-cathode. This way the PMT photo-cathodes with foil funnels cover 91% of the surface. These funnels minimize the dead space between the PMTs.

These funnels have a high reflectivity above $\lambda = 200$nm. The photon collection efficiency increases to about 80% which was only 40% before inserting the funnels. The effect on the collection efficiency is shown in Fig.(3.16) as a function of the angle between the incoming photon and the normal to the detector plane. The influence of the funnels is found from the difference between the total efficiency and the efficiency for "direct" detection.

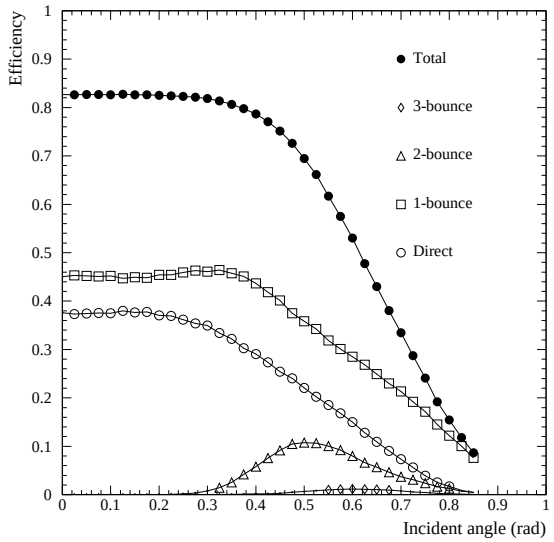

Figure 3.16: The photon collection efficiency versus incident angle. The total efficiency is marked by the solid points. The other points show the components of the efficiency in terms of the number of "bounces", which is the reflection from the foil surface.

The 1934 PMTs for each RICH counter half are read out by the PCOS4 system of LeCroy. The output of the RICH is the hit position of the fired PMTs. It is similar to the multiwire proportional chambers (MWPC). Since the readout system of the 11000 channels of the MWPC is already installed in the HERMES spectrometer, we choose the PCOS4 system. This system allows to develop a compact readout system; 250 front-end cards, 16 electronics controllers based on the FPGA, 5 VME and 1 CAMAC modules. Other features of this system are the low cost per channel ($ 30), the high gain of about $4\mu V/e$ and low noise.

3.3 The Monte Carlo Simulation for the RICH

The simulation for the RICH is performed by the HERMES Monte Carlo(HMC) program. The main parts of HMC are schematically drawn in Fig.(3.17) [13]. HMC consists of three parts of simulations. The first is the LEPTO event generator which simulates the polarized DIS. The second part is JETSET which is used to describe the fragmentations into hadrons. The third is a detector response such as energy losses of hadrons and digitizations of the detector signals which are taken into account using the GEANT detector simulation.

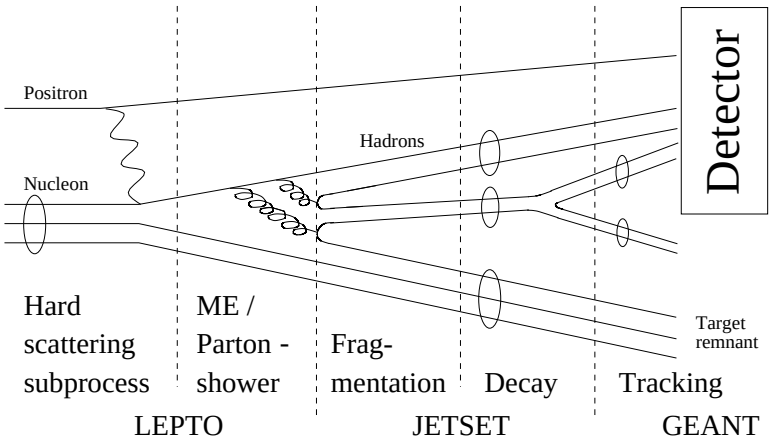

Figure 3.17: Sketch of the different parts which are realized in the MC.

The JETSET which is based on the LUND string model is used to implement hadron fragmentations. The parameters of JETSET were optimized to describe the high-energy data of LEP and HERA. The parameters are re-tuned to fit the hadron spectrum of the HERMES experimental results. Fig.(3.18) shows the hadron momentum spectrum which is corrected for the acceptance of the HERMES spectrometer. The results from the default JETSET parameters and the fitted parameters to the spectrum are superimposed in the figure. Tab.(3.2) shows the numerical values of the JETSET parameters. The parameters of JETSET are: the flavor production ratios, the ratio between quark and diquark production, a parameterization of the string breaking probability (a, b) and the width of the $p_\perp$ distribution [13].

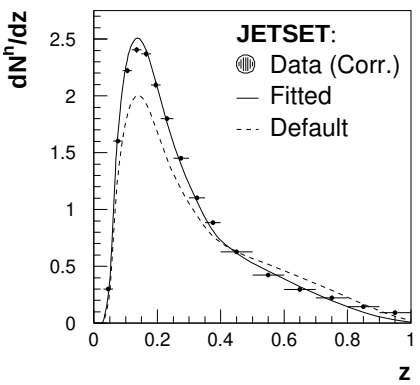

Figure 3.18: Charged hadron spectra in comparison with the simulated spectra from JETSET before and after the tuning.

Parameters	a	b	$\langle p_\perp^2 \rangle$
Default Value	0.30	0.58	0.36
Fitted value	0.82	0.24	0.34

Table 3.2: Parameters of the LUND fragmentation model before and after the fitting.

The GEANT simulates detailed modelings of the detector response. The digitization of the detector signals is still not perfect before the detector simulation. To reproduce the signals the detector efficiencies are taken into account using GEANT.

3.3.1 RICH Improvements in HMC

A simulation of the HERMES RICH is used to estimate systematic effects and to do a detailed comparison of the performance with the experimental data. The simulation defines the physical geometry of the box as a series of "objects". In the RICH the first object is the aluminum window as a front panel, the second is the aerogel radiator, the third is the C_4F_{10} gas radiator, the forth is the mirror and the fifth is the PMT plane. The PMT plane consists of the photon detectors and an aluminum funnel cone. The photon detectors include the photo-cathode quantum efficiencies.

Insight into effects of the RICH apparatus, the simulation is conducted under various conditions. The structure of the simulation is as follows:

1. Effects of the RICH apparatus are included into the simulation: The factors influencing the Čerenkov photons are the refractive index of the aerogel and the C_4F_{10} gas, the Rayleigh scattering, the shape of the aerogel, and the mirror reflectivity. Experimental results for each characteristic are included into the simulation.

2. Perform the simulation: The event generator is LEPTO, and a full GEANT treatment is used. The total number of generated events is 2.5M.

3. Event reconstruction: Tracks are reconstructed using the simulation data. It provides a basic particle information for each track.

4. Particle identification: Each track is identified using the information of the reconstructed data.

Fig.(3.19) shows the HERMES MC and experimental analysis scheme. The properties of the RICH apparatus such as the radiators and the mirror are stored in the data base of the simulation using HDB (HERMES Data Base). HMC (HERMES Monte Carlo) is the main Monte Carlo program which is based on the LEPTO event generator and is able to do a detailed simulation of all HERMES detectors using GEANT. HRC (HERMES ReConstruction) reconstructs tracks from the event data of HMC. It provides a basic particle identification information for each track. PID is the particle identification program based on HANNA. HANNA is the event-driven analysis frame which provides the PID results with HBOOK.

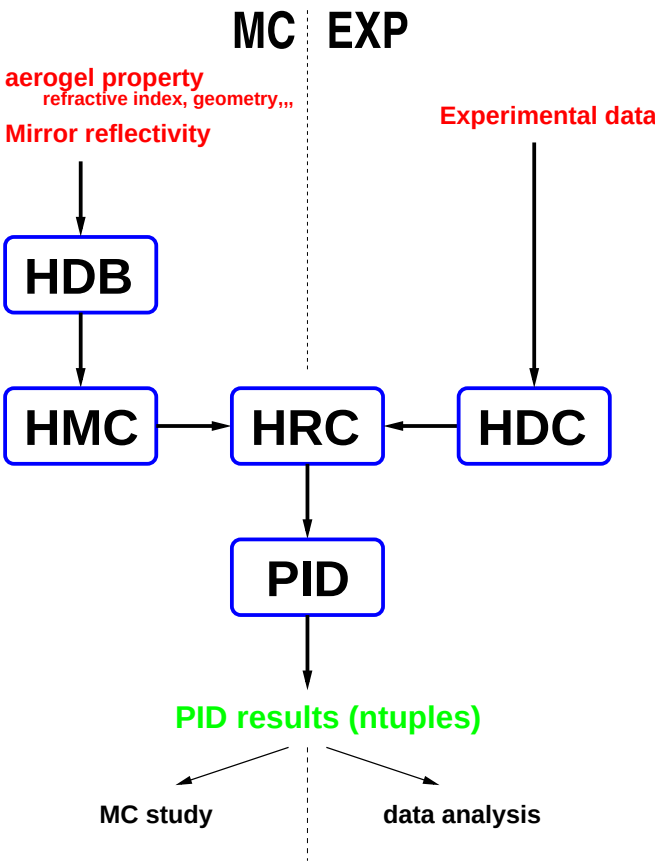

Figure 3.19: The analysis flow for MC and experimental data.

On the other hand, the raw experimental informations are translated to the ADAMO format as it is used in HRC. The experimental events are also reconstructed in the same way as MC data. This analysis frame makes it easy to compare the MC data and the experimental results.

3.3.2 Effects of the RICH Apparatus Included in HMC

We have upgraded the RICH apparatus in HMC. The factors influencing the Čerenkov photons are listed as:

- The Rayleigh scattering
- Aerogel tile/wall geometry
- Edge effects of the aerogel tile
- Čerenkov light refraction at the boundary between aerogel and C_4F_{10}
- Mirror reflectivity

We have checked contributions of each effect to the Čerenkov angle and the number of fired PMTs.

The Rayleigh Scattering

Čerenkov photons produced in aerogel are partially scattered by Rayleigh scattering as was shown by Eq.(3.23). The transmission of light with wavelength λ through a thickness t is proportional to e^{-Ct/λ^4}, where C characterizes the light attenuation by scattering. The fraction of photons which are lost by scattering is

$$F = \frac{A\lambda^4}{Ct}\left(1 - e^{-Ct/\lambda^4}\right) \tag{3.24}$$

where A and C are the Hunt parameters for the radiator. These are taken to $A = 0.964$ and $Ct = 0.0094\mu\text{m}^4$ [12].

The effects of the Rayleigh scattering have a large influence to the number of detected photons. The Rayleigh scattering cross section is proportioned to λ^{-4}. Most photons of low wavelength are scattered in the radiator and they become backgrounds. To suppress this effect, the exit window material is selected to absorb most of them. We choose an ultraviolet-transmitting lucite, which has an absorption cut-off at 280 nm. It is located at the back of the aerogels, in front of the C_4F_{10} gas.

Aerogel Tile/Wall Geometry

To compare the effects of tile and wall geometry, two sets of geometry definitions are prepared. One is "wall geometry", a large aerogel($250 \times 52.0 \times 4.71\text{cm}^3$) with the refractive index $n = 1.0303$. The other is so called "tile geometry". All of the aerogel tiles are placed at the same as experimental setups and the individual refractive indices are also same as experimental ones.

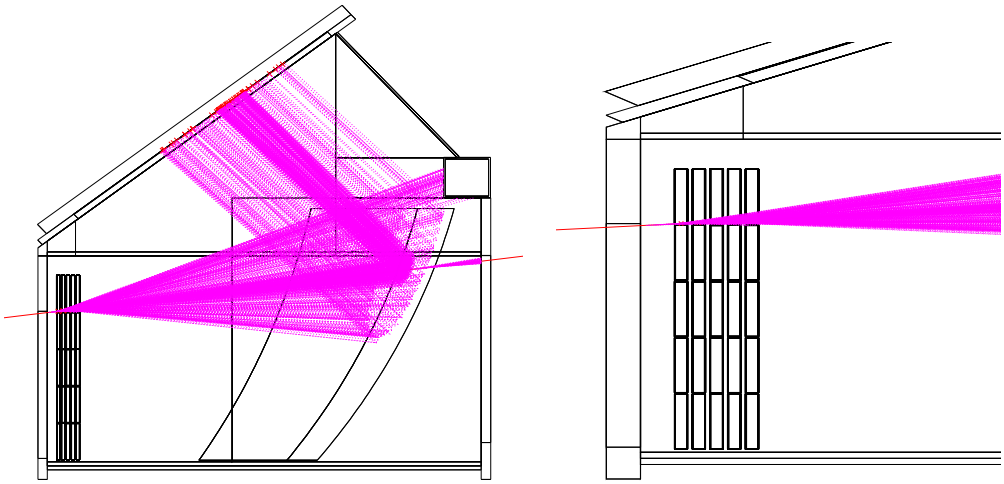

Figure 3.20: A "tile geometry" RICH for the simulation (side view of the RICH). The aerogel has its own individual size, which averaged size is $114\times114\times11.3\text{mm}^3$. The aerogel tiles are stacked in 5 layers. Light lines denote the Čerenkov photons emitted in the aerogels.

Fig.(3.20) shows the schematic view of the RICH in HMC. The left plot is the outlook of the RICH and the right plot shows the aerogel tiles. We can see the aerogel tiles are stacked in 5 layers and the Čerenkov photons are emitted in the radiator.

Edge Effects of the Aerogel Tile

The aerogel tiles have sharply curved surfaces near the edge (Fig.(3.10)). The Čerenkov photons refracted at this region go in an unpredictable direction. To suppress these scattered photons, each tile is separated by the black tedlar foil. This effect is taken into account in the MC to match the experimental configurations.

Čerenkov Light Refraction at the Boundary between Aerogel and C_4F_{10}

The Čerenkov photons are refracted at the boundary between the aerogel and the C_4F_{10} gas. Because of the difference of the refractive index of the radiators, the Čerenkov angle is measured as larger than the predicted value.

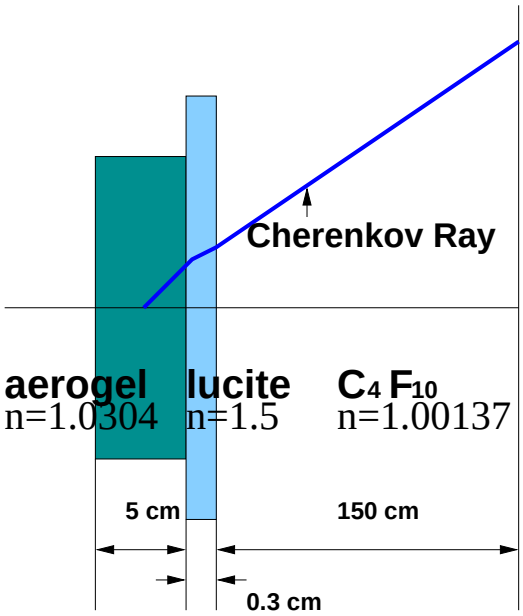

Figure 3.21: Refractions of the Čerenkov ray at the boundary between the aerogel and the C_4F_{10} gas.

As shown with the solid line in Fig.(3.21), the photon ray is refracted twice at the boundaries: aerogel-lucite and lucite-C_4F_{10}. The refractive index of the lucite is about $n_{lucite} = 1.5$ and the thickness is 3mm. The deflection is obtained by assuming an emission angle of 243 mrad and a distance from the lucite to the photon detector of 1.5 m. Under this condition the deflection is evaluated using the Snell's law as:

$$\begin{aligned} & 2.5 \times \tan(0.243) \\ & +0.3 \times \tan(\sin^{-1}(\tfrac{1.0303}{1.5}\sin(0.243))) \\ & +150 \times \tan(\sin^{-1}(\tfrac{1.0303}{1.0014}\sin(0.243))) \\ & = 38.9\text{cm} \end{aligned} \tag{3.25}$$

The emission angle is evaluated from the deflection(38.9cm) and the distance from the emission point to the detector plane (2.5+0.3+150=152.8cm) as:

$$\theta_c = \tan^{-1}\frac{38.9}{152.8} = 0.249 \text{ rad} \tag{3.26}$$

The photon emission angle becomes larger (249mrad) than the predicted value of 243mrad. This result suggests that one has to take into account the contribution of the boundary between the aerogel and the C_4F_{10} gas in order to evaluate the photon emission angle.

We have included the effect of the boundary between the aerogel and the C_4F_{10} gas in the MC.

Mirror Reflectivity

The reflectivity is important because it affects the number of fired PMTs directly. We studied the mirror reflectivity using the pion samples. Comparing the

experimental and MC data, the mirror reflectivity is adjusted to reproduce the experimental data. This analysis allows us to update the value of the reflectivity in the MC [14].

3.4 Čerenkov Angle Resolutions and the Number of Fired PMTs after MC Upgraded

To check the effects as described above, we have compared the MC data and the experimental results. This is performed by selecting pions with low momenta $0 < p < 7$ GeV/c. It is suitable for this investigation because pions with low momenta are bent by the spectrometer magnet and spread in the RICH. Another advantage is that pions below the Kaon threshold of the C_4F_{10} gas are separated easily.

The performed MC productions are:

1. Wall geometry: the aerogel wall has the refractive index of 1.0303, but any other effects are neglected.

2. Tile geometry: the 425 aerogel tiles have individual indices and geometries. The surface of the aerogel tile is also simulated.

3. Tile geometry and the effect of the boundary between aerogel and gas: In addition to the production (2), the effect of the Čerenkov ray refraction at the boundary between the aerogel and the C_4F_{10} gas is simulated.

4. Tile geometry, refraction at the boundary and the mirror reflectivity: In addition to the production (3), the mirror reflectivity is included. This production is expected to agree with the experimental data.

We have checked the number of fired PMTs, $N_{PMT}^{areogel}$ and N_{PMT}^{gas}. (I will explain these values in detail in Chap.4.) Fig.(3.22) shows the results of the four MC productions. The lower plots show the distributions of the number of fired PMTs from the aerogel, the production (1),(2),(3) and (4) from the left. The MC results (denoted by shaded histograms) and the experimental results (normal histograms) are superimposed. The upper plot shows the averaged number of fired PMTs from the aerogel. The square points denote the MC results for each production. The horizontal line at 11.3 is the experimental result. The same plot for N_{PMT}^{gas} is shown in Fig.(B.1) at Chap.B.

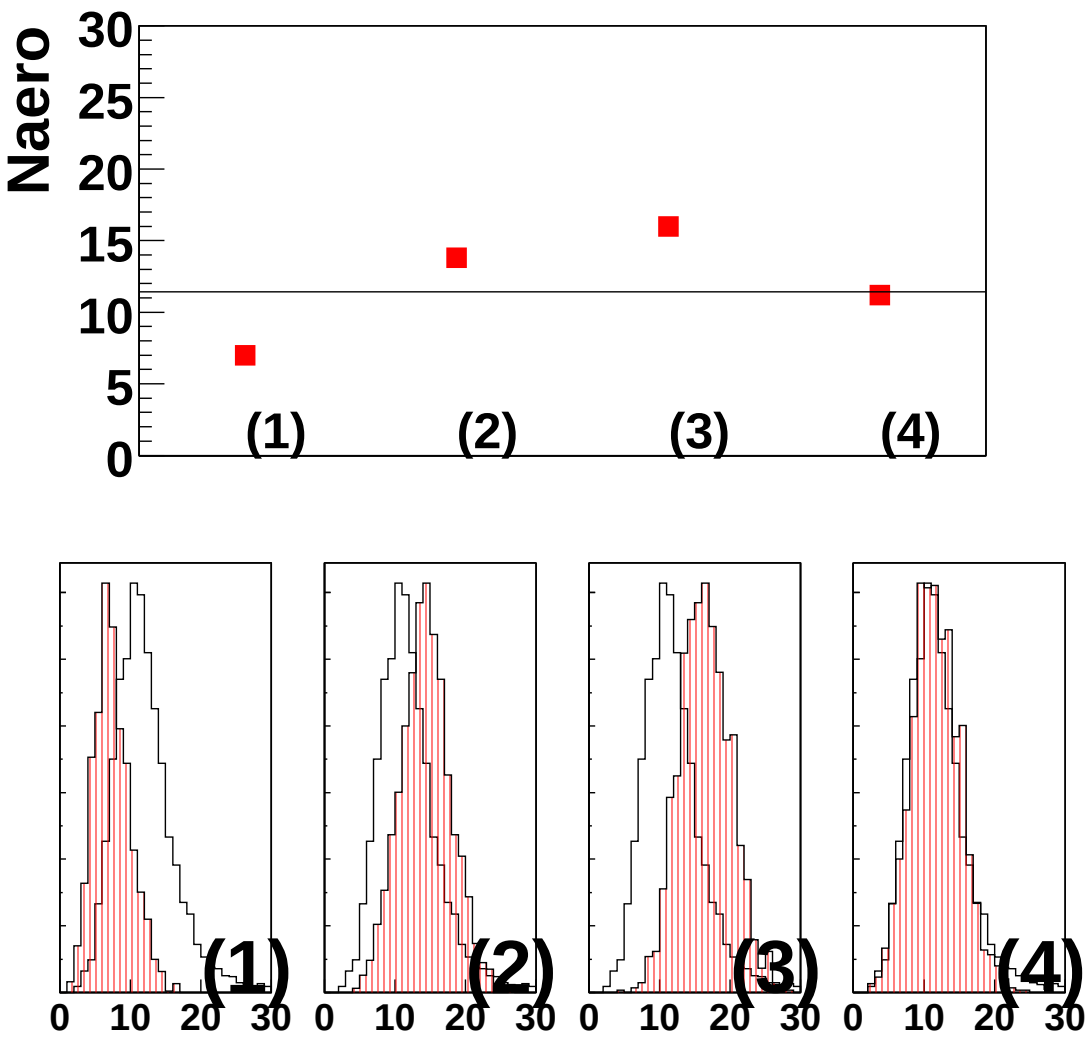

Figure 3.22: The comparison $N_{PMT}^{aerogel}$ with the various MC productions and the experimental result. The lower plots show the distributions of $N_{PMT}^{aerogel}$, the production (1),(2),(3) and (4) from the left. The MC results (denoted by shaded histograms) and the experimental results (normal histograms) are superimposed. The upper plot shows the averaged $N_{PMT}^{aerogel}$. The square points denote the MC results for each production. The horizontal line is the experimental result.

The numerical values of the results are listed in Tab.(3.3). Comparing the experimental data and the MC production (4), the MC data after including all effects is close to the experimental result. Especially the effect of the mirror reflectivity has a large influence to the number of fired PMTs.

MC	T/W	Bnd.	Mir.	$N_{PMT}^{aerogel}$	N_{PMT}^{gas}
1	W	×	×	7.0	13.2
2	T	×	×	13.8	15.1
3	T	◯	×	16.0	15.2
4	T	◯	◯	11.2	13.1
EXP	-	-	-	11.3	11.4

Table 3.3: The numerical values of the number of fired PMTs for each MC Production and the experimental result. "T/W" indicates whether the aerogel is the tile geometry or the wall geometry, "Bnd." indicates that the effect of the boundary between aerogel and C_4F_{10} is included or not, and "Mir." indicates whether the mirror reflectivity is included or not.

In addition to the effects to N_{PMT}, we have checked the reconstructed Čerenkov angle, $\theta^{aerogel}$ and θ^{gas}. Fig.(3.23) shows the results of the four MC productions. The lower plots show the distributions of the Čerenkov angle from the aerogel, the production (1),(2),(3) and (4) from the left. The MC results (shown by shaded histograms) and the experimental results (normal histograms) are superimposed. The upper left plot shows the averaged Čerenkov angle. The square points denote the MC results for each production. The horizontal line at 0.244rad is the experimental result. The upper right plot shows the resolutions of the Čerenkov angle. The triangle points denote the MC results for each production. The horizontal line at 0.0093rad is the experimental result. The same plot for θ^{gas} is shown in Fig.(B.2) at Chap.B.

MC	T/W	Bnd.	Mir.	$\theta^{aerogel}$	±	$\sigma_\theta^{areogel}$	θ^{gas}	±	σ_θ^{gas}
1	W	×	×	233	±	6.0	54.2	±	7.5
2	T	×	×	234	±	6.5	54.0	±	7.6
3	T	◯	×	241	±	7.1	54.2	±	7.7
4	T	◯	◯	241	±	7.1	54.0	±	7.5
EXP	-	-	-	244	±	9.3	49.0	±	9.2

Table 3.4: The numerical values of the reconstructed Čerenkov angles for each MC production and the experimental result. "T/W" indicates whether the aerogel is the tile geometry or the wall geometry, "Bnd." indicates that the effect of the boundary between aerogel and C_4F_{10} is included or not, and "Mir." indicates whether the mirror reflectivity is included or not.

Tab.(3.4) gives a list of the numerical values of the results. After including the effect of the boundary refraction, e.g. the production (3) and (4), the averaged angle is close to the experimental result. It is clear that the effect of the boundary between the aerogel and the C_4F_{10} gas affects the observed Čerenkov angle. On the contrary, the results of θ^{gas} for each MC production do not have any differences. It proves that the aerogel geometry, the boundary conditions

between aerogel and C_4F_{10}, and the reflectivities of the mirrors do not affect the reconstructed Čerenkov angle of the C_4F_{10} gas.

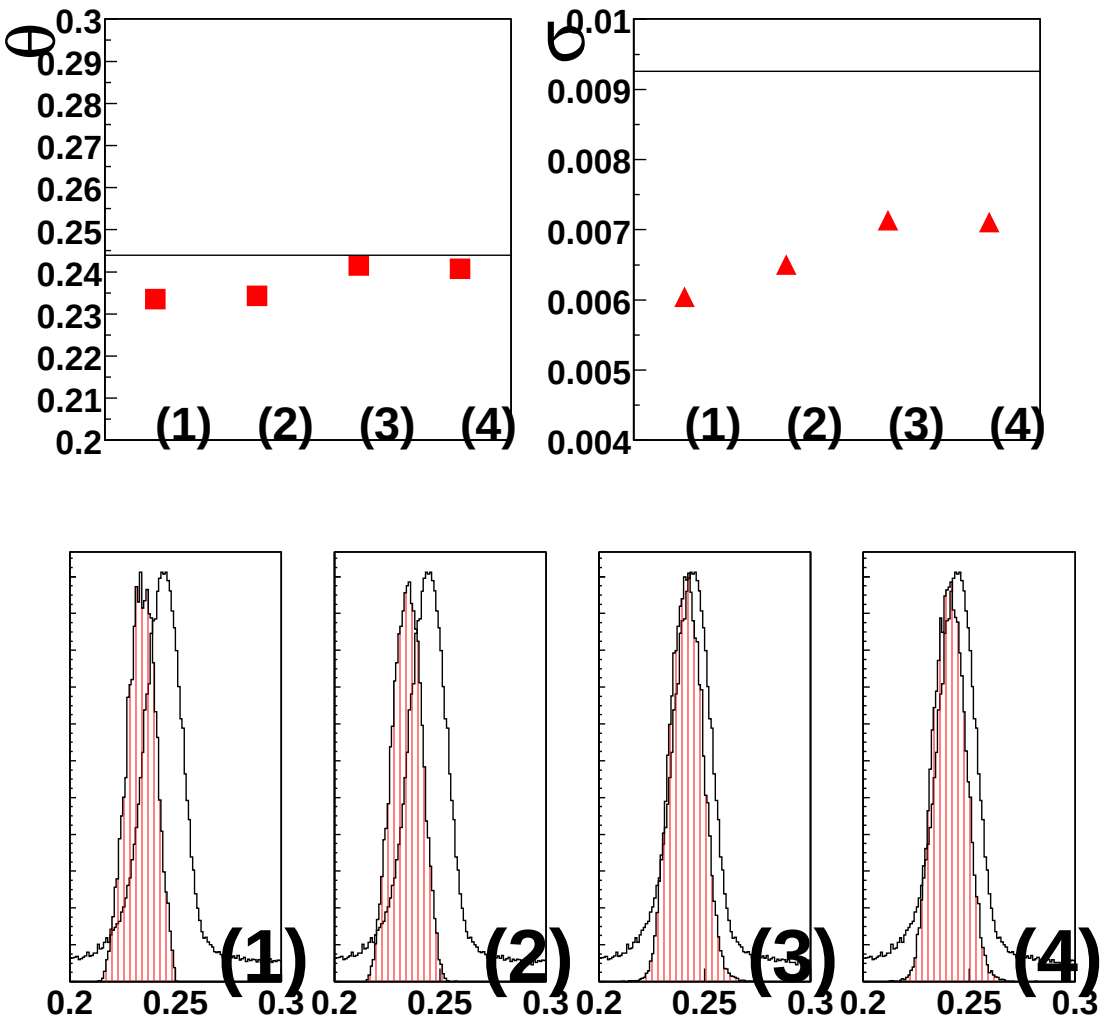

Figure 3.23: The comparison $\theta^{aerogel}$ with the various MC productions and the experimental results. The lower plots show the distributions of $\theta^{aerogel}$ in rad, the production (1),(2),(3) and (4) from the left. The MC results (shown by shaded histograms) and the experimental results (normal histograms) are superimposed. The upper left plot shows the averaged $\theta^{aerogel}$ in rad. The square points denote the MC results for each production. The horizontal line is the experimental result. The upper right plot shows the resolution $\sigma_\theta^{aerogel}$ in mrad. The triangle points denote the MC results for each production. The horizontal line is the experimental result.

In the four MC productions, the results of the Čerenkov angle and the number of fired PMTs with the production (4) are the closest to the experimental results.

Therefore, we have performed the large MC production under the condition of the production (4) to study the RICH performance.

3.5 Results of DIS MC Production

We have performed the MC production with 2.5×10^6 DIS events using HMC. Tracks are reconstructed by HRC. The number of the reconstructed tracks is 1.8×10^6. About 30% of produced events are lost due to short tracks which are bent by the magnet and due to low energy particles absorbed by detectors.

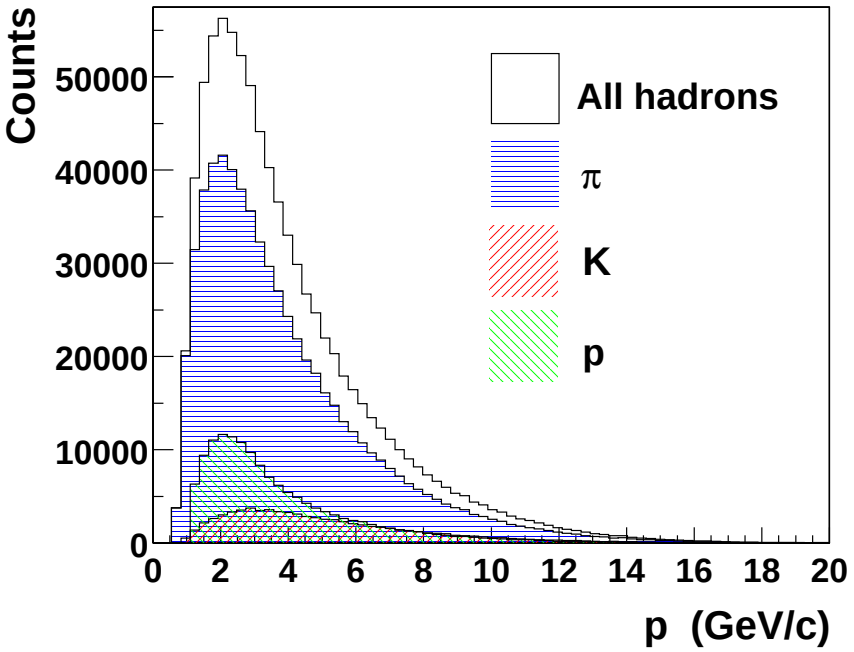

Figure 3.24: Momentum distributions of hadrons(MC).

Fig.(3.24) shows the momentum distributions of the reconstructed hadrons. The distributions of π, K and p are the true hadron spectra because we can obtain the true particle type in MC. On the contrary, the distribution of all hadrons is made using the same lepton-hadron separation method as the experimental technique with $PID2 + PID5$. Comparing hadron spectrum of the MC result in Fig.(3.24) and the experimental result in Fig.(2.5), the distributions show the same exponential fall. The maximum momentum is about 18 GeV/c.

One point I have to mention is that the parameters of the LUND fragmentation model are fitted to only the distribution of all hadrons, not to each hadron type. It means that the distributions of π, K and p do not agree with the real data. I must leave this for a future study.

Chapter 4

Particle Identification with the HERMES RICH

The Čerenkov photons produced in the two radiators are detected by the PMT array. As mentioned earlier, the PMTs are read out using the LeCroy PCOS4 system since the required data is whether the PMT is fired or not, namely digital information (0 or 1).

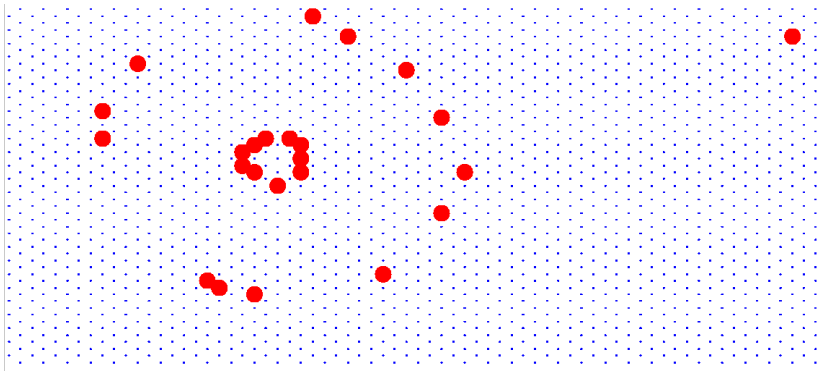

Figure 4.1: A hit pattern for a 4.4 GeV/c π^+. Gas and aerogel rings are clearly visible.

Fig.(4.1) shows the typical hit pattern with (inner) gas and (outer) aerogel rings. A detected Čerenkov ring on the PMT array is not a true circle because the focal points of the mirrors are not on the surface of the PMT array. However, the focal points and the radius of the mirrors, the three dimensional positions of the PMT array are known. Čerenkov angles can be calculated using these informations.

The Čerenkov angle of the C_4F_{10} gas is small while that of the aerogel is large. The averaged number of incident photons per PMT is much smaller than 1 for the aerogel ring, whereas it is about 2 for gas ring, which is estimated by a Monte Carlo simulation.

The HERMES RICH makes use of the available informations from other sectors of HERMES spectrometer in order to identify particles. Basically, the

particle identification of the RICH is performed using the information of the Čerenkov angle and the particle momentum. First of all, the Čerenkov angle θ is calculated using the information on the positions of fired PMTs. Secondly, the momentum $\boldsymbol{p}$ of the particle is determined by the magnetic spectrometer. Finally, the mass of the particle is evaluated by Eq.(3.1) and Eq.(3.11), which is $m = |\boldsymbol{p}|\sqrt{n^2 \cos^2\theta - 1}$.

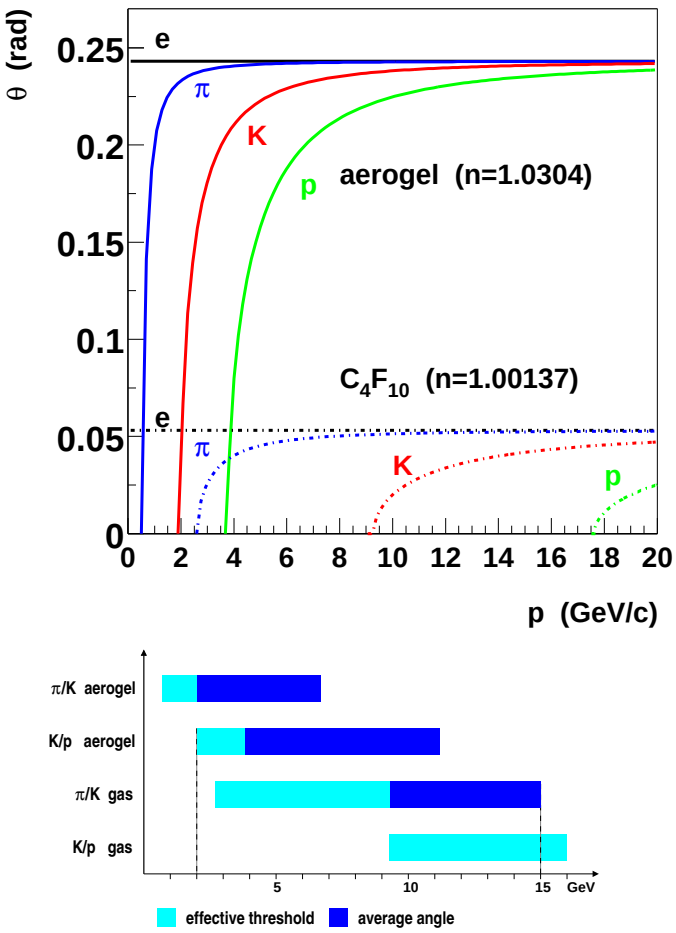

Figure 4.2: Čerenkov angle θ versus particle momentum of e, π, K and p for the aerogel and the C_4F_{10} gas.

Since the HERMES RICH has two radiators, more intelligent particle identification method is adopted. The upper plot of Fig.(4.2) shows the Čerenkov angle θ versus particle momentum of e, π, K and p for the aerogel and the C_4F_{10} gas. The lower plot shows the overlap between the momentum regions for both radiators. The lightly shaded region indicates where the particle can be identified based on whether or not a ring is present at all. In this region the detector acts as a threshold Čerenkov counter. The Čerenkov threshold is summarized in Tab.(4.1).

In the dark shaded region, the identification is based on the Čerenkov angles. In the practical identification algorithm, the informations on the threshold and the Čerenkov angle for both radiators are combined.

	particles		
radiators	π(139.6MeV)	K(493.7MeV)	p(938.3MeV)
$C_4F_{10}(n_{gas} = 1.00137)$	2.7	9.4	17.9
aerogel($n_{gel} = 1.0303$)	0.6	2.0	3.8

Table 4.1: Momentum thresholds(GeV/c) for hadrons for each radiator.

The momentum region for which the identification of π, K and p is possible is determined by the Kaon threshold for the aerogel at 2.0 GeV/c and by the maximum separation momentum for π/K for the C_4F_{10} gas at 15.0 GeV/c [15][16].

4.1 Geometry and Basic Principles

The Čerenkov angle is calculated with an information of track and a hit position of the PMT array. Given the emission point $\boldsymbol{E}$, the hit PMT point $\boldsymbol{D}$, the center of the mirror $\boldsymbol{C}$ and the radius of the mirror R, the reflection point $\boldsymbol{S}$ is reconstructed using an iteration calculation.

We can reconstruct the Čerenkov angle as the angle between the vector $\vec{\boldsymbol{ES}}$ and the track direction $\vec{\boldsymbol{p}}$. This will be explained in the following section(Chap.4.2).

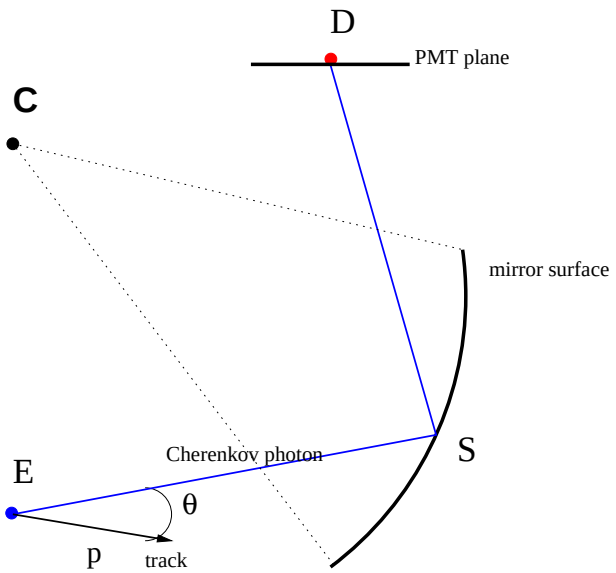

Figure 4.3: The reflection point $\boldsymbol{S}$ is calculated using the emission point $\boldsymbol{E}$, the hit PMT $\boldsymbol{D}$ and the center of the mirror $\boldsymbol{C}$.

The emission point $\boldsymbol{E}$ is not detected with any detectors. Assuming that the Čerenkov photon is produced at the center of the radiator, we can obtain the emission point because it is on the particle track. We have used this hypothetical emission point.

4.2 Identification Methods

Two different identification methods are developed to identify hadrons. One is "Indirect Ray Tracing Method(IRT)" and the other is "Direct Ray Tracing Method(DRT)". Using the DRT method it is possible to estimate where the image of the Čerenkov ring would be. However the amount of CPU time for IRT is smaller than DRT.

Indirect Ray Tracing Method

It should be stressed that the point $\boldsymbol{E}$ is not observed with our techniques. As a solution of this defect, we have assumed that the Čerenkov photons come from the central points of the radiators. The Čerenkov angle θ_c is calculated from the informations of the hit point $\boldsymbol{D}$ on the PMT array and the center of the mirror $\boldsymbol{C}$ using the Indirect Ray Tracing (IRT) method [17].

We choose an Euclid base system with $\boldsymbol{C}$ as the origin as shown in Fig.(4.4). The unit $\vec{\boldsymbol{u}}$ is defined along $\vec{\boldsymbol{CE}}$. The other unit $\vec{\boldsymbol{v}}$ is defined with $\vec{\boldsymbol{CE}}$ and $\vec{\boldsymbol{CD}}$. Its direction is such that $\vec{\boldsymbol{v}} \cdot \vec{\boldsymbol{CD}} > 0$. The third axis $\vec{\boldsymbol{w}}$ is defined so that the base defines a right-handed coordinate system; hence $\vec{\boldsymbol{w}} = \vec{\boldsymbol{u}} \times \vec{\boldsymbol{v}}$. The components of the vectors can be written as:

$$\begin{aligned} \vec{\boldsymbol{CE}} &= (a, 0, 0) \\ \vec{\boldsymbol{CD}} &= (d\cos\alpha, d\sin\alpha, 0) \\ \vec{\boldsymbol{CS}} &= (R\cos\beta, R\sin\beta, 0) \end{aligned} \tag{4.1}$$

where $a = |\vec{\boldsymbol{CE}}|$, $d = |\vec{\boldsymbol{CD}}|$ and $R = |\vec{\boldsymbol{CS}}|$ are fixed values. On the other hand, the angles α and β are defined as $\alpha = \cos^{-1} \hat{\boldsymbol{CE}} \cdot \hat{\boldsymbol{CD}}$, $\beta = \cos^{-1} \hat{\boldsymbol{CE}} \cdot \hat{\boldsymbol{CS}}$. It should be noted that $\hat{\boldsymbol{A}}$ is defined as $\vec{\boldsymbol{A}}/|\vec{\boldsymbol{A}}|$.

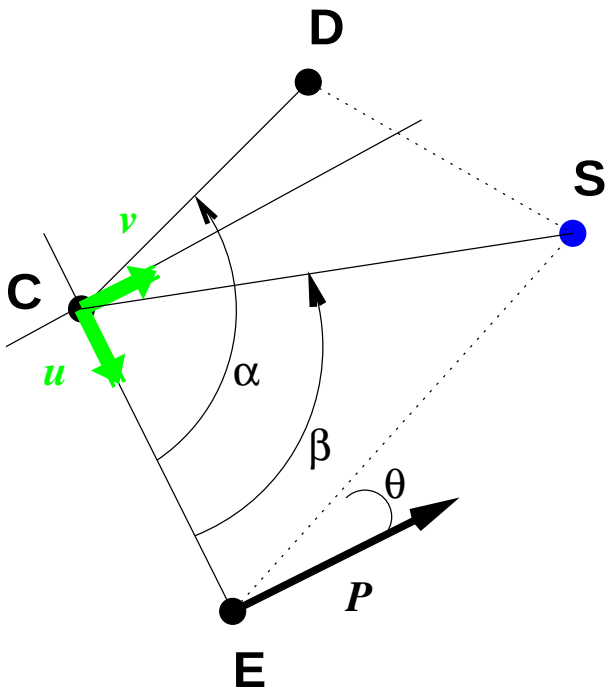

Figure 4.4: The definition of the base and the angle in the IRT method.

Because the angle α is evaluated using informations on the points $\boldsymbol{C}$, $\boldsymbol{E}$ and $\boldsymbol{D}$, all we have to do is to calculate the angle β to find the point $\boldsymbol{S}$. The vectors should satisfy the following conditions:

1. The angle between $\vec{\boldsymbol{SE}}$ and $\vec{\boldsymbol{SC}}$ is the same as $\vec{\boldsymbol{SC}}$ and $\vec{\boldsymbol{SD}}$.
2. $\vec{\boldsymbol{CS}}$ is coplanar with $\vec{\boldsymbol{CE}}$ and $\vec{\boldsymbol{CD}}$.

They are expressed using vectors:

$$\hat{\boldsymbol{SC}} \cdot \hat{\boldsymbol{SE}} = \hat{\boldsymbol{SD}} \cdot \hat{\boldsymbol{SC}} \tag{4.2}$$
$$\hat{\boldsymbol{SC}} \times \hat{\boldsymbol{SE}} = \hat{\boldsymbol{SD}} \times \hat{\boldsymbol{SC}} \tag{4.3}$$

The vectors in these equations can be expressed as:

$$\begin{array}{rcrcl} \vec{\boldsymbol{SC}} & = & -\vec{\boldsymbol{CS}} & = & (-R\cos\beta, -R\sin\beta, 0) \\ \vec{\boldsymbol{SE}} & = & \vec{\boldsymbol{CE}} - \vec{\boldsymbol{CS}} & = & (a - R\cos\beta, -R\sin\beta, 0) \\ \vec{\boldsymbol{SD}} & = & \vec{\boldsymbol{CD}} - \vec{\boldsymbol{CS}} & = & (d\cos\alpha - R\cos\beta, d\sin\alpha - R\sin\beta, 0) \end{array} \tag{4.4}$$

Eq.(4.2) is explicitly written as:

$$\begin{aligned} &\{\cos\beta(a - R\cos\beta) - \sin\beta R\sin\beta\} \,/|\vec{\boldsymbol{SE}}| = \\ &\quad \{\cos\beta(d\cos\alpha - R\cos\beta) + \sin\beta(d\sin\alpha - R\sin\beta)\} \,/|\vec{\boldsymbol{SD}}| \end{aligned} \tag{4.5}$$

and is simply written as:

$$(a\cos\beta - R)|\vec{\boldsymbol{SD}}| = (d(\cos\alpha\cos\beta + \sin\alpha\sin\beta) - R)|\vec{\boldsymbol{SE}}| \tag{4.6}$$

The non-zero component in Eq.(4.3) is the third component along the w-axis as:

$$\begin{aligned}&\{R\cos\beta\sin\beta+\sin\beta(a-R\cos\beta)\}/|\vec{\boldsymbol{SE}}|=\\&\{(d\cos\alpha-R\cos\beta)\cdot(-\sin\beta)+\cos\alpha(d\sin\alpha-R\sin\beta)\}/|\vec{\boldsymbol{SD}}|\end{aligned}\tag{4.7}$$

This equation is reduced to:

$$a\sin\beta|\vec{\boldsymbol{SD}}|=d(-\cos\alpha\sin\beta+\sin\alpha\cos\beta)|\vec{\boldsymbol{SE}}|\tag{4.8}$$

Considering denominators in Eq.(4.6) and Eq.(4.8), the ratio of these equations is:

$$\frac{a\cos\beta-R}{a\sin\beta}=\frac{d(\cos\alpha+\sin\alpha\sin\beta)-R}{d(\sin\alpha\cos\beta-\cos\alpha\sin\beta)}\tag{4.9}$$

which is reduced to:

$$a\cdot d\cdot\sin(\alpha-2\beta)+R\cdot(a\cdot\sin\beta-d\cdot\sin(\alpha-\beta))=0\tag{4.10}$$

where $a=|\vec{\boldsymbol{CE}}|$, $d=|\vec{\boldsymbol{CD}}|$ and $R=|\vec{\boldsymbol{CS}}|$ are fixed with the known experimental setup. The angle α can be written as:

$$\alpha=\cos^{-1}\hat{\boldsymbol{CE}}\cdot\hat{\boldsymbol{CD}}\tag{4.11}$$

An unsolved variable β is left in Eq.(4.10). The solution to the equation can be found from Newton-Raphson iterations with numerical calculations. When β is found, the reflection point $\boldsymbol{S}$ is obtained as:

$$\vec{\boldsymbol{CS}}=R\cos\beta\vec{\boldsymbol{u}}+R\sin\beta\vec{\boldsymbol{v}}\tag{4.12}$$

where

$$\begin{aligned}\vec{\boldsymbol{u}}&=\frac{\vec{\boldsymbol{CE}}}{a}\\\vec{\boldsymbol{v}}&=\frac{\vec{\boldsymbol{CD}}-d\cos\beta\vec{\boldsymbol{u}}}{d\sin\beta}\end{aligned}\tag{4.13}$$

The particle momentum $\vec{\boldsymbol{p}}$ of the track is determined by the tracking detectors. The Čerenkov angle θ_c is obtained as:

$$\theta_c=\cos^{-1}\hat{\boldsymbol{ES}}\cdot\hat{\boldsymbol{p}}=\cos^{-1}\frac{\vec{\boldsymbol{CS}}-\vec{\boldsymbol{CE}}}{|\vec{\boldsymbol{CS}}-\vec{\boldsymbol{CE}}|}\cdot\hat{\boldsymbol{p}}\tag{4.14}$$

Direct Ray Tracing Method

The Direct Ray Tracing method (DRT) can determine the reflection point $\boldsymbol{S}$ on the mirror and the incident point $\boldsymbol{D}$ on the PMT plane [17]. Given the emission point $\boldsymbol{E}$ and the momentum vector $\boldsymbol{p}$ of the Čerenkov photon, $\boldsymbol{D}$ and $\vec{\boldsymbol{SD}}$ can be determined. For the purpose of reconstructing the Čerenkov ring, it is sufficient to determine only $\boldsymbol{D}$. However, it is also necessary to determine $\vec{\boldsymbol{SD}}$ to calculate the incident angle on the PMT plane.

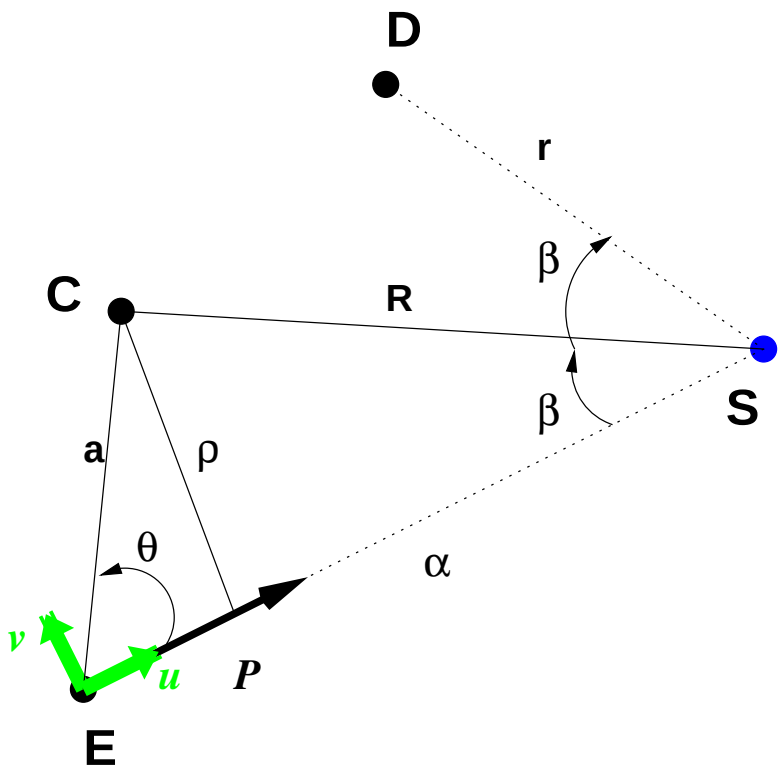

Figure 4.5: The definition of the base and the angle in the DRT method.

ρ is the perpendicular distance of $\boldsymbol{C}$ to the line $\boldsymbol{ES}$. α is the distance from $\boldsymbol{E}$ to $\boldsymbol{S}$.

$$\begin{aligned} \rho &= a\sin\theta \\ &= R\sin\beta \\ \alpha &= |\vec{\boldsymbol{ES}}| \\ &= a\cos\theta + R\cos\beta \end{aligned} \tag{4.15}$$

We choose an Euclid base system with $\boldsymbol{E}$ as the origin as shown in Fig.(4.5). The unit $\vec{\boldsymbol{u}}$ is defined along $\vec{\boldsymbol{ES}}$ and the other unit $\vec{\boldsymbol{u}}$ is perpendicular to $\vec{\boldsymbol{u}}$ in the $\boldsymbol{ECS}$ plane. They are written as:

$$\begin{aligned} \vec{\boldsymbol{u}} &= \frac{\vec{\boldsymbol{p}}}{|\vec{\boldsymbol{p}}|} \\ \vec{\boldsymbol{v}} &= \frac{\vec{\boldsymbol{EC}} - a\cos\theta\vec{\boldsymbol{u}}}{a\sin\theta} \end{aligned} \tag{4.16}$$

$\vec{\boldsymbol{ES}}$ and $\vec{\boldsymbol{ED}}$ are written with the units:

$$\begin{aligned} \vec{\boldsymbol{ES}} &= (\alpha, 0, 0) \\ \vec{\boldsymbol{ED}} &= \vec{\boldsymbol{ES}} + r\,(-\cos 2\beta, \sin 2\beta, 0) \end{aligned} \tag{4.17}$$

The vector $\vec{\boldsymbol{D}}$ is explicitly written as:

$$\vec{\boldsymbol{D}} = \vec{\boldsymbol{S}} + \left(\alpha - r\left[\cos 2\beta - \frac{\sin 2\beta\cos\theta}{\sin\theta}\right]\frac{\vec{\boldsymbol{p}}}{|\vec{\boldsymbol{p}}|}\right) + r\sin 2\beta\frac{\vec{\boldsymbol{EC}}}{a\sin\theta} \tag{4.18}$$

To solve a variable r, it is required that $\vec{\boldsymbol{D}}$ lies on the PMT plane. $\vec{\boldsymbol{D}}$ should satisfy the following equation:

$$\vec{\boldsymbol{N}} \cdot \vec{\boldsymbol{D}} = c \tag{4.19}$$

where $\vec{\boldsymbol{N}}$ is a vector perpendicular to the PMT plane and c is a constant. Defining the tilt angle γ of the PMT plane as the angle between the y-axis on HERMES coordinates and $\vec{\boldsymbol{N}}$. $\vec{\boldsymbol{N}}$ is written as:

$$\vec{\boldsymbol{N}} = (0, \cos\gamma, -\sin\gamma) \tag{4.20}$$

Then Eq.(4.19) becomes:

$$c = \vec{\boldsymbol{E}} \cdot \vec{\boldsymbol{N}} + \left(\alpha - r\left[\cos 2\beta - \frac{\sin 2\beta \cos\theta}{\sin\theta}\right]\right)\frac{\vec{\boldsymbol{p}} \cdot \vec{\boldsymbol{N}}}{|\vec{\boldsymbol{p}}|} + r \sin 2\beta \frac{\vec{\boldsymbol{EC}} \cdot \vec{\boldsymbol{N}}}{a \sin\theta} \tag{4.21}$$

The solution for r is

$$r = \frac{c - \vec{\boldsymbol{E}} \cdot \vec{\boldsymbol{N}} - \left(\alpha - \frac{\sin 2\beta \cos\theta}{\sin\theta}\right)\frac{\vec{\boldsymbol{p}} \cdot \vec{\boldsymbol{N}}}{|\vec{\boldsymbol{p}}|}}{\frac{\sin 2\beta \vec{\boldsymbol{EC}} \cdot \vec{\boldsymbol{N}}}{a \sin\theta} - \cos 2\beta \frac{\vec{\boldsymbol{p}} \cdot \vec{\boldsymbol{N}}}{|\vec{\boldsymbol{p}}|}} \tag{4.22}$$

The procedure is to calculate a and θ, then deduce β and α. Then calculate $\frac{\vec{\boldsymbol{p}} \cdot \vec{\boldsymbol{N}}}{|\vec{\boldsymbol{p}}|}$, $\vec{\boldsymbol{E}} \cdot \vec{\boldsymbol{N}}$ and $\vec{\boldsymbol{EC}} \cdot \vec{\boldsymbol{N}}$, which allows the calculation of r.

4.3 Likelihood Technique

The Čerenkov ring on the PMT plane is not a perfect circle due to configurations of the imaging system of the RICH. Instead of determining a Čerenkov ring directly, a likelihood (which is a measure using probability) is defined. The task of the likelihood technique is to assign a particle type (π,K,p) to each track, so as to best describe the observed hit.

Our particle identification algorithm is developed to satisfy some requirements:

1. to make full use of available informations: Čerenkov angle, number of fired PMTs
2. to take into account the threshold informations
3. to give equal treatments to C_4F_{10} and aerogel radiators

We have two algorithms to determine the likelihood corresponding to the two reconstructed methods (IRT and DRT). The details will be discussed in the following sections.

4.3.1 IRT Likelihood Algorithm

The information on a track is represented by the three-dimensional momentum $\vec{p}$ and its location $\vec{X}$. These informations can be measured by the magnetic spectrometer. Suppose the track is the particle type $h(= e, \pi, \mathrm{K}, \mathrm{p})$, the theoretical Čerenkov angle θ_{th} is calculated:

$$\begin{aligned} \theta_{th}^{gas} &= \cos^{-1}\frac{1}{n_{gas}}\sqrt{1+\left(\frac{m_h}{|\vec{p}|}\right)^2} \\ \theta_{th}^{aerogel} &= \cos^{-1}\frac{1}{n_{aerogel}}\sqrt{1+\left(\frac{m_h}{|\vec{p}|}\right)^2} \end{aligned} \tag{4.23}$$

where m_h is the mass of particle h, n_{gas} and $n_{aerogel}$ are the refractive indices of the C_4F_{10} gas and the aerogel.

A hit position (Dx, Dy) on the PMT array is transformed to "Čerenkov space" (θ, ϕ). The transformation between these systems is calculated with IRT method.

The allowable range σ_w(which is called "window size") of angles of θ_{th}^{gas} and $\theta_{th}^{aerogel}$ determines the zone: $\theta \in [\theta_{th} - \sigma_w, \theta_{th} + \sigma_w]$. Then we obtain the number of fired PMTs in this window which are activated by the photons from the C_4F_{10} gas and the aerogel; N_{PMT}^{gas} and $N_{PMT}^{aerogel}$. The average of the Čerenkov angle is also calculated using the Čerenkov angles in the window. $\langle\theta^{gas}\rangle$ and $\langle\theta^{aerogel}\rangle$ denote the averaged Čerenkov angles.

For each of the hypothesis $h(= \pi, \mathrm{K}, \mathrm{p})$, a likelihood is calculated based on the number of fired PMTs $N_{PMT}^{gas/aerogel}$, the averaged Čerenkov angle $\langle\theta^{gas/aerogel}\rangle$, the averaged resolution $\sigma_{\langle\theta^{gas/aerogel}\rangle}$ and the theoretical Čerenkov angle $\theta_{th}^{gas/aerogel}$. With a Gaussian shape of the averaged angle distribution the likelihood is calculated as:

$$L^{gas/aerogel} = \exp\left\{-\frac{(\langle\theta^{gas/aerogel}\rangle - \theta_{th}^{gas/aerogel})^2}{2\sigma^2_{\langle\theta^{gas/aerogel}\rangle}}\right\} \tag{4.24}$$

where $\sigma_{\langle\theta^{gas/aerogel}\rangle}$ is the averaged angle resolution which is calculated from the single photon resolution $\sigma_\theta^{gas/aerogel}$:

$$\sigma_{\langle\theta^{gas/aerogel}\rangle} = \frac{\sigma_\theta^{gas/aerogel}}{\sqrt{N_{PMT}^{gas/aerogel} - 1}} \tag{4.25}$$

In addition to informations on the Čerenkov image, an effect of Čerenkov thresholds is taken into account. It is summarized simply as:

- If a particle is below the Čerenkov threshold momentum, any PMTs should not be fired. Let a likelihood be a fixed value $L_{s.thre.}$, so called the sub-threshold likelihood.
- A particle above the Čerenkov threshold momentum has the number of fired PMTs below the background level. The minimum likelihood L_{min} is

calculated as:

$$L_{min}^{gas/aerogel} = \exp\left\{-\frac{\sigma_w}{2\sigma^2_{\langle\theta\, gas/aerogel\rangle}}\right\} \tag{4.26}$$

where σ_w is the window size.

The algorithm flow is shown in Fig.(4.6). The momentum of the Čerenkov threshold $p_{thre.}$ for each radiator is calculated for the particle type h. B^h_{PMT} is the background of the fired PMTs for each particle hypothesis. It is a free parameter and can be adjusted to optimize the performance of the particle identification.

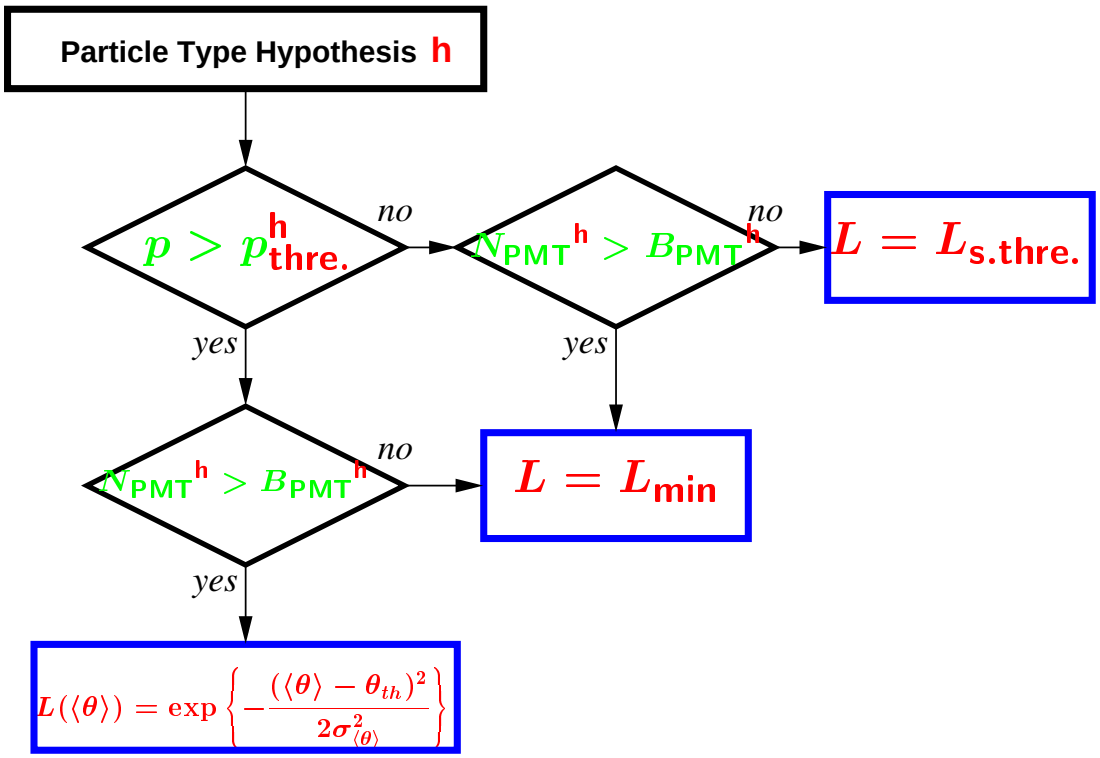

Figure 4.6: The algorithm flow of the IRT likelihood calculation: p is the momentum of the particle, and $p_{thre.}$ is the momentum threshold for each radiator. N_{PMT} is the number of fired PMTs, and B_{PMT} is the number of background PMTs. L is the likelihood for the particle hypothesis h, $L_{s.thre.}$ is the sub-threshold likelihood, and L_{min} is the minimum likelihood.

We can obtain two likelihoods L^{gas} and $L^{aerogel}$ for the two radiators. They are combined to the overall likelihood $L = L^{gas}L^{aerogel}$ by multiplication.

4.3.2 DRT Likelihood Algorithm

We can see from Eq.(3.1) and Eq.(3.2) that the number of the fired PMTs depends on the particle and its track and velocity. The probability for the i-th PMT to

be fired $P_h(i)$ is evaluated according to the Poisson distribution:

$$P(i;h) = 1 - \exp\left(-N_{pe}(i;h)\right) \tag{4.27}$$

where $N_{pe}(i;h)$ is the total number of photoelectrons expected in the i-th PMT for each hypothesis $h(=\pi, \mathrm{K}, \mathrm{p})$:

$$N_{pe} = \sum_{t,h} N_0^r l^r \sin^2\theta^{(t,r,h)} \frac{N_{PH}^{(t,r,h)}(i)}{\sum_i N_{PH}^{(t,r,h)}(i)} + BG \tag{4.28}$$

where t and r denote the track and radiators. N_0^r is the quality factor of the radiator r with thickness l^r. $N_{PH}^{(t,r,h)}(i)$ is the number of photons in the i-th PMT. BG is the number of photoelectrons expected from backgrounds.

N_0^r and $N_{PH}^{(t,r,h)}$ should be evaluated by a Monte Carlo simulation. These factors contain effects of the detector response, multiple-track events and overlapping rings.

The likelihood is calculated from $P(i;h)$:

$$L_h = \Pi_i \left\{P(i;h)C(i) + (1 - P(i;h))(1 - C(i))\right\} \tag{4.29}$$

where $C(i)$ is 0 if the i-th PMT does not fire, or 1 if it fires. i runs over all of the PMTs ($i \in [1, 2, ..., 1934]$ for each RICH counter half).

4.3.3 Quality Parameter

A likelihood L_h is calculated for each of the hypothesis $h(=\pi, \mathrm{K}, \mathrm{p})$. Comparing these likelihoods L_h, we select the particle type that has the highest likelihood. Difference of logarithms between the highest and the second highest likelihood indicates how reliable the identification is. The "quality parameter" is

$$Qp = \log_{10}\frac{L_1}{L_2} \tag{4.30}$$

where L_1 and L_2 are the highest and the second highest likelihood.

Because L_1 is larger than L_2, the quality parameter should be $Qp > 0$. However, in the case where the highest and the second highest likelihood are the same value, the particle becomes "not-identified particle(X)" and $Qp = 0$.

Chapter 5

The Performance of the Čerenkov Ring Reconstruction

It is necessary to calculate the Čerenkov angle from the information of the hit PMT pattern. The way to evaluate Čerenkov angle is already discussed in Chap.4.2. The Čerenkov angle for each hit position is determined by the IRT reconstruction method. The single photon resolution should affect the performance of the particle identifications. To obtain sufficient resolution, we have tuned the parameters which are concerned with the IRT method. The factors that we have optimized to obtain the best resolution are listed below:

- The alignment of the mirrors
- The refraction of the Čerenkov ray at the boundary between the aerogel and the C_4F_{10} gas

The mirror system consists of 8 small mirrors, and each mirror has a curvature radius of 220 cm and a size of $\sim 60 \times 40 \mathrm{cm}^2$. They are made of aluminum (see Tab.(3.1)). The positions that the mirrors are mounted are calibrated before installing the RICH. However, the mirrors are observed to be slack by their own weight. We have corrected the focus point by software. A mirror is imaginary divided into 3×3 peaces, and evaluated the focus position for each peace.

The second improvement is that the Čerenkov ray is refracted at the boundary between the aerogel and the C_4F_{10} gas. A Čerenkov photon emitted in the aerogel will cross two boundaries, one is the boundary between aerogel and lucite, and the other is between lucite and C_4F_{10} gas. Due to differences of their indices, the Čerenkov ray is bent at the boundary as discussed in Chap.3.3.2. We have corrected for the effect by calculating back the ray trajectory.

5.1 The Performance of the Experimental Data

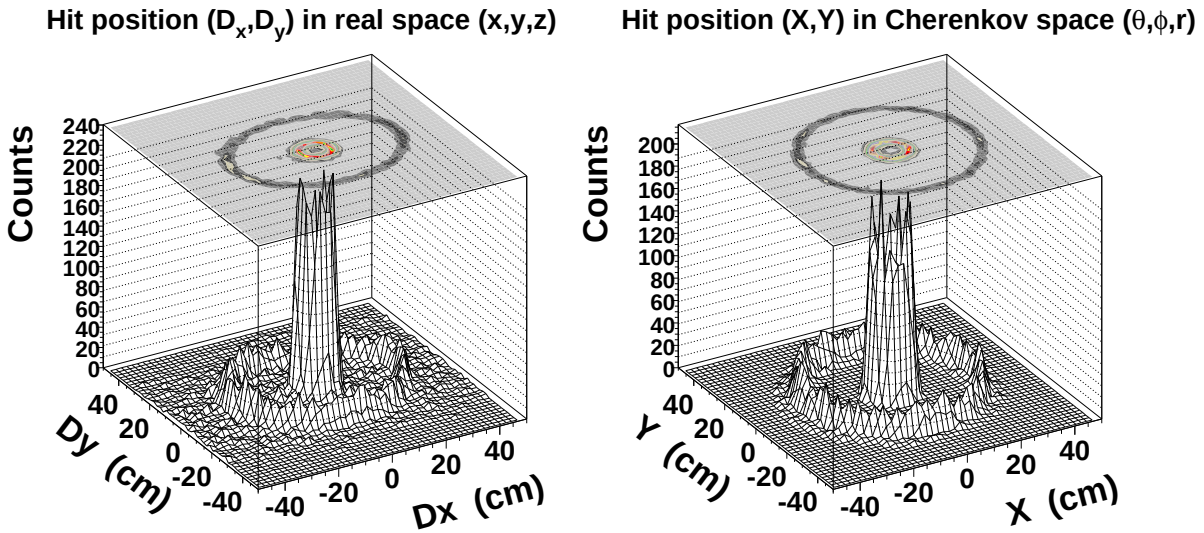

(a) (b)

Figure 5.1: The ring distributions as observed in the HERMES RICH. The rings from individual tracks are all superposed such that the track center lies at the origin. Figure (a) shows the positions where PMTs are fired on the PMT plane, (b) shows the reconstructed angle calculated by the IRT method. Both plots show events with a single lepton.

Fig.(5.1-a) shows the positions where PMTs are fired on the PMT plane. The rings from individual tracks are transposed such that the track center lies at the origin. The distribution is plotted in the real space (D_x,D_y) on the PMT plane. The ring is not a perfect circle, but roughly an ellipse. The small ring might be made by the photons which came from C_4F_{10}, and the larger ring from aerogel. However, we cannot easily recognize because the information on the emission points is lost.

We have separated the photons from the aerogel and C_4F_{10} gas as: at first, the Čerenkov angle is reconstructed by the IRT method on the two assumptions that the photon came from the center of aerogel along z-axis in HERMES coordinate system and the photon came from the middle of track in the C_4F_{10} gas. Then we obtain the two Čerenkov angle distributions. Fig.(5.2-a) and Fig.(5.2-b) show the angle distributions evaluated with each assumption. Both plots show events with a single lepton which has a momentum of $p > 5.0$ GeV/c.

Secondly, the theoretical Čerenkov angle is calculated from Eq.(3.1) as:

$$\theta_{th}^{aerogel/gas} = \cos^{-1} \frac{1}{n_{aerogel/gas}} \sqrt{1 + \left(\frac{m}{p}\right)^2} \tag{5.1}$$

where $n_{aerogel}(n_{gas})$ is the refractive index of the aerogel(C_4F_{10} gas), p is the particle momentum, and m is its mass. The theoretical Čerenkov angle can be calculated if the mass is assumed. The Čerenkov angle of the photons from the aerogel is determined in a window with the range of $[\theta_{th}^{aerogel} - \sigma_w^{aerogel}, \theta_{th}^{aerogel} + \sigma_w^{aerogel}]$. $\sigma_w^{aerogel}$ is a cut criterion which is twice as large as the single photon resolution $\sigma_\theta^{aerogel}$ in this analysis. The Čerenkov angle of which the photon from the C_4F_{10} gas is determined in the same way.

We obtain the Čerenkov angle from the aerogel θ^{aero} and from the C_4F_{10} gas θ^{gas}. In addition to the Čerenkov angle, a hit position (Dx, Dy) on the PMT plane is transformed to "Čerenkov space" (θ, ϕ, r) which is the spherical polar coordinate of the photon with respect to the particle track and r is the depth in the photon detector measured along the ray. The transformation between these systems is calculated with the IRT method. Fig.(5.1-b) show the reconstructed Čerenkov angle with the Čerenkov space of (θ, ϕ, r). The projection from (θ, ϕ, r) to (X, Y) is calculated as:

$$\begin{aligned} X &= r \tan\theta \cos\phi \\ Y &= r \tan\theta \sin\phi \end{aligned} \tag{5.2}$$

Hence, the ring becomes a perfect circle.

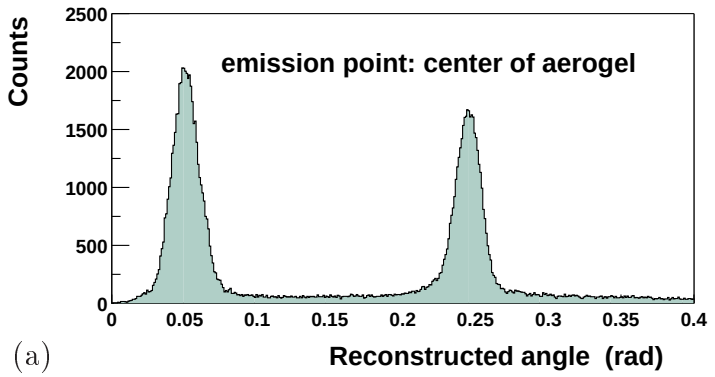

(a)

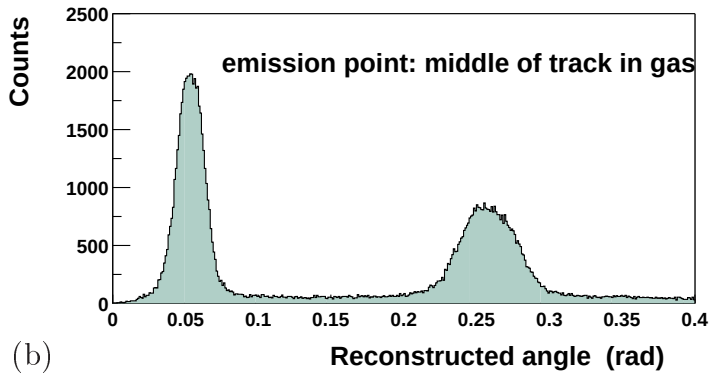

(b)

Figure 5.2: The reconstructed angle spectra. The assumptions that the photons are emitted in the aerogel (a) or in the gas (b). Both plots are from a single lepton track.

Two peaks are visible in the reconstructed angle spectra (Fig.(5.2-a) and Fig.(5.2-b)). The higher angle is from the aerogel and the lower angle from the C_4F_{10} gas. Comparing the reconstructed angle spectra on the two assumptions, the angle on the wrong assumption is broader than that on the right assumption. The upper angle on the assumption that the photon came from the gas (Fig.(5.2-b)) has twice large than that on the right assumption (Fig.(5.2-a)). This is because that the thickness of the C_4F_{10} is 75cm, while that of the aerogel is 5cm. The uncertainty of the emission point affects the width of the peaks. However, the lower angles which are expected that the photon came from the C_4F_{10} gas are almost the same in Fig.(5.2-a) and Fig.(5.2-b). The Čerenkov angle of the gas is so small that the effect of the emission point uncertainty does not have a big influence on the reconstructed angle.

The entries outside of the window $[\theta_{th} - \sigma_w, \theta_{th} + \sigma_w]$ are provided by backgrounds. From the reconstructed angle spectra in Fig.(5.2), the background ratio is estimated to be about 1 fired PMT in every 2 events.

The backgrounds are classified in three types. The first type is the photons from trackless particles. These tracks are low momentum particles that do not pass through the entire spectrometer and particles produced within the spectrometer such as delta electrons and electron-positron pairs. These "trackless rings" act as backgrounds against the rings associated with tracked particles. The second type is the several sources of background photons that do not necessarily fall on the ring structures, such as Rayleigh scattered photons, Čerenkov photons produced in the lucite. These sources are associated with their particle tracks. The third type is the noises independent of particle tracks, such as the electronic and PMT noises.

Averaged Čerenkov Angles and Resolutions

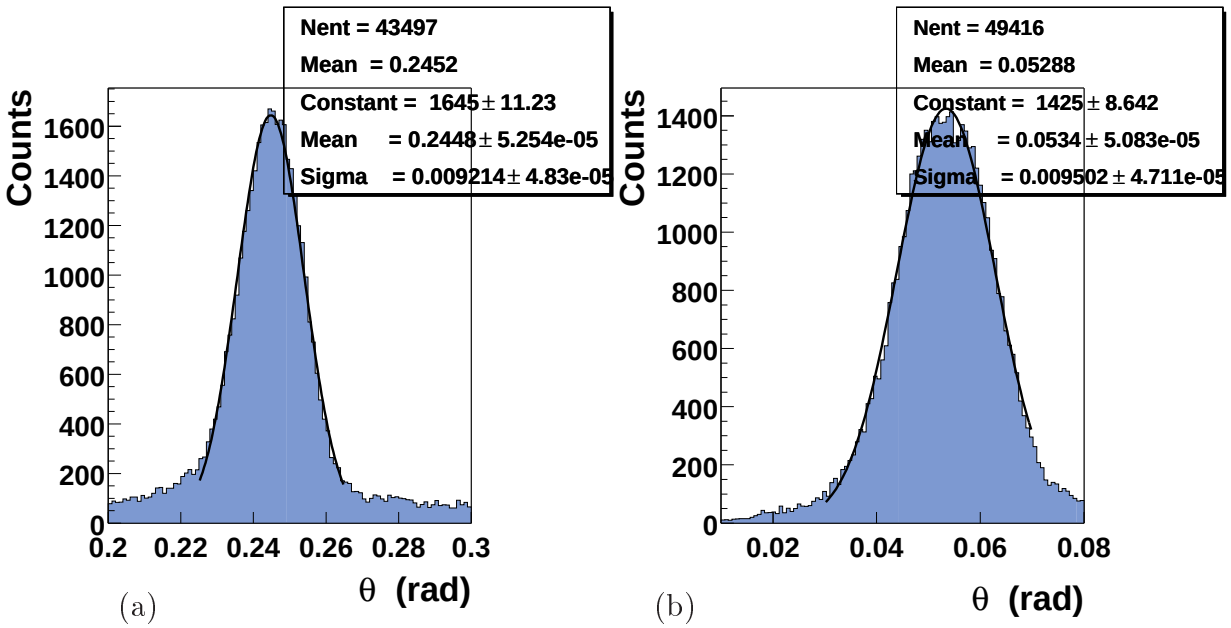

Figure 5.3: The distributions of the reconstructed Čerenkov angle. Figure (a) shows the Čerenkov angle of the photons from the aerogel, (b) shows the Čerenkov angle of the photons from the C_4F_{10} gas. Both plots are from a single lepton track.

Fig.(5.3-a) and Fig.(5.3-b) show the distributions of the reconstructed Čerenkov angle, $\theta^{aerogel}$ and θ^{gas}, respectively. These plots are from a single lepton track. The averaged angle $\langle\theta\rangle$ and its resolution σ_θ are summarized as:

radiator	$\langle\theta\rangle$ (mrad)	σ_θ (mrad)
aerogel	244	9.2
C_4F_{10}	53.4	9.5

Table 5.1: The experimental results of the averaged Čerenkov angle and the resolution (events with a single lepton, $p > 5.0$ GeV/c).

The theoretical Čerenkov angles of the aerogel $\theta^{aerogel}$ and of the C_4F_{10} gas θ^{gas} are:

$$\begin{aligned} \theta_{aerogel} &= 244 \text{ mrad} \\ \theta_{gas} &= 53.2 \text{ mrad} \end{aligned} \tag{5.3}$$

The experimental results of the averaged angle in Tab.(5.1) have good agreements with theoretical values for each radiator.

In Tab.(5.2), the expected contributions to the resolution of the reconstructed angle are listed for both radiators. The largest contribution comes from the PMT

pixel size $\Delta\theta_{pix}$ which follows from the size of the pixels of 3/4". $\Delta\theta_{em}$ is the uncertainty in the emission point along the track in the radiators. The chromatic error contribution $\Delta\theta_{chr}$ is estimated from the variation of the refractive index measured at 633 and 544 nm. Photons refracted near the edge of the aerogel tile go in an unpredictable direction. $\Delta\theta_{tile}$ is estimated from comparing the resolution for tracks that are not affected by the tile edges to those that are. $\Delta\theta_{nvar}$ is due to the variation of the refractive index between the aerogel tiles. Pressure and temperature fluctuations change the density of gas, and therefore its refractive index. $\Delta\theta_{press}$ is obtained from the observed maximum pressure fluctuations [18][19].

	aerogel	C_4F_{10}
$\Delta\theta_{pix}$	5.6	5.2
$\Delta\theta_{em}$	1.8	2.2
$\Delta\theta_{chr}$	2.5	-
$\Delta\theta_{tile}$	3.0	-
$\Delta\theta_{nvar}$	1.1	-
$\Delta\theta_{press}$	-	1.0
experimental σ_θ	9.2	9.5

Table 5.2: Contributions to the single photon resolutions of aerogel and C_4F_{10} gas (events with a single lepton, $p > 5.0$ GeV/c).

It should be stressed that the overall resolution σ_θ is not determined by a simple sum of the individual resolutions, neither a square root of the sum of resolutions squared. The sources must have large correlations by themselves. The effects should be studied by Monte Carlo simulation which will be discussed in Chap.5.2.

Number of Fired PMTs

The value that is sensitive to the efficiencies for photons is the number of fired PMTs which is denoted as N_{PMT}. Fig.(5.4) shows the distributions of the number of fired PMTs.

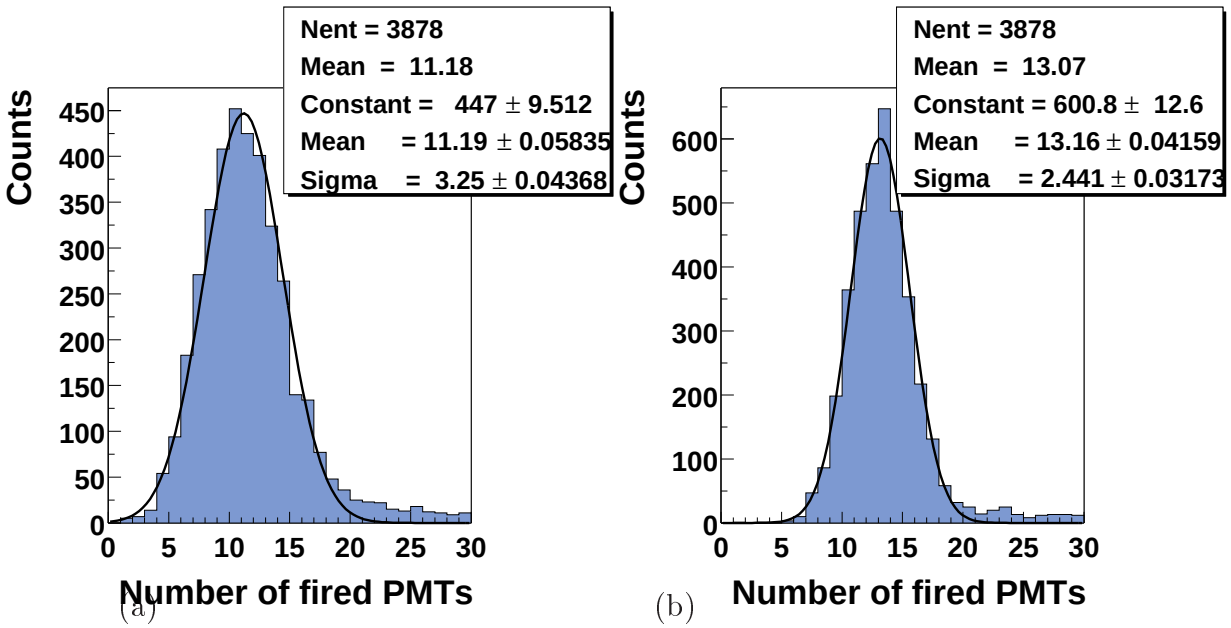

Figure 5.4: The distributions of the number of fired PMTs. Figure (a) shows the number of fired PMTs of the photons from the aerogel, (b) shows the number of the photons from the C_4F_{10} gas. Both plots are from a single lepton track.

The number of fired PMTs per a ring is an important parameter. The mean values of the fired PMTs for each radiator are listed in Tab.(5.3). The number of fired PMTs is affected by the reflection efficiencies of the mirror and the funnel. For the aerogel ring, the number of photons per a ring is proportional to the number of photons. However, for the gas ring more than 1 photons enter a PMT because the Čerenkov angle is small.

radiator	N_{PMT}
aerogel	11.2
C_4F_{10}	13.1

Table 5.3: The experimental results of the fired PMTs. (events with a single lepton, $p > 5.0$ GeV/c.)

Detector Response Parameter

The overall "detector response parameter N_0" represents a figure of merit which depends on the radiators and the efficiencies. From Eq.(3.3), the detector response parameter N_0 is given as:

$$N_0 = \frac{N_{PMT}}{Z^2 L \sin\theta} \tag{5.4}$$

where z is the charge of the particle, L is the track length in the radiator and θ is the Čerenkov angle. Fig.(5.5) shows the distributions of the detector response parameter for each radiator. Tracks of a single lepton at $p > 5.0$ GeV/c are selected.

The observed number of fired PMTs from the C_4F_{10} gas corresponds to the figure of merit $N_0^{gas} \sim 75\text{cm}^{-1}$. The number from the aerogel indicates $N_0^{aerogel} \sim 40\text{cm}^{-1}$.

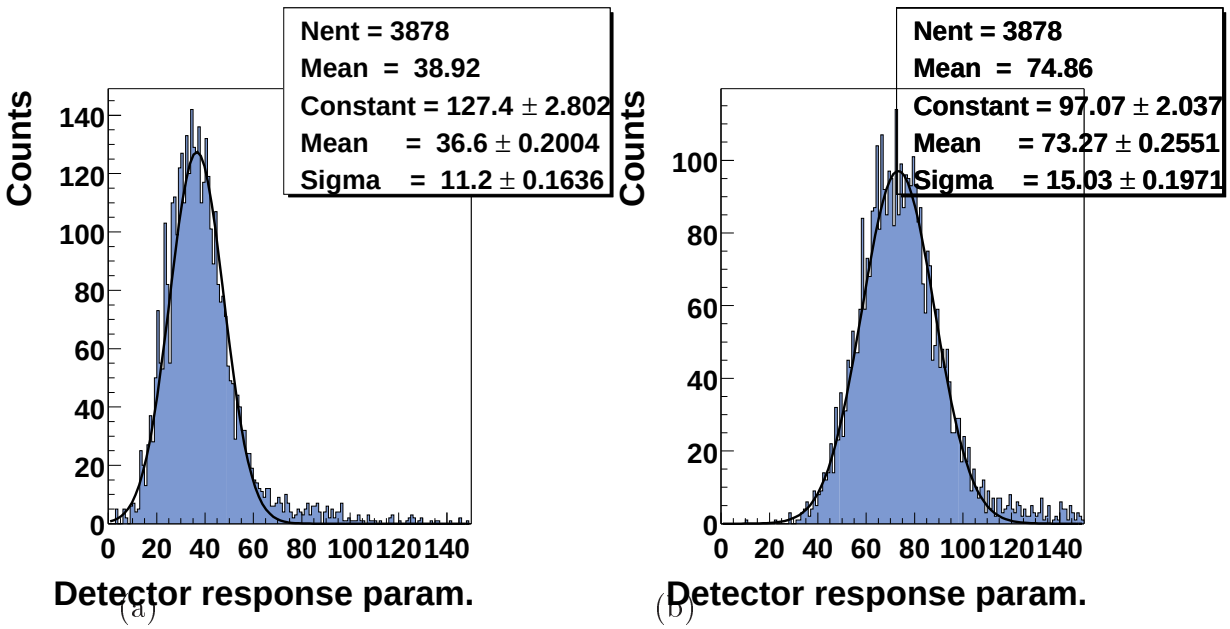

Figure 5.5: The distributions of the detector response parameter N_0. The photons are emitted in the aerogel (a) and in the C_4F_{10} gas (b).

Fig.(5.6) shows the distributions of particle velocity β reconstructed as $\beta = 1/n\cos\theta$. Since these are events with a single lepton ($p > 5.0$ GeV/c), the values must be 1. However, the resolution of the reconstructed angle also affects the distribution of β.

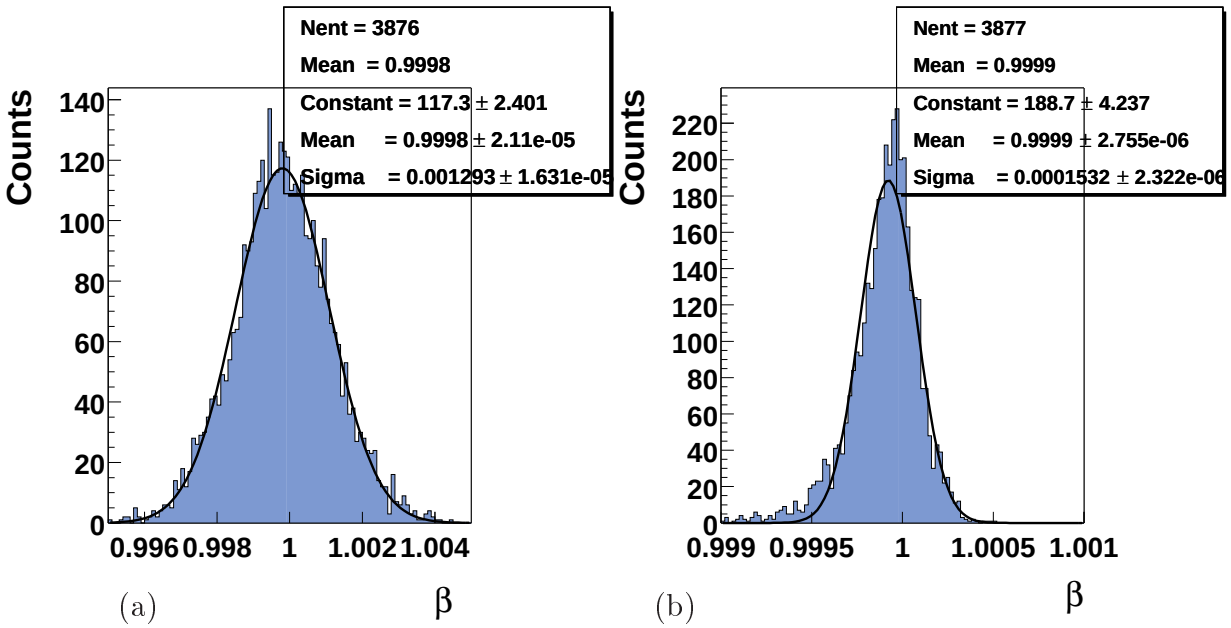

Figure 5.6: The distributions of the reconstructed velocity β of leptons. The photons are emitted in the aerogel (a) and in the C_4F_{10} gas (b).

The observed resolutions are listed in Tab.(5.4).

radiator	$\sigma_\beta/10^{-4}$
aerogel	13.0
C_4F_{10}	1.5

Table 5.4: The experimental results of the resolutions of β. (events with a single lepton, $p > 5.0$ GeV/c.)

The resolution of β gives a simple and direct performance test of the particle identification. From Eq.(3.15), the resolution of β is equal to the RICH counter constant κ_r. From Eq.(3.13), the maximum momentum p_{max} at which the discrimination of π, K and p with 4 standard deviation is possible is calculated as:

$$\begin{aligned} p_{max}^{aerogel}[\pi,K] &= \sqrt{\frac{m_K^2 - m_\pi^2}{2\cdot 4\cdot \sigma_\beta^{aerogel}}} = 4.6 \text{ GeV/c} \\ p_{max}^{aerogel}[K,p] &= = 8.5 \text{ GeV/c} \\ p_{max}^{gas}[\pi,K] &= \sqrt{\frac{m_K^2 - m_\pi^2}{2\cdot 4\cdot \sigma_\beta^{gas}}} = 14 \text{ GeV/c} \\ p_{max}^{gas}[K,p] &= = 25 \text{ GeV/c} \end{aligned} \tag{5.5}$$

In the practical particle identification method, particles are identified with the likelihood technique using combined the information of the aerogel and C_4F_{10}. The maximum momentum for π, K and p separation cannot be simply determined. The maximum momentum for π, K and p separation is about 15 GeV/c.

The numerical value of the performance is summarized in Tab.(5.5). It gives us a simple comparison between the aerogel and the C_4F_{10} gas.

	Material	
	aerogel	C_4F_{10}
n	1.0303	1.00137
θ_c^{max} (mrad)	243	52.3
$p_{thre.}[\pi]$ (GeV/c)	0.6	2.7
$p_{thre.}[K]$ (GeV/c)	2.0	9.4
$p_{thre.}[p]$ (GeV/c)	3.8	17.9
N_{PMT}	11.2	13.1
N_0	~ 40	~ 75
σ_θ^{track} (mrad)	9.2	9.5
$\sigma_\beta^{track}/10^{-4}$	13.0	1.5

Table 5.5: Some characteristics of the radiator materials used in the HERMES RICH; the thresholds for each hadron and the resolution of θ_c and β from the experimental results.

Mass Distributions

As is shown in Fig.(5.1), the Čerenkov angle has a relation to the particle momentum. Fig.(5.7) shows the momentum distribution of the Čerenkov angle of π, K and p. The upper three bands are from the aerogel, the lower bands from the C_4F_{10} gas.

In the momentum range of $4 < p < 7$ GeV/c, π-K separation is mainly performed with the information of the Čerenkov angle. The tails of the reconstructed Čerenkov angle distributions of π and K in this region are overlapping. We have optimized the window σ_w to separate the distributions and chosen twice the single photon resolution; $\sigma_w = 2 \times \sigma_\theta$.

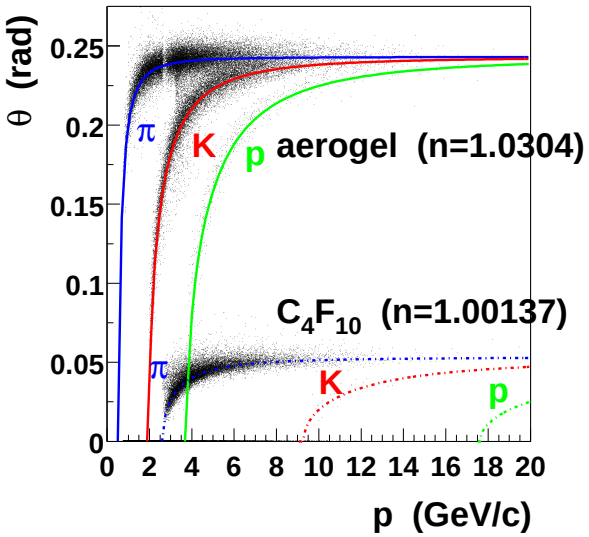

Figure 5.7: The momentum dependence of the Čerenkov angle in the HERMES RICH for different particles (Experimental data). Points represent data, line - theoretical curves.

From Eq.(3.1) and Eq.(3.11), the mass m of the particle can be written as:

$$m = p\sqrt{n^2 \cos^2\theta - 1} \tag{5.6}$$

Fig.(5.8-a) and Fig.(5.8-b) show the momentum distribution of the particle mass which is evaluated from Eq.(5.6). The horizontal axis is the particle mass squared, which is calculated using reconstructed Čerenkov angles as $m^2 = p^2(n^2 \cos^2\theta - 1)$. The vertical axis is the momentum p of the particle. Fig.(5.8-a) is the result of the reconstructed Čerenkov angle of the aerogel, and Fig.(5.8-b) of the C_4F_{10} gas. The bands represent the mass of π, K and p from the left to the right.

These plots give us a clean overview on how the particle identification can be realized. From the momentum range of $p > 2$ GeV/c, π-K separation is performed using the Čerenkov angle and the threshold of the aerogel (Fig.(5.8-a)). From $p > 3$ GeV/c, it becomes possible to identify all hadrons (π,K and p). At higher momentum region of $p > 4$ GeV/c, π and K are not separable with aerogel. But, above this momentum the identification using the Čerenkov angle and threshold of the C_4F_{10} gas can be performed (Fig.(5.8-b)).

aerogel C_4F_{10}

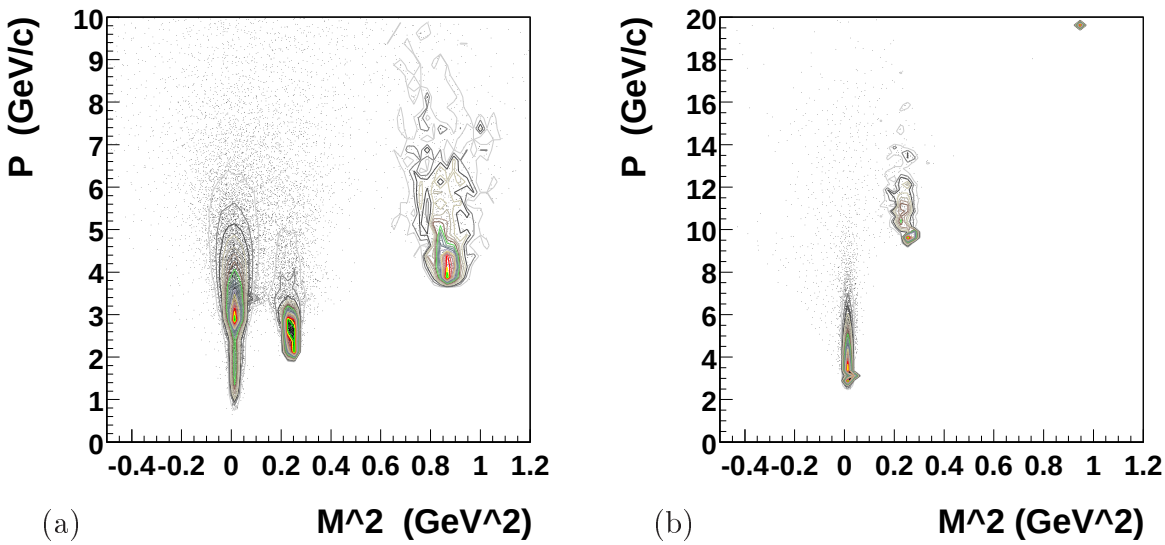

(a) (b)

Figure 5.8: The momentum distributions of the particle mass. The left plot is evaluated from the reconstructed angle of the aerogel, the right from the C_4F_{10} gas. (The horizontal axis is the particle mass squared, which is calculated using reconstructed Čerenkov angle as $m^2 = p^2(n^2 \cos^2\theta - 1)$. The vertical axis is the momentum p of the particle.)

5.2 The Performance of the MC Simulation

The reconstructed Čerenkov angle θ and the number of fired PMTs N_{PMT} are essential values for the particle identification. It is important to compare these values with MC.

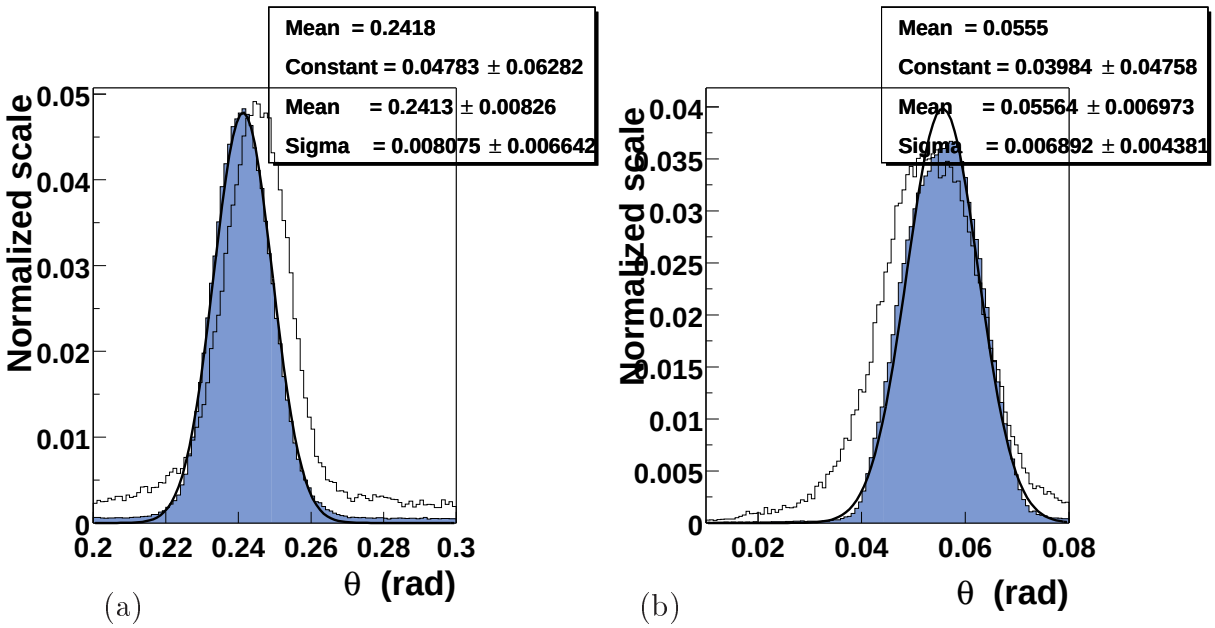

Figure 5.9: The distributions of the reconstructed Čerenkov angle of MC data (shaded histograms). Events are from single lepton tracks with $p > 5.0$ GeV/c. The left plot shows the Čerenkov angle from the aerogel, and the right the Čerenkov angle from the C_4F_{10} gas. The experimental results (normal histograms) are superimposed for comparison.

Fig.(5.9) shows the distributions of reconstructed angle, $\theta^{aerogel}$ and θ^{gas}. Events with single electrons at $p > 5.0$ GeV/c are selected. The numerical values are listed in Tab.(5.6).

	$\theta^{aerogel}$	$\pm$	$\sigma_\theta^{aerogel}$	θ^{gas}	$\pm$	σ_θ^{gas}
MC	241	$\pm$	8.1	55.6	$\pm$	6.7
Experimental	244	$\pm$	9.2	53.4	$\pm$	9.5
Theoretical	244	-	-	53.2	-	-

Table 5.6: The numerical values of the reconstructed Čerenkov angle for MC and experimental results.

The resolutions have a difference between the MC and the experimental data. The main reason is the effect at the edge of the aerogel tiles because the latest HMC which includes this effect provides good agreements (AppendixB).

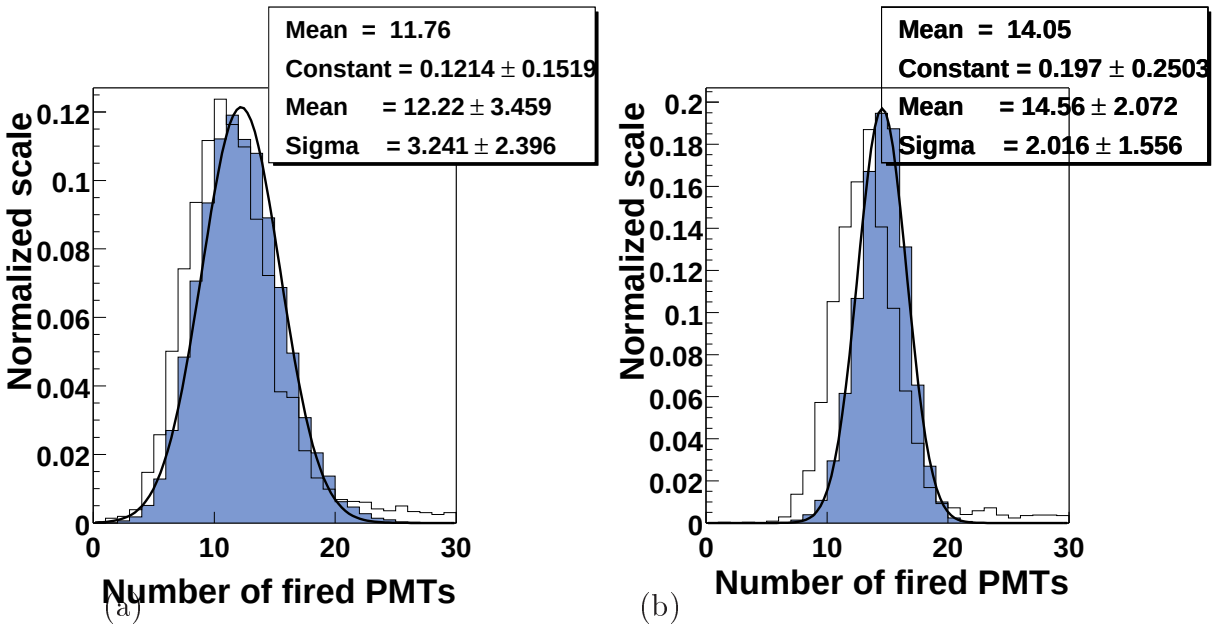

Figure 5.10: The distributions of the number of fired PMTs N_{PMT} of MC data (shaded histograms). Events are from single lepton tracks with $p > 5.0$ GeV/c. The left plot shows N_{PMT} from the aerogel, and the right N_{PMT} from the C_4F_{10} gas. The experimental results (normal histograms) are superimposed for comparison.

Fig.(5.10) shows the distributions of the number of fired PMTs of the MC data. The numerical values of the MC and the experimental results are listed in Tab.(5.7). The number of fired PMTs is mainly affected by the mirror reflectivity. After the MC was upgraded as discussed in Chap.3.3.1, the numbers of fired PMTs from each radiator, N_{PMT}^{aerogl} and N_{PMT}^{gas} are close to the experimental results. However, the MC data does not reproduce the large tail of the experimental data. The reason is that the MC does not treat the backgrounds such as Čerenkov photons produced in the lucite and the electronic and PMT noises which are independent of particle tracks.

	N_{PMT}^{aero}	N_{PMT}^{gas}
MC	11.8	14.1
Experimental	11.2	13.1

Table 5.7: The numerical values of the reconstructed Čerenkov angle for MC and experimental Results.

Chapter 6

PID Efficiency and Purity

As described in Chap.4, two PID algorithms have been developed for the HERMES RICH. It is necessary to define a PID evaluation parameter to compare the algorithms. The "efficiency" and "purity" are useful to estimate the detector performance. They will be described in the following section. In brief, efficiency is the probability that a particle is correctly identified. Purity is the probability that an identified particle is truly of that particle type.

6.1 How to Calculate P- and Q- Matrix

Every particle is labeled with the identified particle type. On the other hand, each particle has a true particle type. We define the number of particles N_t^i. t is the true particle type and i is the identified particle type.

$$N_t^i \quad \begin{matrix} \leftarrow \text{identified particle type} \\ \leftarrow \text{true particle type} \end{matrix} \tag{6.1}$$

These numbers N_t^i form a matrix $\boldsymbol{N}$:

$$\boldsymbol{N} = \begin{pmatrix} N_\pi^\pi & N_K^\pi & N_p^\pi \\ N_\pi^K & N_K^K & N_p^K \\ N_\pi^p & N_K^p & N_p^p \end{pmatrix} \tag{6.2}$$

Now we define the "identification probability P_t^i" as the ratio of N_t^i to the sum of the identified particle type, which is written as [20]:

$$P_t^i = \frac{N_t^i}{\sum_j N_t^j} \tag{6.3}$$

A matrix $\boldsymbol{P}$ has the elements P_t^i:

$$\boldsymbol{P} = \begin{pmatrix} P_\pi^\pi & P_K^\pi & P_p^\pi \\ P_\pi^K & P_K^K & P_p^K \\ P_\pi^p & P_K^p & P_p^p \end{pmatrix} \tag{6.4}$$

The columns of the matrix are normalized to 1.

$$\sum_i P_t^i = \sum_i \frac{N_t^i}{\sum_j N_t^j} = 1 \tag{6.5}$$

On the other hand, the "true type probability Q_t^i" can be defined as the ratio of N_t^i to the sum of the true particle type as:

$$Q_t^i = \frac{N_t^i}{\sum_s N_s^i} \tag{6.6}$$

The matrix $\boldsymbol{Q}$ is written as:

$$\boldsymbol{Q} = \begin{pmatrix} Q_\pi^\pi & Q_\pi^K & Q_\pi^p \\ Q_K^\pi & Q_K^K & Q_K^p \\ Q_p^\pi & Q_p^K & Q_p^p \end{pmatrix} \tag{6.7}$$

The columns of the matrix $\boldsymbol{Q}$ are normalized to 1.

$$\sum_t Q_t^i = \sum_t \frac{N_t^i}{\sum_s N_s^i} = 1 \tag{6.8}$$

For example, P_π^{p} means the probability that a true pion is misidentified as a proton. Q_π^{p} is the probability that a particle which is identified as a proton is truly pion.

6.1.1 General Formalism

From Eq.(6.6), the Q-matrix is connected simply via the P-matrix and the flux factors:

$$Q_t^i = \frac{N_t^i}{\sum_s N_s^i} = \frac{N_t^i \frac{1}{\sum_{s'} N_{s'}}}{\sum_s N_s^i \frac{1}{\sum_{s'} N_{s'}}} = \frac{\frac{N_t^i}{\sum_{i'} N_t^{i'}} \frac{\sum_{i'} N_t^{i'}}{\sum_{s'} N_{s'}}}{\sum_s \frac{N_s^i}{\sum_{i'} N_s^{i'}} \frac{\sum_{i'} N_s^{i'}}{\sum_{s'} N_{s'}}} = \frac{P_t^i \phi_t}{\sum_s P_s^i \phi_s} \tag{6.9}$$

With $N_t = \sum_{i'} N_t^{i'}$ the flux factors are defined as:

$$\phi_t = \frac{N_t}{\sum_s N_s} \tag{6.10}$$

The flux factors describe how many true particles are crossing the RICH. They are determined by the production cross sections in DIS and the acceptance of the detector.

The identification "efficiency ϵ_t" is the probability that a particle type t is identified correctly, and is the diagonal element of the P-matrix.

$$\epsilon_t = P_t^t \tag{6.11}$$

On the other hand the "purity $\mathcal{P}^i$" is the percentage of correctly identified particle in a sample of the identified particle type. The purity is the diagonal element of the Q-matrix.

$$\mathcal{P}^i = Q^i_i \tag{6.12}$$

The elements of P- and Q-matrices defined in Eq.(6.3),Eq.(6.6) are expressed with the number of particles N^i_t that is tagged by the identified particle type i and the true particle type t. As discussed in AppendixA, the statistical errors of P- and Q-matrices can be written as:

$$\delta P^i_t = \sqrt{\left\{ (\frac{1}{\sum_{k'} N^{k'}_t})^2 - 2\frac{1}{\sum_{k'} N^{k'}_t}\frac{N^i_t}{(\sum_{k'} N^{k'}_t)^2} \right\} \cdot N^i_t + \frac{(N^i_t)^2}{(\sum_{k'} N^{k'}_t)^4} \sum_k N^k_t} \tag{6.13}$$

$$\delta Q^i_t = \sqrt{\left\{ (\frac{1}{\sum_{s'} N^i_{s'}})^2 - 2\frac{1}{\sum_{s'} N^i_{s'}}\frac{N^i_t}{(\sum_{s'} N^i_{s'})^2} \right\} \cdot N^i_t + \frac{(N^i_t)^2}{(\sum_{s'} N^i_{s'})^4} \sum_s N^i_s} \tag{6.14}$$

6.1.2 Monte Carlo Analysis

One of the ways to make P- and Q-matrices is to use a Monte Carlo(MC). The advantage of MC is that the true particle types of tracks are known. Each track is tagged with the true particle type and the identified particle type. A list of the numbers is shown in Tab.(6.1). The incident particles are π, K, p and e. The identified particle types of the RICH are π, K, p and X(not-identified). The efficiency and purity values are listed together in the table.

		true particle type				$\mathcal{P}$
		π	K	p	e	
identified as	π	517204	6800	19485	6407	0.975
	K	14528	52673	15092	211	0.899
	p	5747	4937	72090	49	0.912
	X	7197	5246	23166	737	
ϵ		0.976	0.927	0.863		

Table 6.1: An example for the N-matrix together with efficiencies and purities.

With the Eq.(6.3), the matrix of Tab.(6.1) is converted into the P-matrix. It is expressed as follows:

$$P = \begin{pmatrix} P^\pi_\pi & P^\pi_K & P^\pi_p & P^\pi_e \\ P^K_\pi & P^K_K & P^K_p & P^K_e \\ P^p_\pi & P^p_K & P^p_p & P^p_e \\ P^X_\pi & P^X_K & P^X_p & P^X_e \end{pmatrix} = \begin{pmatrix} 0.976 & 0.018 & 0.070 & 0.925 \\ 0.002 & 0.927 & 0.076 & 0.028 \\ 0.013 & 0.069 & 0.863 & 0.007 \\ 0.010 & 0.020 & 0.010 & 0.050 \end{pmatrix} \tag{6.15}$$

The Q-matrix is calculated from Eq.(6.6):

$$Q = \begin{pmatrix} Q_\pi^\pi & Q_\pi^K & Q_\pi^p & Q_\pi^X \\ Q_K^\pi & Q_K^K & Q_K^p & Q_K^X \\ Q_p^\pi & Q_p^K & Q_p^p & Q_p^X \\ Q_e^\pi & Q_e^K & Q_e^p & Q_e^X \end{pmatrix} = \begin{pmatrix} 0.976 & 0.012 & 0.041 & 0.088 \\ 0.007 & 0.899 & 0.040 & 0.074 \\ 0.018 & 0.090 & 0.912 & 0.838 \\ 0.010 & 0.010 & 0.020 & 0.020 \end{pmatrix} \tag{6.16}$$

6.1.3 Decaying Particle Analysis

The P-matrix can be determined from a decaying particle analysis. To obtain a set of true pions, kaons and protons, we select the following decays:

$$\begin{aligned} \rho &\to \pi^+ + \pi^- \\ \phi &\to \mathrm{K}^+ + \mathrm{K}^- \\ \Lambda &\to \mathrm{p}^+ + \pi^- \\ \mathrm{K}_s^0 &\to \pi^+ + \pi^- \end{aligned}$$

As an example, the decay $\phi \to \mathrm{K} + \mathrm{K}$ will be described below:

We can obtain the invariant mass distribution with a $\mathrm{K} + \mathrm{K}$ assumption. The mass peak at ϕ meson mass is constructed by a pair of true $\mathrm{K} + \mathrm{K}$. Due to a misidentification by the RICH, some particles in the mass peak are identified as other particles (π or p). To get the P-matrix, the counts in the mass peak are separated as the following sets of the particles: both are identified as kaons (K,K), one is identified as a kaon and the other is identified as a pion (π,K), as a proton (p,K) and as a not-identified particle (X,K). (H,K) is the sum of these.

$n(H_1, H_2)$ denotes the total number of the hadron sets. The ratios give the column of the P-matrix for true Kaon as:

$$\begin{aligned} \epsilon_K \;=\; P_K^K &= n(K,K)/n(H,K) \\ P_K^\pi &= n(\pi,K)/n(H,K) \\ P_K^p &= n(p,K)/n(H,K) \\ P_K^X &= n(X,K)/n(H,K) \end{aligned} \tag{6.17}$$

The other columns; P_π^h and P_p^h are obtained using ρ and Λ decays.

6.2 Unfolding the Counts of Identified Hadrons

Identified particles are grouped in the four types: π, K, p and not-identified "X".

$$\vec{I} = (I_\pi, I_\mathrm{K}, I_\mathrm{p}, I_\mathrm{X}) \tag{6.18}$$

are the counts of identified hadrons. However, one cannot know the true particle type. The counts of the true particles are grouped as follows:

$$\vec{N} = (N_\pi, N_\mathrm{K}, N_\mathrm{p}) \tag{6.19}$$

The P- and Q-matrices connect the identified particle vector $\vec{I}$ and the true particle vector $\vec{N}$ as:

$$\vec{I} = P \cdot \vec{N} \tag{6.20}$$

$$\vec{N} = Q \cdot \vec{I} \tag{6.21}$$

From Eq.(6.21), one can derive the counts of the true hadrons from the number of hadrons identified with the RICH via the Q-matrix. The identification performance of the RICH should be a function of momentum because Čerenkov angle is momentum dependent as shown in Fig.(4.2). Thus, the vector of the identified counts $\vec{I}$, the P- and Q-matrices are determined as functions of momenta. At the end, we will obtain the momentum spectra of the true particles.

Correction to the Hadron Production Asymmetry

To calculate the hadron production asymmetry A_1^h as defined in Eq.(1.34) from actual data one must take into account the imperfect polarizations of the beam and the target, depolarization factors of the virtual photon and the acceptance effects. The relation between the asymmetry and the counts of a particle type h is written as:

$$A_1^h = \frac{N_h^+ \mathcal{L}^- - N_h^- \mathcal{L}^+}{N_h^+ \bar{\mathcal{D}}^- \mathcal{L} P^- + N_h^- \bar{\mathcal{D}}^+ \mathcal{L} P^+} \tag{6.22}$$

where $N_h^\pm$ are the total hadron counts in each spin state. $\mathcal{L}^\pm$ are the luminosity factors, while $\mathcal{L}P^\pm$ represent the luminosities multiplied by the beam and target polarizations. $\bar{\mathcal{D}}^\pm$ are the averaged depolarization factors defined in Chap.1.4.

The luminosities, $\mathcal{L}$ and $\mathcal{L}P$ are determined with the actual data regardless of the particle types identified with the RICH. However, the depolarization factor $\mathcal{D}$ and the counts of the detected particles N are determined for each particle type of detected hadrons and their kinematic values. It is important to correct the counts of the detected particles using the Q-matrix.

6.3 PID Efficiency and Purity Study with MC

As shown in Fig.(4.2) the Čerenkov threshold and the angle have a relation to momentum of charged particles. Therefore the performance of the hadron identification is a function of momentum.

6.3.1 PID Efficiency from MC Data

The efficiency is studied with MC as follows:

- The detector simulation with GEANT is already described in Chap.3.3 and Chap.3.3.1.

- To separate electron-hadron samples using TRD, calorimeter and preshower counters, we apply the following cuts:

$$\begin{array}{lcll} PID2 + PID5 & > & 2.0 & \text{for leptons} \\ PID2 + PID5 & < & 0.0 & \text{for hadrons} \end{array} \tag{6.23}$$

- Ignore not-identified particle X: with the RICH identification algorithm we obtain the identified particle type for each track. We ignore the not-identified particles with a quality parameter cut $Qp > 0.0$.

Then we obtain the 3×3 matrix of N. Tab.(6.2) shows a result of the N-matrix. The IRT likelihood technique is used in the whole momentum region(0-30 GeV/c). The number of the true electron is in the table for comparison but it is not taken into account when the efficiencies(diagonal elements of the P-matrix) and the purities(diagonal elements of the Q-matrix) are calculated. The statistical errors of the efficiency and the purity are evaluated from the equations as (AppendixA):

$$\delta P_t^i = \sqrt{\left\{ (\frac{1}{\sum_{k'} N_t^{k'}})^2 - 2\frac{1}{\sum_{k'} N_t^{k'}} \frac{N_t^i}{(\sum_{k'} N_t^{k'})^2} \right\} \cdot N_t^i + \frac{(N_t^i)^2}{(\sum_{k'} N_t^{k'})^4} \sum_k N_t^k} \tag{6.24}$$

$$\delta Q_t^i = \sqrt{\left\{ (\frac{1}{\sum_{s'} N_{s'}^i})^2 - 2\frac{1}{\sum_{s'} N_{s'}^i} \frac{N_t^i}{(\sum_{s'} N_{s'}^i)^2} \right\} \cdot N_t^i + \frac{(N_t^i)^2}{(\sum_{s'} N_{s'}^i)^4} \sum_s N_s^i} \tag{6.25}$$

where N_t^i are the elements of the N-matrix.

		true particle type				$\mathcal{P}$
		π	K	p	e	
id. as	π	542227	7118	20485	6688	0.9516±0.0003
	K	15195	55163	15818	222	0.640±0.002
	p	6012	5185	75641	52	0.871±0.001
ϵ		0.9623±0.0003	0.817±0.001	0.676±0.001		

Table 6.2: The result of the N-matrix (IRT, $Qp > 0.0$, positive and negative charged particles in the momentum range of 0-30 GeV/c).

The results show the efficiencies of $\epsilon_\pi = 0.962$, $\epsilon_K = 0.817$ and $\epsilon_p = 0.676$. The efficiency and purity are expected to be functions of momentum. These values become much higher when we select the higher momentum region as we do in the actual data analysis.

6.3.2 Factors Influencing PID Efficiency

We need to study the effects which affect the efficiency of the particle identification. The properties influencing the identification algorithm are listed as follows:

- **PID algorithms: IRT and DRT** are different identification techniques. Using the DRT method it is possible to estimate where the image of the Čerenkov ring would be. However the amount of CPU time for calculation is smaller for IRT than DRT.

- **The quality parameter** is the decadic logarithm of the ratio of the highest and the second highest likelihoods, $Qp = \log_{10} \frac{L_1}{L_2}$. A cut on the quality parameter affects the performance of the particle identifications.

- **Track multiplicities:** The number of tracks is selected as 1,2,>2 per a detector half. When more than 1 tracks enter the RICH, photons from other tracks will become backgrounds.

From the view of the efficiency(the P-matrix), we have checked the effects of the possible properties described above. In the following section these effects are explained.

Possible PID Methods (IRT,DRT)

Two approaches have been developed to identify hadrons: IRT and DRT. The DRT method takes into account multiple tracks and overlapping rings. On the contrary, the IRT method is faster than the DRT and works fine when rings do not overlap.

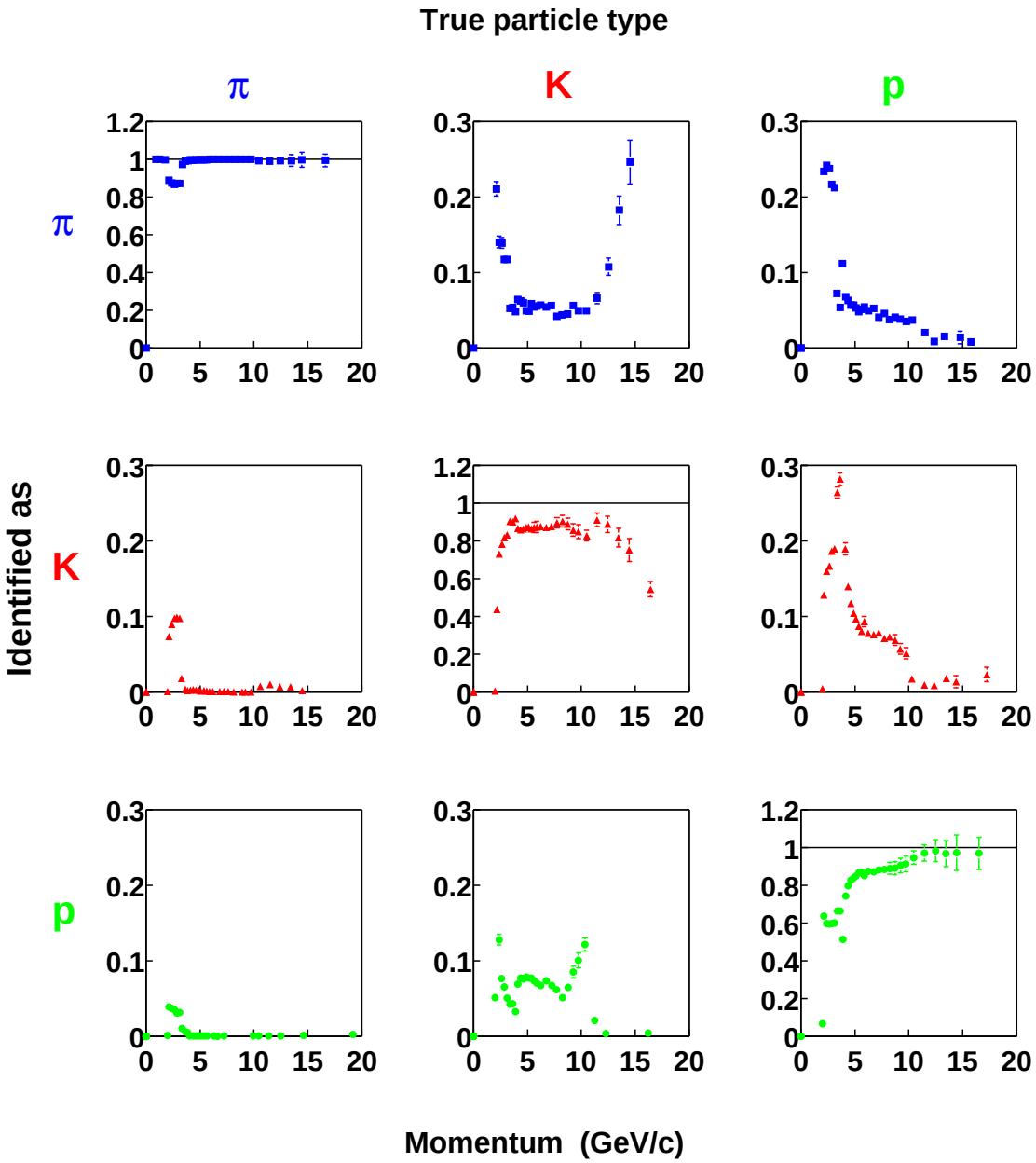

Figure 6.1: Identification efficiencies(the P-matrix) using the **IRT** method ($Qp > 0.0$).

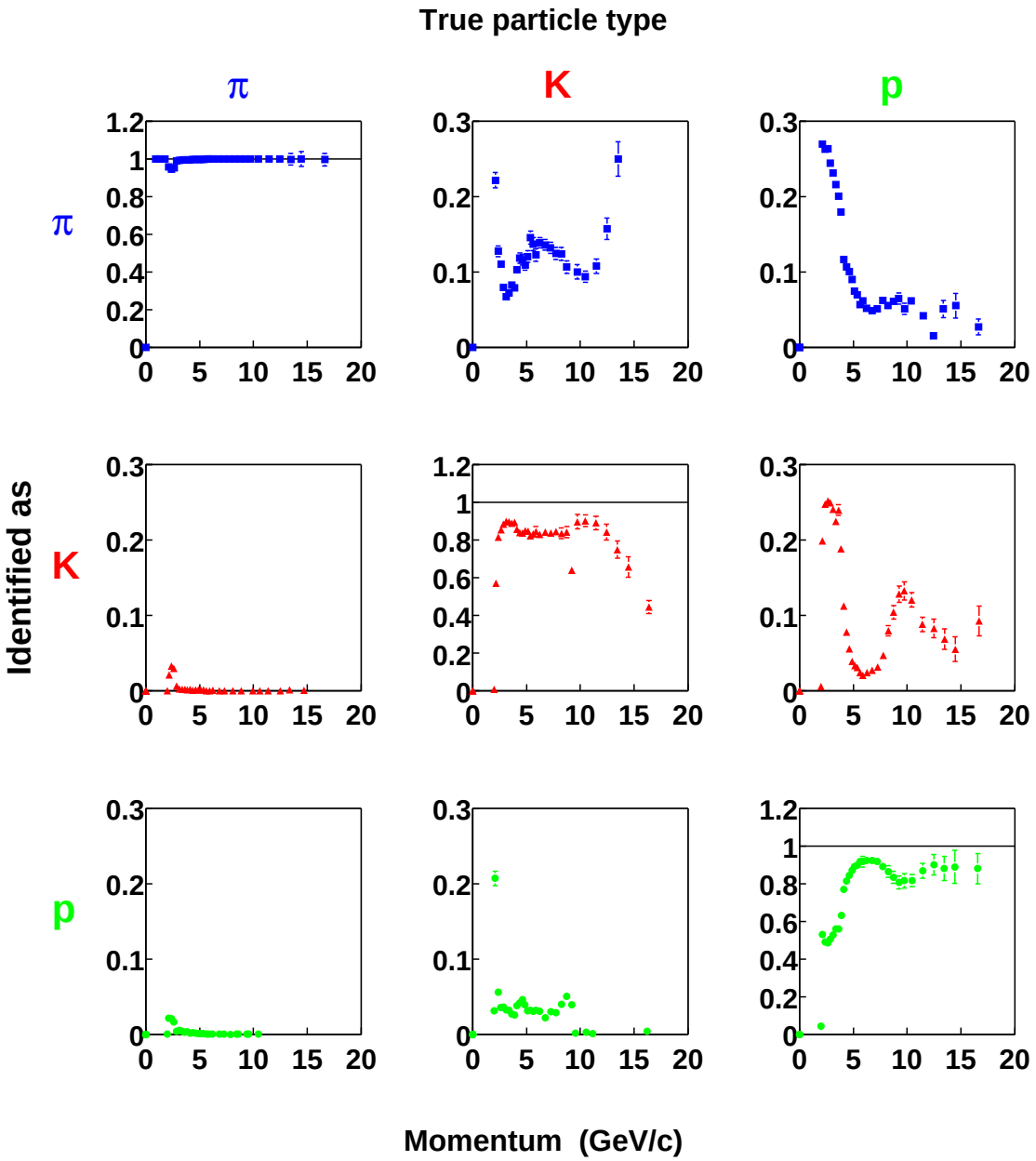

Figure 6.2: Identification efficiencies(the P-matrix) using the **DRT** method ($Qp > 0.0$).

The P-matrix elements using IRT and DRT are shown in Fig.(6.1) and Fig.(6.2). The efficiency of pion is more than 99% in the whole range of momentum. The efficiency of kaon with the IRT is about 3% bigger than that of the DRT. The difference becomes large in the high momentum region. As for the efficiency of proton, the result of the IRT method shows the efficiency increases gradually as the momentum increases, from 80% to 99%.

PID Quality Parameter

The quality parameter is the decadic logarithm of the ratio of the highest and the second highest likelihoods, $Qp = \log_{10} \frac{L_1}{L_2}$. This definition has a simple interpretation. It states that the identification efficiency goes up as the quality parameter increases. Hence, a cut on the quality parameter affects the performance of the particle identification.

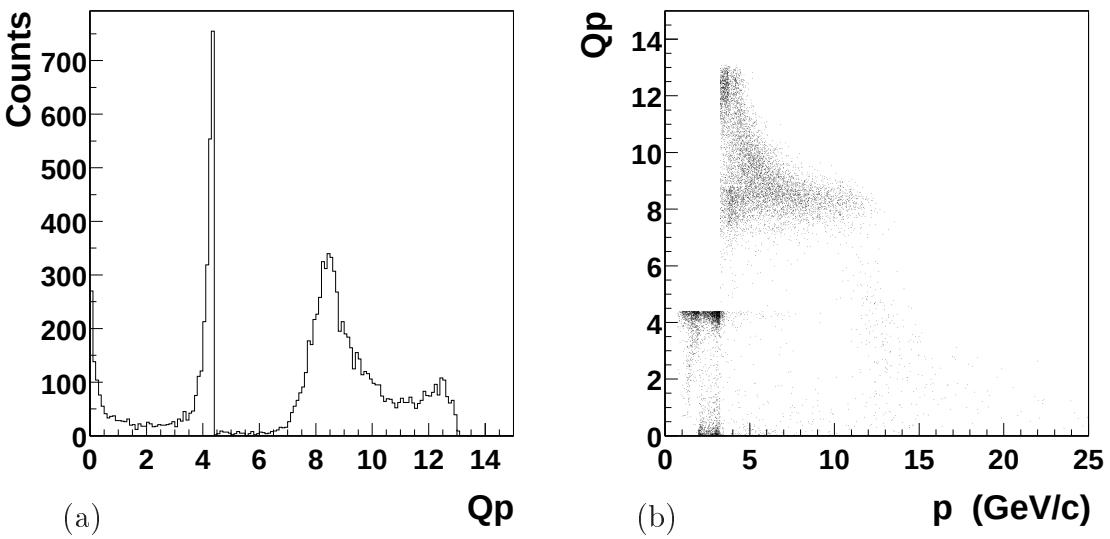

Figure 6.3: The distributions of the quality parameter. The left plot shows the distribution of the quality parameter, and the right plot shows the momentum distribution of the quality parameter. (The results from the MC simulation.)

Fig.(6.3-a) shows the distribution of the quality parameter. The distribution has two peaks at the values of 4.3 and 8.5. To explain this distribution, it is necessary to check the momentum distribution of the quality parameter as shown in Fig.(6.3-b). The threshold informations of the two radiators are used in the momentum range from 2 to 4 GeV/c. The maximum value of the quality parameter should be given as:

$$\log_{10}\left(L_{min}^{aerogel} \cdot L_{min}^{gas}\right) = 4.34 \tag{6.26}$$

where L_{min} is the minimum value of the likelihood as discussed in Chap.4.3.1. Hence, the quality parameter is cut off at this value. In the momentum range from 4 to 10 GeV/c, the Čerenkov angle of the aerogel and the threshold information of the C_4F_{10} gas are used. Because the Čerenkov angles of π, K and p are close with each other as the momentum increases, the quality parameter decreases and reaches the expected minimum value as:

$$\log_{10}\left(L(\langle\theta_{th}\rangle)^{aerogel} \cdot L_{min}^{gas}\right) = 8.5 \tag{6.27}$$

Similarly, in the momentum range above 10 GeV/c, the Čerenkov angles of both aerogel and C_4F_{10} gas are used. The quality parameter decreases as the momentum increases and reaches the expected value as:

$$\log_{10}\left(L(\langle\theta_{th}\rangle)^{aerogel}\cdot L(\langle\theta_{th}\rangle)^{gas}\right)=0.0 \tag{6.28}$$

We have applied some cuts on the quality parameter, $Qp > 0.0, 0.5, 1.0, 1.5, 2.0, 2.5, 3.0$. Tab.(6.3) and Tab.(6.4) show the numerical values of the averaged efficiencies, diagonal elements of the P-matrix for each cut on the quality parameter. The efficiencies of pion and proton increase as the quality parameter increases. On the contrary, in the results from IRT, the efficiency of kaon has a maximal value of 85.8% at $Qp = 1.0$, and decreases as the quality parameter increases. The numerical values of overall efficiencies suggest that $Qp > 1.0$ is a suitable cut.

	$Qp >$	0.0	0.5	1.0	1.5	2.0	2.5	3.0
	$\pi^{\pm}$	96.2±0.1	98.3±0.1	98.5±0.1	98.6±0.1	98.6±0.1	98.6±0.1	98.7±0.1
ϵ_t	$K^{\pm}$	81.8±0.1	85.3±0.1	85.8±0.1	85.6±0.2	85.2±0.2	84.9±0.2	84.5±0.2
	$p/\bar{p}$	67.6±0.1	70.6±0.1	71.6±0.1	72.2±0.1	72.7±0.1	73.2±0.2	74.0±0.2

Table 6.3: Integrated efficiencies over whole momentum range(IRT): averaged values in the momentum range of $0-30$ GeV/c.

	$Qp >$	0.0	0.5	1.0	1.5	2.0	2.5	3.0
	$\pi^{\pm}$	98.9±0.1	99.1±0.1	99.3±0.1	99.5±0.1	99.6±0.1	99.6±0.1	99.7±0.1
ϵ_t	$K^{\pm}$	80.4±0.2	81.8±0.1	83.2±0.2	84.3±0.1	85.1±0.1	85.7±0.1	86.1±0.2
	$p/\bar{p}$	62.3±0.1	62.9±0.1	62.8±0.2	61.6±0.2	59.1±0.2	55.4±0.2	54.9±0.2

Table 6.4: Integrated efficiencies over whole momentum range(DRT): averaged values in the momentum range of $0-30$GeV/c.

To make further analysis of this data, it it necessary to consider the momentum dependence of the efficiency. Fig.(6.4) shows the momentum dependence of the efficiencies for pion, kaon and proton.

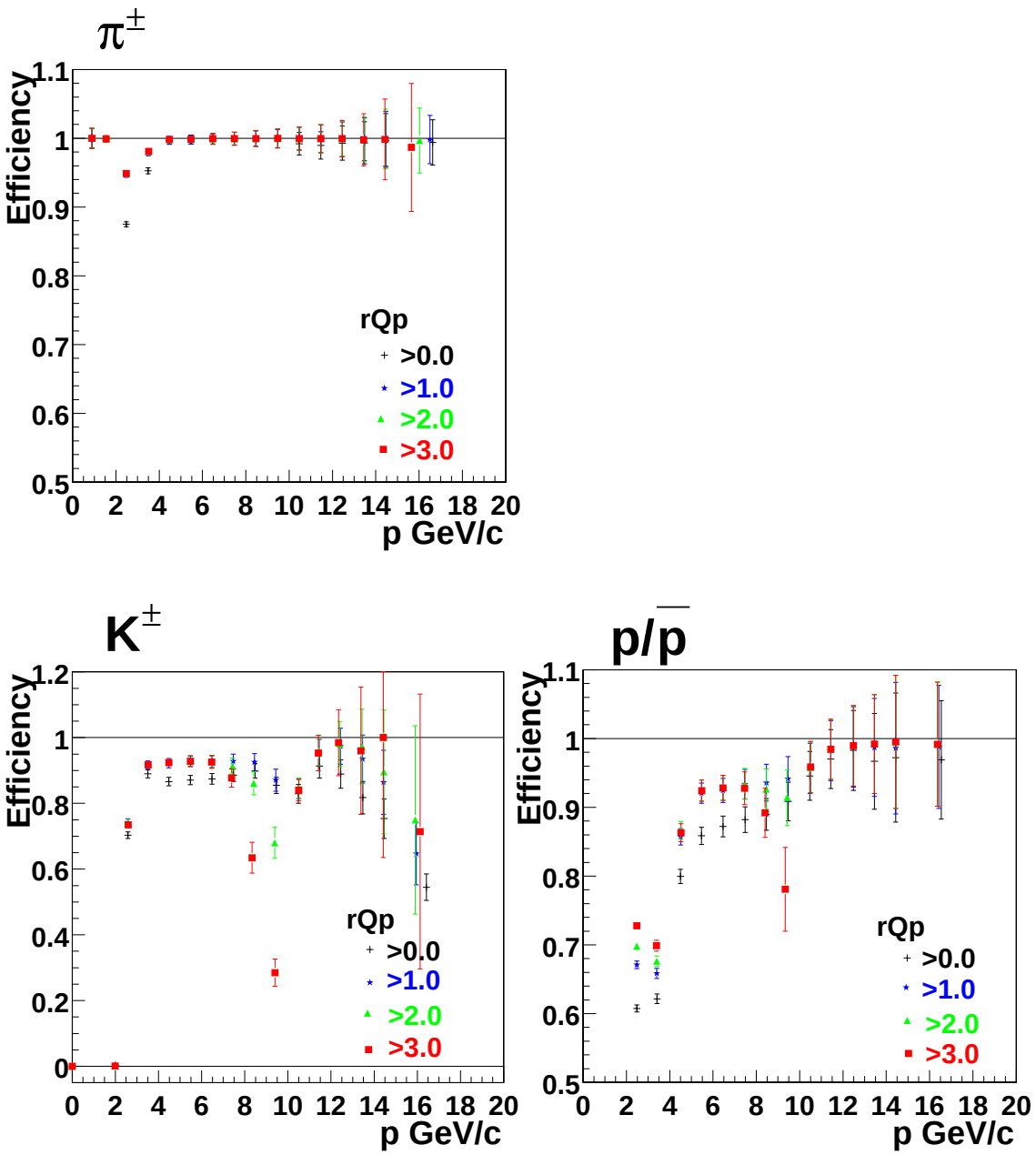

Figure 6.4: The momentum distributions of efficiencies of π, K and p for cuts on the quality parameter, $Qp > 0.0, 1.0, 2.0, 3.0$.

The efficiencies have dips in the Čerenkov thresholds at $p = 2.7$ GeV/c for pions and $p = 9.4$ GeV/c for kaons and protons as shown in Fig.(6.4). The dips increase as the quality parameter increases. The reason will be discussed in Chap.7.

Number of Tracks per a Detector Half

Number of tracks per a detector half should affect the identification performance because photons from the other ring become backgrounds.

Fig.(E.1),Fig.(E.2), and Fig.(E.3) in AppendixE show the efficiencies of π, K and p for the various number of tracks per a detector half;1,2, and > 2 respectively. They are the results from the IRT and DRT likelihood technique.

The results show that the both IRT and DRT efficiencies of pion are larger than 98% in the momentum range of $p > 3$ GeV/c for each cut of $N_{trk} = 1, 2, > 2$. As seen from the plots of kaon and proton, the efficiencies decrease as the number of tracks increases, $N_{trk} = 1, 2, > 2$. The reason is, as expected, that a Čerenkov ring is affected by photons of other rings as backgrounds.

To compare the results of the IRT and DRT methods, the numerical values of the efficiencies are listed in Tab.(6.5). The results indicate that the efficiencies of π, K and p decrease with the number of tracks per a detector half; $N_{trk} = 1, 2, > 2$. It should be stressed that the efficiencies in the lower momentum region are affected most because the numerical values are averaged over the whole momentum range and the number of produced hadrons shows the exponential fall with the momentum as shown in Fig.(3.24).

N_{trk}	$= 1$		$= 2$		> 2	
	IRT	DRT	IRT	DRT	IRT	DRT
ϵ_π	97.83±0.03	99.16±0.02	94.65±0.05	98.72±0.02	93.1±0.1	98.65±0.05
ϵ_K	88.6±0.2	87.6±0.2	73.8±0.3	72.1±0.3	65.0±0.7	63.1±0.7
ϵ_p	83.7±0.2	81.4±0.2	51.9±0.2	44.2±0.2	38.4±0.5	28.7±0.4

N_{trk}	*all*	
	IRT	DRT
ϵ_π	96.24±0.03	98.95±0.01
ϵ_K	81.8±0.1	80.4±0.2
ϵ_p	67.6±0.1	62.3±0.1

Table 6.5: The integrated efficiencies; $N_{trk} = 1, 2, > 2, all$, IRT and DRT, $Qp > 0.0$.

6.4 Purity from MC

The Q-matrix is not an inverse of the P-matrix. To calculate the Q-matrix, we need to return to the N-matrix. All elements in the N-matrix, N_t^i are determined using the MC results because each track is tagged with the true particle type t and the identified particle type i. The element of the Q-matrix, Q_t^i is written as defined in Eq.(6.6):

$$Q_t^i = \frac{N_t^i}{\sum_s N_s^i} \tag{6.29}$$

and it is normalized to 1 as $\sum_t Q_t^i = 1$.

It is necessary to determine the Q-matrix to correct the counts of hadrons and obtain the asymmetries of hadron productions. From Eq.(6.9), the Q- and P-matrix are connected via the hadron flux factors ϕ. The flux factors analyzed by MC rely on the simulation such as the event generator and the model of hadron fragmentation.

We will check the Q-matrix with a cut of the quality parameter and the multiplicity for each identification algorithm; IRT and DRT, and describe the results below.

The Purity using the IRT Technique

The MC data used is the same as those used in the analysis of the efficiencies.

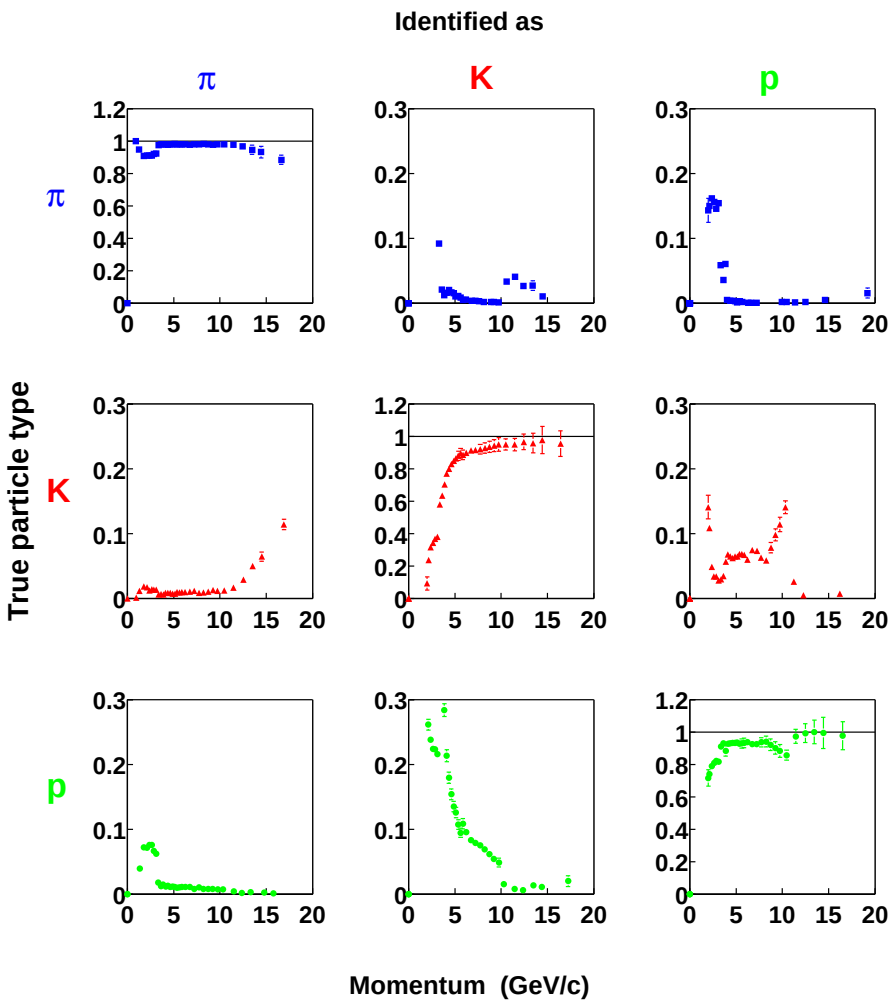

Figure 6.5: The Q-matrix elements which show purities and contaminations; IRT,$Qp > 0.0$.

The Purity using the DRT Technique

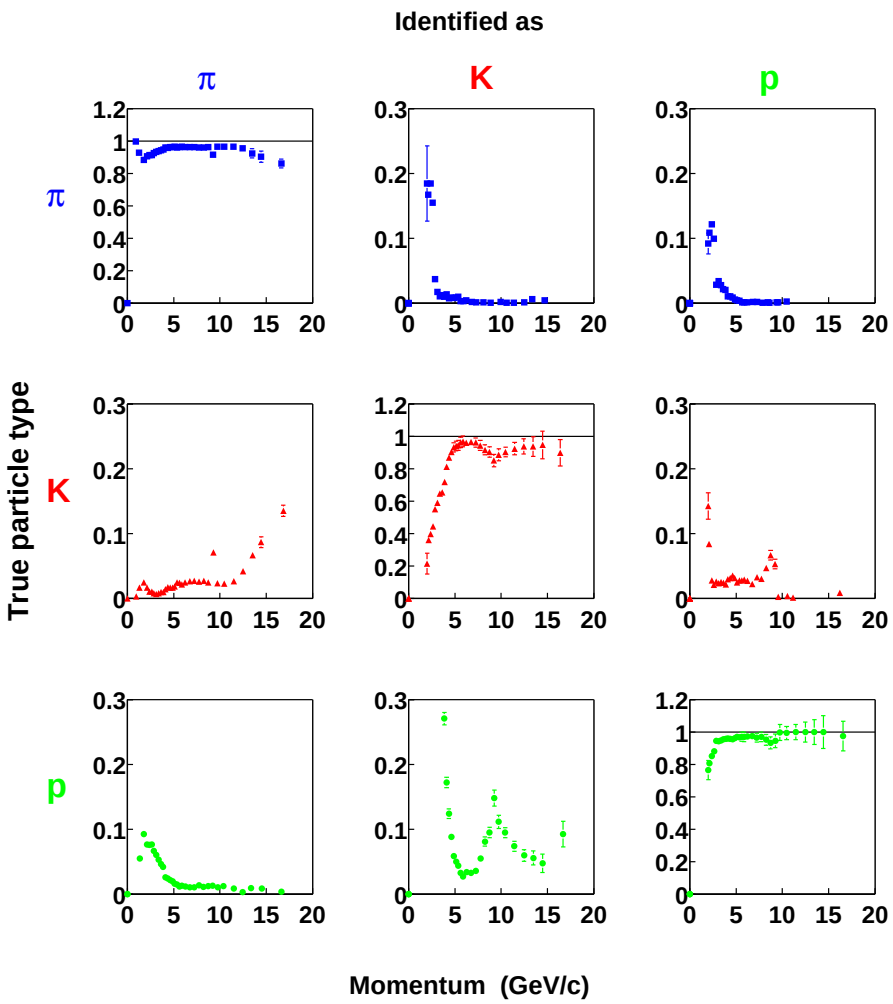

Figure 6.6: The Q-matrix elements which show purities and contaminations; DRT,$Qp > 0.0$.

6.5 Comparison of MC and Experimental Results

The results of MC are affected by the effects of the event generator and the model of hadron fragmentations. It is therefore important to compare the results of the MC with experimental data.

6.5.1 PID Efficiency from Decaying Particle Analysis

From Eq.(6.9), the P- and Q-matrix are connected via the hadron flux factors ϕ. One advantage of the experimental data is that the real flux factors can be taken into account. This chapter describes analysis of the experimental data with both

polarized and unpolarized gas target. To check all the elements of the P-matrix, the following decays are selected:

$$\begin{aligned}
\rho &\to \pi^+ + \pi^- \\
\phi &\to \mathrm{K}^+ + \mathrm{K}^- \\
\Lambda &\to \mathrm{p}^+ + \pi^- \\
\mathrm{K}^0_s &\to \pi^+ + \pi^-
\end{aligned}$$

The invariant mass peak is formed by two hadrons of a specific type. Fig.(6.7) shows the reconstructed ϕ invariant mass [21]. The mass is reconstructed with an assumption that the both hadrons have a kaon mass. These mass distributions are made under the condition that one of the detected two hadrons is identified with the RICH as a kaon. This condition allows us to evaluate the elements of N-matrix. The number of counts of the hadron identified as a kaon is denoted as $n(K, K)$. On the other hand, if the hadron is misidentified as a pion(proton), we obtain the counts of $n(\pi, K)(n(p, K))$. The total number of ϕ decaying into kaons is given by the integral of the mass peak, which is $n(h, K)$.

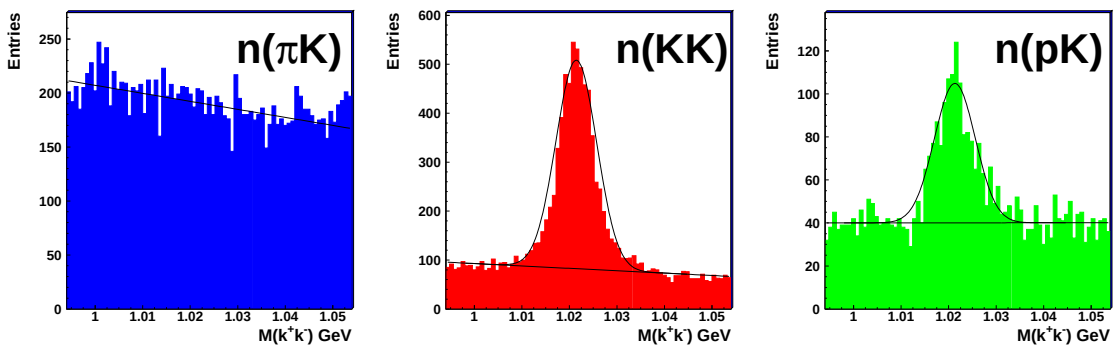

Figure 6.7: The reconstructed invariant mass distributions of ϕ with a kaon mass assumption. The one track is identified as K with the RICH, and the other track as π(or K,p).

The elements of the P-matrix can be determined as:

$$\begin{aligned}
P^{\pi}_{K} &= n(\pi, K)/n(h, K) \\
P^{K}_{K} &= n(K, K)/n(h, K) \\
P^{p}_{K} &= n(p, K)/n(h, K)
\end{aligned} \tag{6.30}$$

The accuracy of this method depends on the precision with which the integrals of the peaks are determined.

6.5.2 Comparison of DIS MC and Decaying Particle Analysis for Efficiency

The experimental results of the efficiency, momentum distributions of the P-matrix for the number of tracks per a detector half; $N_{trk} = 1, 2, > 2$ are shown in

Appendix G. Because of low statistics in the decaying particles, the results with $N_{trk} = 2$ are investigated, as shown in Fig.(6.8) [22].

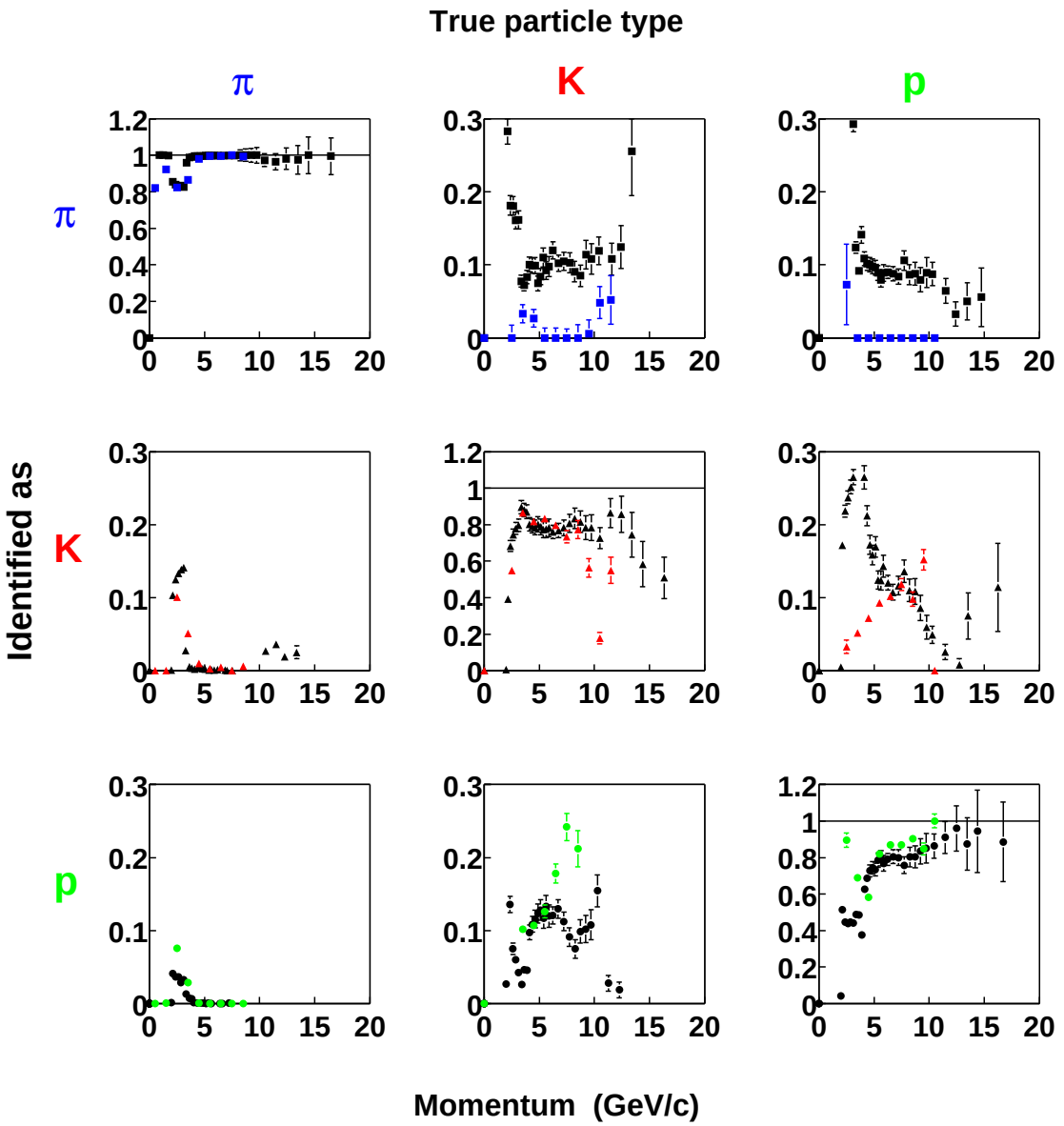

Figure 6.8: The momentum distributions of the P-matrix (the number of track per a detector half is 2.); the colored points denote results of the experimental data, and those of MC are superimposed as the black points.

The results are analyzed with the IRT method and a cut on the quality parameter is $Qp > 0.0$. The MC results with the IRT method and the same cut on the quality parameter are superimposed.

In general, hadrons from decaying particles have low momenta. The momentum of hadrons from decaying particles ranges from 0 to 12 GeV/c. The efficiencies are analyzed in the momentum range below 12 GeV/c and the momentum width of 1 GeV/c.

The results show that the efficiency of pion is more than 99% in the momentum range from 5 to 10 GeV/c. The efficiency of kaon increases as the momentum increases from 40% at 2 GeV/c to 85% at 8 GeV/c. Because of the low statistics at 9 GeV/c, the error on the efficiency of kaon is large at high momentum. The efficiency of proton increases as the momentum increases. The maximum value is 97%.

At the column of the true pions in Fig.(6.8), the misidentification probabilities of P_π^K and P_π^p are consistent between MC and experimental results. Misidentification probabilities are typically less than 0.01, with the peak value of up to 0.1.

The efficiency of kaon shows a good agreement below the momentum of 10 GeV/c, but a dip is visible at 10 GeV/c which is the Čerenkov threshold of kaon for the C_4F_{10} gas. Misidentification probabilities of kaon do not agree with the MC data. As for the column of proton, compared MC and experimental results, the efficiencies agree with each other. The misidentification probabilities have significant differences.

The result, Fig.(6.8) shows that the efficiencies of π, K and p agree well. However, the off-diagonal elements have differences between MC and experimental data. The possible reason will be discussed in the following section.

Chapter 7

Interpretation of the Results

Fig.(6.8) shows the main result of this work. This result suggests interpretations as below:

- The efficiencies have dips around the Čerenkov thresholds. The dips increase as the quality parameter increases.
- The efficiencies of MC and experimental results are consistent in the measured range of momentum. However, the off-diagonal elements of the P-matrix have a significant difference between MC and experimental results.

7.1 Dips at the Čerenkov Thresholds

The efficiencies, the diagonal elements of the P-matrix, have dips at the Čerenkov thresholds of $p = 2.7$ GeV/c for pions and $p = 9.4$ GeV/c for kaons. As show in Fig.(6.4), the dips increase as the quality parameter increases. Contrary to our prediction, it means that the efficiencies are not going up as the quality parameter increases.

To explain this result, I must refer to the IRT likelihood technique as described in Chap.4. The likelihood is defined as (Eq.(4.24)):

$$L(\langle\theta\rangle) = \exp\left\{-\frac{(\langle\theta\rangle - \theta_{th})^2}{2\sigma^2_{\langle\theta\rangle}}\right\}$$

for each radiator. The averaged angle resolution $\sigma_{\langle\theta\rangle}$ is expressed as $\sigma_{\langle\theta\rangle} = \sigma_\theta/\sqrt{N_{PMT} - 1}$. In case of the particle with the momentum below the threshold, we cannot evaluate the above equation because no Čerenkov information can be obtained. We set a fixed value as the sub-threshold likelihood. Then we obtain the combined likelihood from aerogel and gas for a particle with its momentum below the threshold as:

$$L = L(\langle\theta\rangle) \cdot L_{s.thre.}$$

Before calculating the quality parameter, we take the decadic logarithm of the combined likelihood as:

$$\log_{10} L = \log_{10} L_{s.thre.} - \frac{\log_{10} e}{2\sigma_\gamma^2} \cdot (\langle\theta\rangle - \theta_{th})^2 \cdot |N_{PMT} - 1| \qquad (7.1)$$

At the C_4F_{10} gas threshold for kaons($p_{thre.}[K] = 9.4$ GeV/c), the efficiency of kaons is reduced gradually as the momentum approaches the threshold. This gentle distribution is caused by the fact that the likelihood has a smooth function of $\langle\theta\rangle - \theta_{th}$ of aerogel as a term in Eq.(7.1). On the other hand, just above the threshold, the efficiency goes up suddenly to 85%. It is necessary to consider that each likelihood is calculated as a Gaussian shape of the averaged angle distribution as:

$$L \;=\; L^{gas}(\langle\theta\rangle)) \cdot L^{aerogel}(\langle\theta\rangle) \qquad (7.2)$$

This equation in general gives the larger value than that of Eq.(7.1). That is why the efficiency goes up suddenly after the threshold. At the gas threshold for pions($p_{thre.}[\pi] = 2.7$ GeV/c), the dip of the pion efficiency is visible as the same reason.

It is necessary to optimize the fixed value of L_{min} and $L_{s.thre.}$ in order to obtain the efficiencies more properly.

7.2 Disagreement between MC and Decaying Particle Analysis

As described in Eq.(6.3), the P-matrix is independent of the flux factors. It means that the DIS MC and the decaying particle analysis should be in agreement on the elements of the P-matrix.

Disagreements between MC and experimental results may be caused by the event topology. For example, $\phi \to$ KK decay provides kaon samples to evaluate the K-column of the P-matrix.

The momentum of the kaons is mostly low and the opening angle is large. Hence, the results of the MC and decaying particle analysis have agreement at the low momentum region which is about $p < 5.0$ GeV/c. On the contrary, at the higher momentum region the opening angle is getting smaller and it causes the overlapping Čerenkov rings. Since the overlapping ring affects as backgrounds to the other tracks, the performance of the particle identification should be influenced. The results of K-column in Fig.(6.8) show that the efficiency decreases at the high momentum region $p > 5$ GeV/c, and correspondingly the misidentification of proton increases.

7.3 Relation of the P- and Q-matrix via the Flux Factor

From Eq.(6.9), the Q-matrix is connected simply via the P-matrix and the flux factor ϕ. Since the P-matrix is independent of the flux factor, the flux factor affects only the Q-matrix.

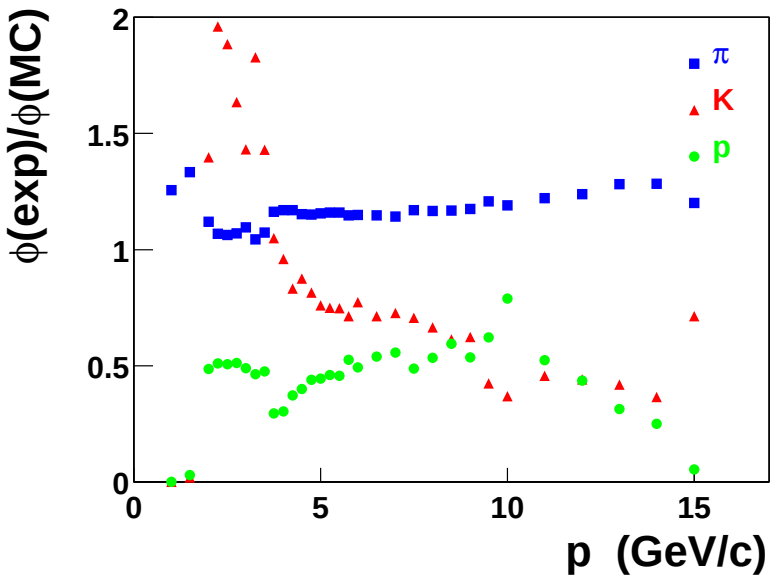

Figure 7.1: The momentum distributions of the flux ratio. Points denote the ratio of the experimental and MC flux factors $\phi(exp)/\phi(MC)$ for each particle: π, K and p.

Fig.(7.1) shows the momentum distributions of the ratio of the experimental and MC flux factors $\phi(exp)/\phi(MC)$ for each particle: π, K and p. They should be 1, but the results show the difference between the MC and experimental data. The overall ratios for K and p are about 1.5 and 0.5 respectively.

In order to check the effects of the flux factors, the method described below is considered. A P-matrix is made as an example:

$$P = \begin{pmatrix} 0.9759_{\pm 0.0003} & 0.019_{\pm 0.001} & 0.183_{\pm 0.001} \\ 0.0019_{\pm 0.0002} & 0.927_{\pm 0.002} & 0.080_{\pm 0.001} \\ 0.0012_{\pm 0.0002} & 0.079_{\pm 0.001} & 0.863_{\pm 0.002} \end{pmatrix} \tag{7.3}$$

This is the P-matrix of the result from IRT method, with a cut of $Qp > 0.0$. The Q-matrix of the data is written as:

$$Q = \begin{pmatrix} 0.9756 & 0.012 & 0.047 \\ 0.007 & 0.899 & 0.041 \\ 0.018 & 0.089 & 0.912 \end{pmatrix} \tag{7.4}$$

The statistical errors are ignored.

New flux factors are chosen to agree the flux factors with the MC and the experimental data. From Fig.(7.1), the averaged correction factors are 1.5 for kaons and 0.75 for protons as the flux factor of pions to be normalized to 1. The Q-matrix becomes:

$$Q = \begin{pmatrix} 0.9712 & 0.020 & 0.04 \\ 0.009 & 0.965 & 0.09 \\ 0.012 & 0.013 & 0.847 \end{pmatrix} \tag{7.5}$$

The purity of kaon has a difference with about 7%, and that of proton with about 5%. This result indicates that the flux factor is playing a role in the calculation of the Q-matrix.

7.4 Advantage of the Q-matrix

From Eq.(6.20) and Eq.(6.21), the Q-matrix has the same behavior as the inverse of the P-matrix.

The advantage of using the Q-matrix is that we can take into account the not-identified particle "X" as $\vec{I} = (I_\pi, I_K, I_p, I_X)$. In this case, the P-matrix becomes a 4×3 matrix. In general, the inverse of the 4×3 matrix cannot be calculated. However, detected hadrons can be unfolded using the 4×3 Q-matrix.

A point to which special attention should be paid is to use the not-identified particle X. We choose a cut on the quality parameter as $Qp > 0.0$ to suppress the X particles because the MC simulation does not realize the experimental data perfectly. It is necessary to tune the parameters of the MC to adjust the hadron momentum spectra.

I will consider the error propagation in the inverse of the P-matrix and the Q-matrix. Let us take an artificial example of the P-matrix as:

$$P + \delta P = \begin{pmatrix} 1 - a_1 - b_1 + \delta & a_2 - \frac{\delta}{2} & a_3 - \frac{\delta}{2} \\ a_1 - \frac{\delta}{2} & 1 - a_2 - b_2 + \delta & b_3 - \frac{\delta}{2} \\ b_1 - \frac{\delta}{2} & b_2 - \frac{\delta}{2} & 1 - a_3 - b_3 + \delta \end{pmatrix} \tag{7.6}$$

a_i and b_i (i=1,2,3) are the off-diagonal elements of the P-matrix, and $1 - a_i - b_i$ are the diagonal elements. δ is a small value which is independent of a_i and b_i. δ, a_i and b_i are small enough compared to 1.

The propagation of the errors of the inverse of $P + \delta P$ is checked using this δ. One of the diagonal elements of the inverse of the P-matrix can be written as:

$$(P + \delta P)^{-1}_{11} = \frac{1 - (a_2 + b_2 + a_3 + b_3) - \delta + O(a_i^2, b_i^2)}{1 - (a_1 + b_1 + a_2 + b_2 + a_3 + b_3) - \frac{3}{2}\delta + O(a_i^2, b_i^2)} \tag{7.7}$$

The value of the error δ does not affect results much. Because the denominator and the numerator have 1 in their terms, δ does not affect the values. On the contrary, an off-diagonal element of the inverse of the P-matrix is written as:

$$(P + \delta P)^{-1}_{21} = \frac{-(1 - a_2 - b_2 + \delta)(a_3 - \frac{\delta}{2}) + O(a_2 b_b)}{1 - (a_1 + b_1 + a_2 + b_2 + a_3 + b_3) - \frac{3}{2}\delta + O(a_i^2, b_i^2)} \tag{7.8}$$

The numerator contains $(a_3 - \frac{\delta}{2})$. In case that δ is close to the value of a_3, the change of the element $(P + \delta P)^{-1}_{21}$ becomes larger compared to the value of a_3.

As for the Q-matrix, it is derived from the elements of the P-matrix as Eq.(6.9). One of the elements of the Q-matrix is written as:

$$Q^{\pi}_{\pi} = \frac{P^{\pi}_{\pi}\phi_{\pi}}{\sum_{t=\pi,K,p} P^{\pi}_{t}\phi_{t}} \tag{7.9}$$

Let us replace the elements of the P-matrix with a_i and b_i. The value of $Q^{\pi}_{\pi} = Q_{11}$ is explicitly written as:

$$Q_{11} = \frac{(1 - (a_1 + b_1) - \delta)\phi_{\pi}}{(1 - (a_1 + b_1) - \delta)\phi_{\pi} + (a_2 - \frac{\delta}{2})\phi_K + (a_3 - \frac{\delta}{2})\phi_p} \tag{7.10}$$

The error becomes δ. An off-diagonal element of the Q-matrix is derived in the same way as:

$$Q_{21} = \frac{(a_1 - \frac{\delta}{2})\phi_{\pi}}{(a_1 - \frac{\delta}{2})\phi_{\pi} + (1 - (a_2 + b_2) - \delta)\phi_K + (a_3 - \frac{\delta}{2})\phi_p} \tag{7.11}$$

The numerator contains $(a_1 - \frac{\delta}{2})$. In case that δ is close to the value of a_1, the change of the element Q_{21} becomes larger compared to the value of a_1. The Q-matrix and the inverse of the P-matrix have the same behavior from the point of view of the error propagation.

Chapter 8

Summary

The Ring Imaging Čerenkov Counter (RICH) of HERMES is designed to identify the hadrons in the momentum range of 2-15 GeV/c. It has been constructed and operating routinely as part of the HERMES experiment since May 1998.

The HERMES RICH is a dual radiator RICH. The radiators are the C_4F_{10} gas and the silica aerogel. The refractive indices are $n_{\rm gas} = 1.00137$ and $n_{\rm aerogel} = 1.0303$ respectively. These indices are suitable to identify hadrons in the momentum range of HERMES ($2 < p < 15$GeV/c). The RICH with aerogel is used for the first time in an actual experiment.

The refractive indices of the aerogel tiles are measured using an optical method with a He-Ne laser beam of $\lambda = 632.8$ nm. The averaged refractive index is $n_{\rm aerogel} = 1.0303$ and its standard deviation is 2.5×10^{-4}. These values satisfy the requirement of the refractive index. The averaged size of the aerogel is $11 \times 11 \times 1.1{\rm cm}^3$, and its deviation is ± 0.4mm.

This precision allows us to determine the Čerenkov angle from the information of positions of fired PMTs. Another factors influencing the precision of the Čerenkov angle are: uncertainty of the focal points of the mirrors, refraction of the Čerenkov photons at the boundary between the aerogel and the C_4F_{10} gas, and Rayleigh scattering in the aerogel. These factors are corrected for by software to improve the precision of calculating the Čerenkov angle. On the other hand, the number of fired PMTs is also a criterion of the RICH performance because it is affected by the reflectivity of the mirror and the efficiency of the photon detector. After the analysis of the mirror reflectivity, the number of fired PMTs from the MC data has a good agreement with the experimental result; $N_{PMT}^{aerogel} = 11$ and $N_{PMT}^{gas} = 13$. The values of θ and N_{PMT} from the experiment have achieved the design values and are close to the MC predictions.

The Čerenkov angle and the number of fired PMTs are taken into account to perform the particle identification. In the practical particle identification method, particles are identified with the likelihood technique which combines the information of the aerogel and the C_4F_{10} gas to give equal treatments of the radiators. A likelihood L_h for each of the hypothesis $h = \pi, {\rm K}, {\rm p}$ is calculated based on the number of fired PMTs N_{PMT} and the measured Čerenkov angle θ.

PID performance of the RICH is studied from the point of view of the efficiency

and purity. The number of identified hadrons $\vec{I} = (I_\pi, I_\mathrm{K}, I_\mathrm{p})$ and true hadrons $\vec{N} = (N_\pi, N_\mathrm{K}, N_\mathrm{p})$ are related by matrices. They are expressed as P- and Q-matrix. The efficiencies (purities) are the diagonal elements of the P-(Q-) matrix.

The following factors influencing the efficiencies are taken into account: (1) The quality parameter is the decadic logarithm of the ratio of the highest and the second highest likelihoods, $Qp = \log_{10} \frac{L_1}{L_2}$. A cut on the quality parameter affects the performance of the particle identification. (2) The events are classified according to the number of tracks $= 1, = 2, > 2$ per a detector half. When more than one tracks enter the RICH, photons from other tracks will become backgrounds.

The results of the overall efficiencies under the conditions described above suggest that the $Qp > 1.0$ is a suitable cut for kaons. The efficiencies for each particle are $\epsilon_\pi = 98\%$ and $\epsilon_K = 93\%$, which are consistent with the results of the study of the decaying particles ($\phi \to K^+K^-$, $\rho \to \pi^+\pi^-$, $\Lambda \to p\pi^-$, etc.).

From the MC results, the P-matrix in the range of $2 - 15$ GeV/c is obtained. The efficiencies (the diagonal elements of the P-matrix) of MC and experimental results are consistent in the measured range of momentum. The following points are to be further studied in future. The off-diagonal elements of the P-matrix still have a difference between MC and experimental results. The efficiencies have dips around the Čerenkov thresholds.

The data of kaons identified with the RICH have been accumulated and analyzed to study the asymmetries of the kaon productions. It allows us to measure the parton distribution functions of the strange quarks, and the flavor asymmetry of the polarized sea quarks. The HERMES RICH is a major breakthrough in the study of the spin structure of the nucleon.

Acknowledgement

I would like to thank Prof. T.-A. Shibata, my thesis supervisor. I wish to thank him for providing me with the opportunity to study the HERMES RICH. I also would like to express my appreciation to the continuing guidance and encouragement of Dr. Y. Sakemi. The several helpful discussions with him are gratefully acknowledged.

Many people have contributed to the design and use of the HERMES RICH. I wish to thank J. Kanesaka, L.F. Zhang and F. Sato for their measurements of the aerogel properties, constructions of the RICH and development of the Monte Carlo. The Monte Carlo production is performed by S. Yoneyama. These data have been essential.

It is a pleasure to acknowledge the hospitality and encouragement of the members of the HERMES group. I would like to thank R. Kaiser for suggesting this study and for stimulating in it. Several helpful discussions with S. Bernreuther are gratefully acknowledged.

This thesis is a culmination of several years of work and would not have been possible without help from many people. I wish to thank them here.

Appendix A

Statistical Error of P- and Q-Matrix

The element of P-matrix P_t^i is a function of N_t^i and it is written as

$$P_t^i = \frac{N_t^i}{\sum_j N_t^j} \tag{A.1}$$

Deviation δP_t^i can be expressed with partial differential of P_t^i with N_t^i

$$\begin{aligned} \delta P_t^i &= \sum_k \frac{\partial P_t^i}{\partial N_t^k} \delta N_t^k \\ &= \sum_k \left\{ \frac{1}{\sum_{k'} N_t^{k'}} \delta(k,i) - \frac{N_t^k}{(\sum_{k'} N_t^{k'})^2} \right\} \delta N_t^k \end{aligned} \tag{A.2}$$

where $\delta(k,i)$ is a delta function(= 1 for $k = i$, = 0 for $k \neq i$). If a correlation between δN_t^i and $\delta N_t^k (k \neq i)$ is ignored, a square of the deviation δP_t^i is given as

$$\begin{aligned} (\delta P_t^i)^2 &= \left(\sum_k \{ \frac{1}{\sum_{k'} N_t^{k'}} \delta(k,i) - \frac{N_t^i}{(\sum_{k'} N_t^{k'})^2} \} \delta N_t^k \right)^2 \\ &= \left\{ (\frac{1}{\sum_{k'} N_t^{k'}})^2 - 2 \frac{1}{\sum_{k'} N_t^{k'}} \frac{N_t^i}{(\sum_{k'} N_t^{k'})^2} \right\} (\delta N_t^i)^2 + \frac{(N_t^i)^2}{(\sum_{k'} N_t^{k'})^4} \sum_k (\delta N_t^k)^2 \end{aligned} \tag{A.3}$$

If the elements of P-matrix N_t^i are represented as a Poisson distribution, the deviations δN_t^i are

$$\delta N_t^i = \sqrt{N_t^i} \tag{A.4}$$

hence,

$$\delta P_t^i = \sqrt{ \left\{ (\frac{1}{\sum_{k'} N_t^{k'}})^2 - 2 \frac{1}{\sum_{k'} N_t^{k'}} \frac{N_t^i}{(\sum_{k'} N_t^{k'})^2} \right\} \cdot N_t^i + \frac{(N_t^i)^2}{(\sum_{k'} N_t^{k'})^4} \sum_k N_t^k } \tag{A.5}$$

As for Q-matrix, the elements Q_t^i are functions of N_t^i. The deviations δQ_t^i can be calculated in the same way as described before.

$$\delta Q_t^i = \sqrt{ \left\{ (\frac{1}{\sum_{s'} N_{s'}^i})^2 - 2 \frac{1}{\sum_{s'} N_{s'}^i} \frac{N_t^i}{(\sum_{s'} N_{s'}^i)^2} \right\} \cdot N_t^i + \frac{(N_t^i)^2}{(\sum_{s'} N_{s'}^i)^4} \sum_s N_s^i } \tag{A.6}$$

Appendix B

Projected Performance of the RICH

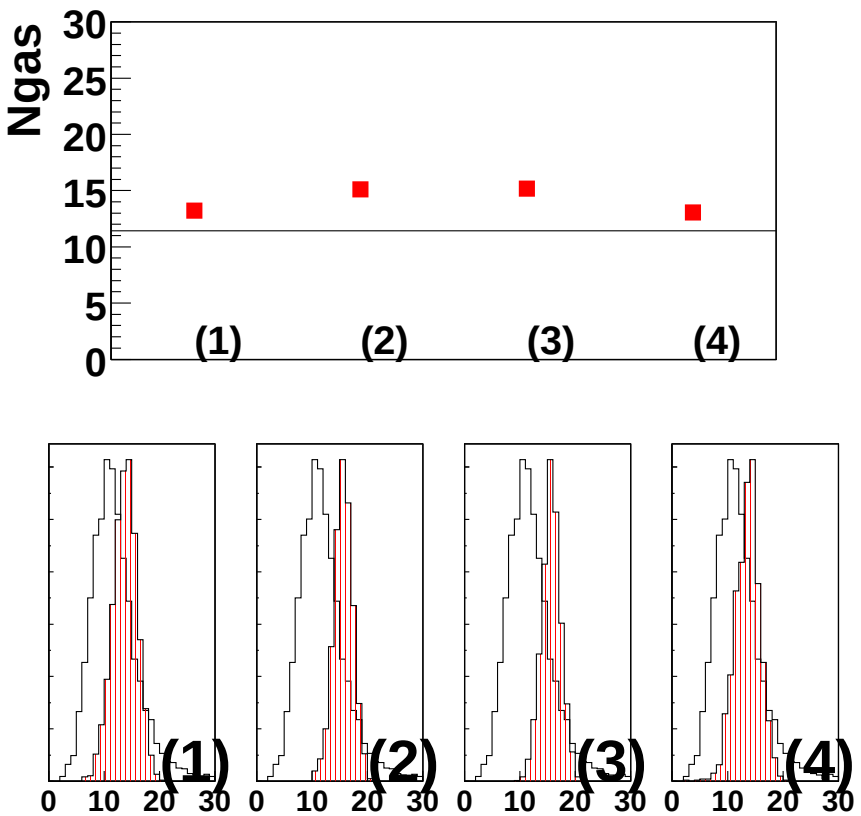

Figure B.1: The comparison N_{PMT}^{gas} with the various MC productions and the experimental results. The lower plots show the distributions of N_{PMT}^{gas}, the production (1),(2),(3) and (4) from the left. The MC results (denoted by shaded histograms) and the experimental results (normal histograms) are superimposed. The upper plot shows the averaged N_{PMT}^{gas}. The square points denote the MC results for each production and the horizontal line is the experimental results.

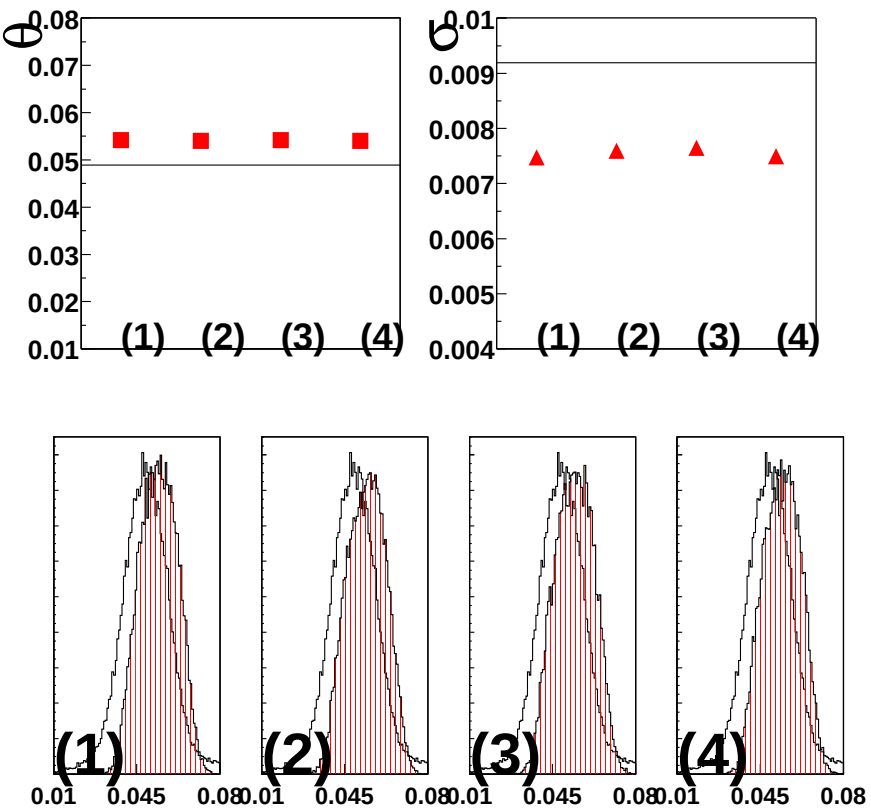

Figure B.2: The comparison θ^{gas} with the various MC productions and the experimental results. The lower plots show the distributions of θ^{gas}, the production (1),(2),(3) and (4) from the left. The MC results (denoted by shaded histograms) and the experimental results (normal histograms) are superimposed. The upper plot shows the averaged θ^{gas}. The square points denote the MC results for each production and the horizontal line is the experimental results.

Čerenkov Angle Distributions of the Latest MC Simulation

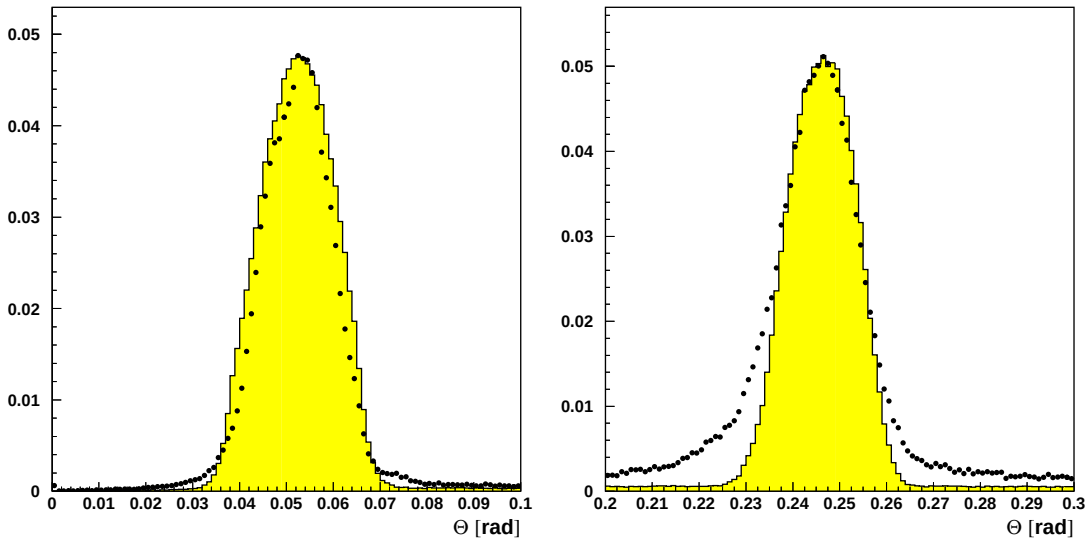

Figure B.3: Distributions of the Čerenkov angle from the latest MC simulation. The left plot shows the Čerenkov angle of the C_4F_{10} gas, the right of the aerogel for single electrons ($p > 5$ GeV/c). Histogram MC, points data. The averaged values of the distributions have a good agreement with each other. The wider tails of the experimental distributions are due to backgrounds.

Momentum Distributions of the Likelihood

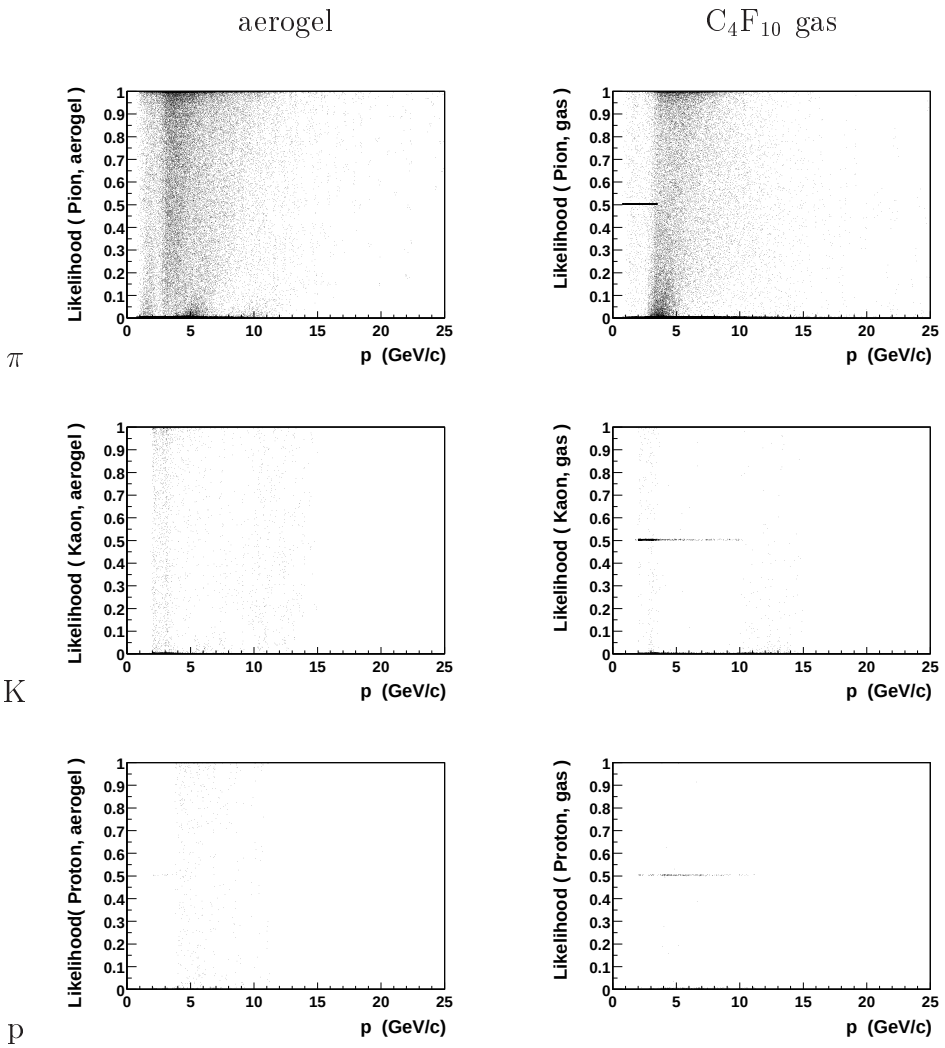

Figure B.4: Momentum distributions of the likelihood. The plots show the momentum distributions of the likelihood calculated for each particle hypothesis (π, K and p) and each radiator (aerogel and C_4F_{10}).

Appendix C

Momentum Distributions of the Statistics for the Two Binnings

The momentum binning is regarded as of importance for the correction to the hadron yields. To study a fine unfolding of the identified particles it is necessary to use small intervals of momenta. On the contrary, the statistics in a momentum bin becomes small and its statistical error grows up.

The momentum distribution of the hadrons shows the exponential fall (Fig.(3.24)). Clearly, there is large decrease in the number of hadrons when applying a constant interval binning, 1 bin per 1 GeV/c for example. The number of hadrons under the momentum binning, so called "binning 1" is listed in Tab.(C.1).

bin	0.0-1.0	1.0-2.0	2.0-3.0	3.0-4.0	4.0-5.0	5.0-6.0
number of hadrons	9811	114302	176900	132300	93073	66636
	6.0-7.0	7.0-8.0	8.0-9.0	9.0-10.0	10.0-11.0	11.0-12.0
	46695	32176	22222	15568	10609	7337
	12.0-13.0	13.0-14.0	14.0-15.0	15.0-30.0		
	4701	3098	1883	2614		

Table C.1: Momentum binning1: the interval is $1 GeV/c$.

bin	0.0-0.5	0.5-1.0	1.0-1.5	1.5-2.0	2.0-2.25	2.25-2.5
number of hadrons	0	10031	48172	67763	46341	45468
	2.5-2.75	2.75-3.0	3.0-3.25	3.25-3.5	3.5-3.75	3.75-4.0
	43813	41536	38448	34667	32121	27131
	4.0-4.25	4.25-4.5	4.5-4.75	4.75-5.0	5.0-5.25	5.25-5.5
	26196	24297	22369	20610	18932	17687
	5.5-5.75	5.75-6.0	6.0-6.5	6.5-7.0	7.0-7.5	7.5-8.0
	15634	14513	25396	21394	17527	14710
	8.0-8.5	8.5-9.0	9.0-9.5	9.5-10.0	10.0-11.0	11.0-12.0
	12153	10105	8562	7039	10609	7337
	12.0-13.0	13.0-14.0	14.0-15.0	15.0-30.0		
	4701	3098	1883	2614		

Table C.2: Momentum binning2: the interval is defined as the number of hadrons in each bin are same as possible.

To make full use of the high statistics at the lower momentum, the momentum binning is modified as shown in Tab.(C.3); "binning 2":

momentum	0.0	-	2.0	-	6.0	-	10.0	-	15.0	-	30.0
bins per 1GeV/c		2		4		2		1		all	
width (GeV/c)		1.0		0.25		0.5		1.0		15.0	

Table C.3: Definition of the momentum "binning 2".

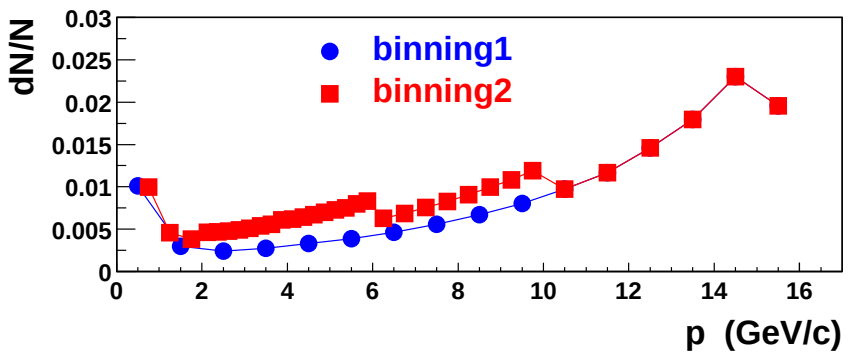

Figure C.1: Momentum distributions of the statistical errors for the two binnings.

Tab.(C.2) shows the statistics of hadrons in the bins.

Binning 1 Binning 2

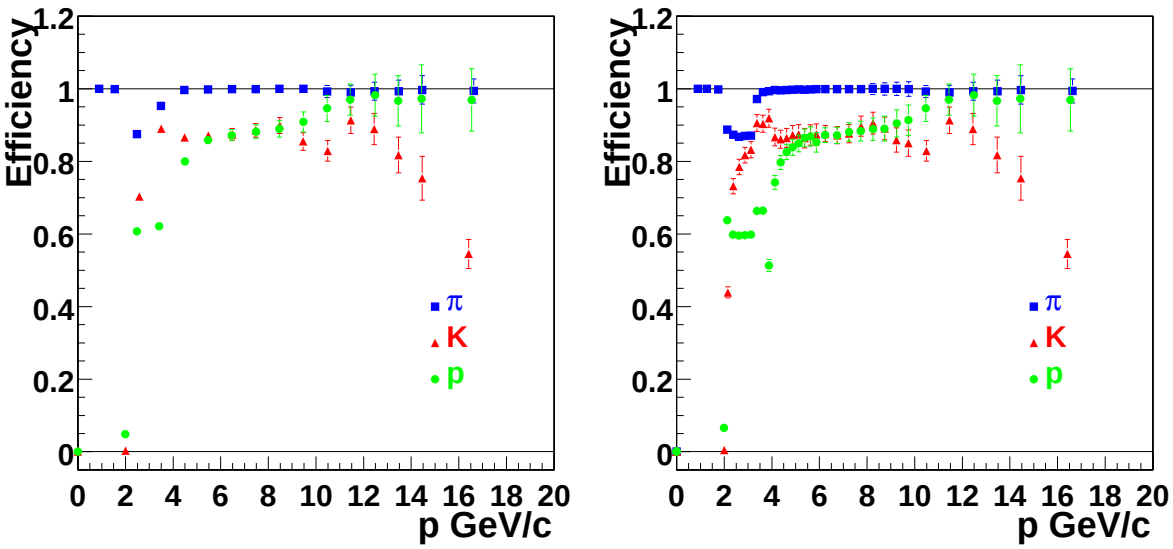

Figure C.2: Efficiencies of pion, kaon and proton with the two different binnings: The left plot shows the momentum binning 1. The definition of the binning is 1 bin per 1 GeV/c. The right plot shows the momentum binning 2. The definition of the binning is described in the text and Tab.(C.3).

Fig.(C.2) shows the efficiencies of pion, kaon and proton with the momentum binning 1 and 2, respectively. Both are the results of the IRT identification method and a cut on the quality parameter is $Qp > 0.0$. We have applied "momentum binning 2" to studies of the efficiencies in the following section.

Appendix D

Difference Between Positive and Negative Charged Particles

Difference between positive and negative charged particles should not affect the particle identification because the RICH and other spectrometers are located symmetrically with the y-axis of the HERMES coordinate system.

Positive hadrons Negative hadrons

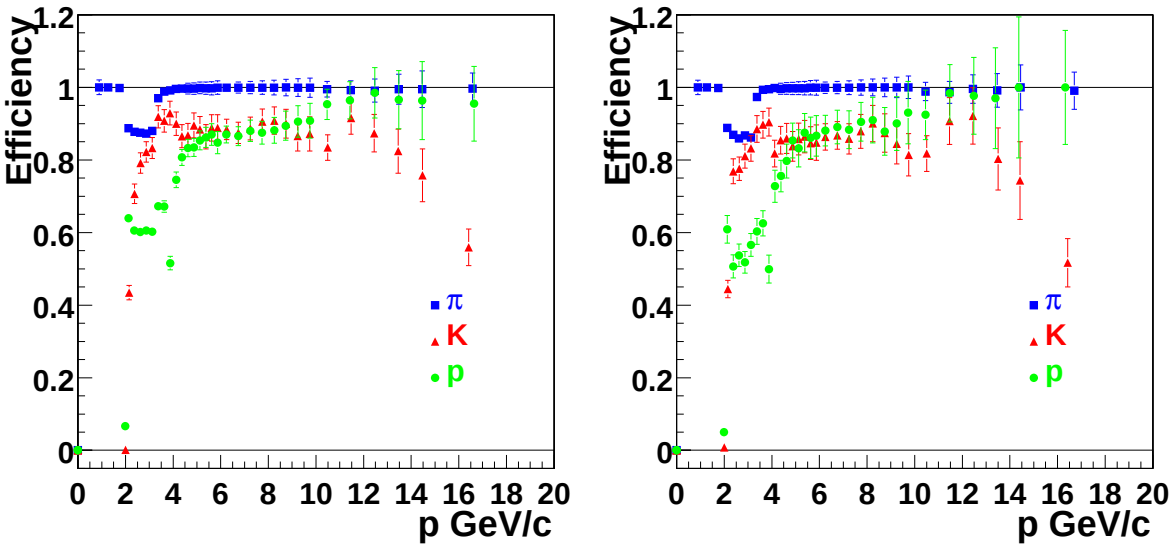

Figure D.1: Efficiencies of pion, kaon and proton for the positive charged hadrons(the left plots) and the negative charge hadrons (the right plots).

Fig.(D.1) shows the efficiencies of the positive and negative charged hadrons respectively. The yield of produced negative hadrons is smaller than that of positive hadrons, and the statistical errors in negative charged hadrons are larger.

However, compared the results of the efficiencies agree well with each other within the statistical errors.

This result indicates that it it sufficient to use both negative and positive hadrons altogether to study the efficiency.

Appendix E

Momentum Distributions of the Efficiencies

Comparison of the Efficiencies for the Two Likelihood Technique; IRT and DRT ($N_{trk} = 1, 2, > 2$)

IRT ($N_{trk} = 1$) DRT ($N_{trk} = 1$)

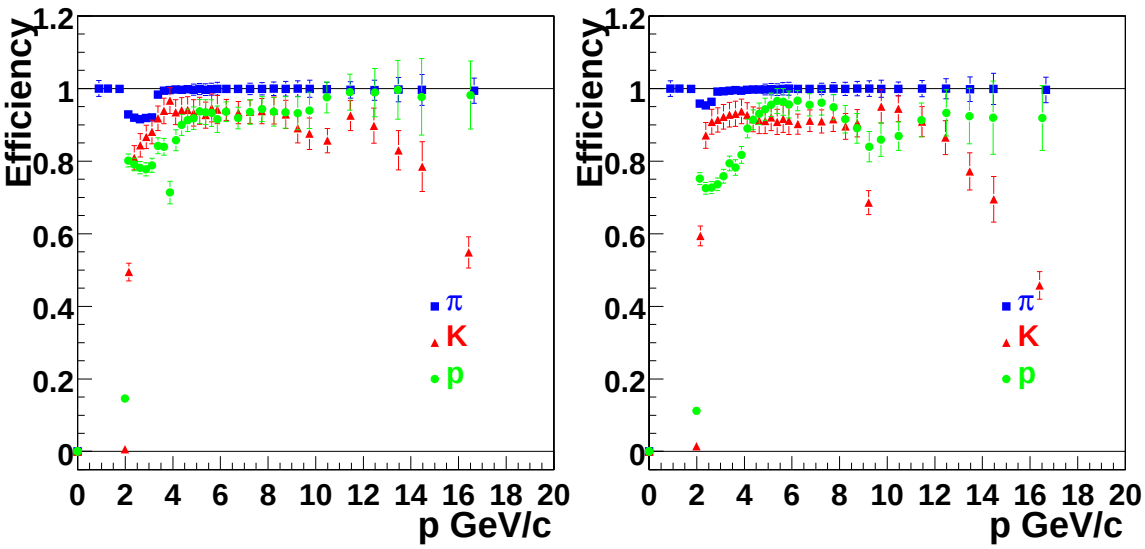

Figure E.1: Efficiencies of pion, kaon and proton; the number of tracks per a detector half is 1 ($Qp > 0.0$). The left plot shows the results for IRT, and the right plot for DRT.

IRT ($N_{trk} = 2$) DRT ($N_{trk} = 2$)

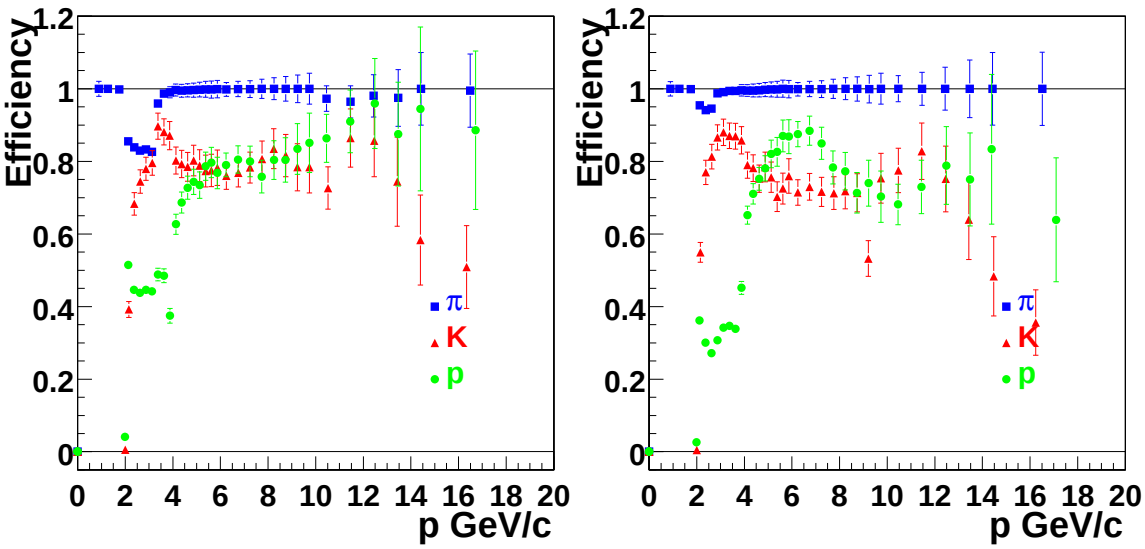

Figure E.2: Efficiencies of pion, kaon and proton; the number of tracks per a detector half is 2 ($Qp > 0.0$). The left plot shows the results for IRT, and the right plot for DRT.

IRT ($N_{trk} > 2$) DRT ($N_{trk} > 2$)

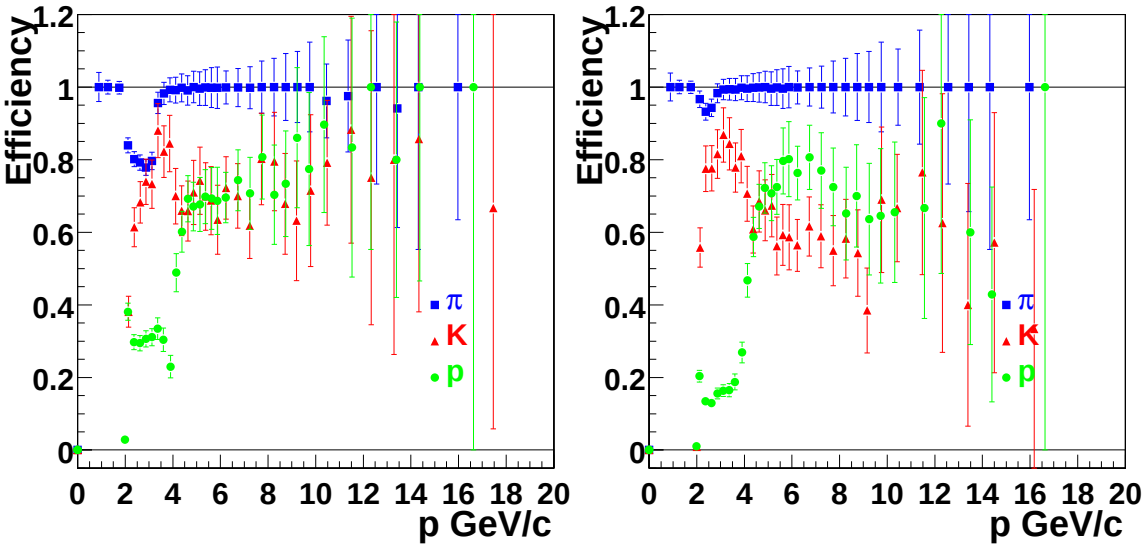

Figure E.3: Efficiencies of pion, kaon and proton; the number of tracks per a detector half is 2 ($Qp > 0.0$). The left plot shows the results for IRT, and the right plot for DRT.

Appendix F

Momentum Distributions of the Q-matrix

The Q-matrices Analyzed with the IRT Method ($N_{trk} = 1, 2, > 2$)

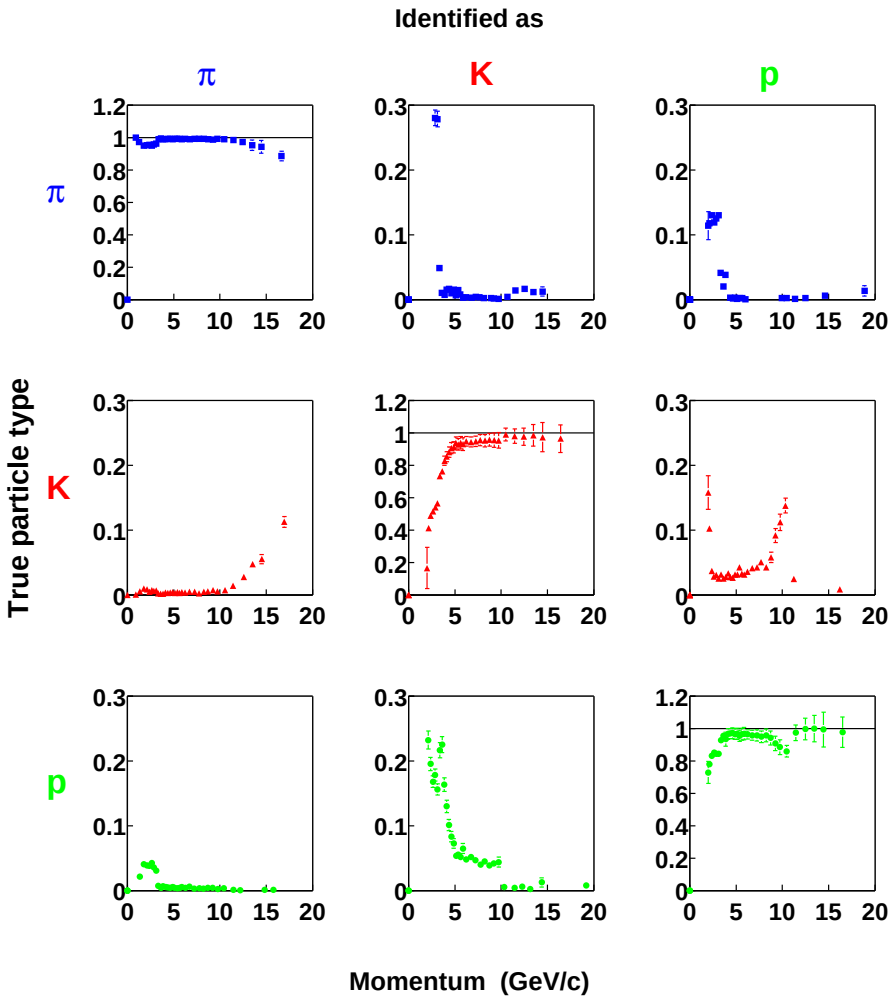

Figure F.1: Purities and contaminations; $Qp > 0.0$,$N_{trk} = 1$

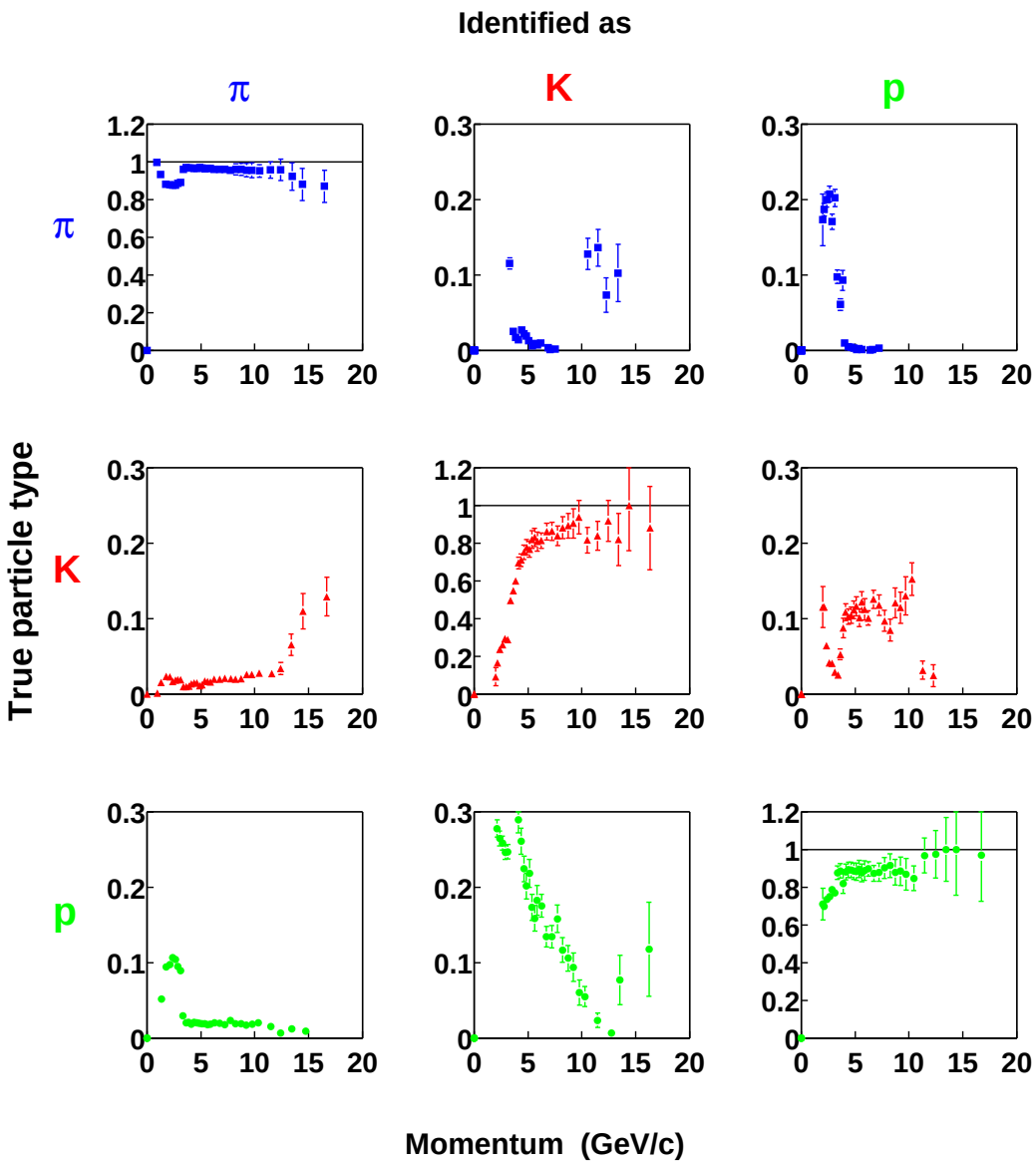

Figure F.2: Purities and contaminations; $Qp > 0.0$,$N_{trk} = 2$

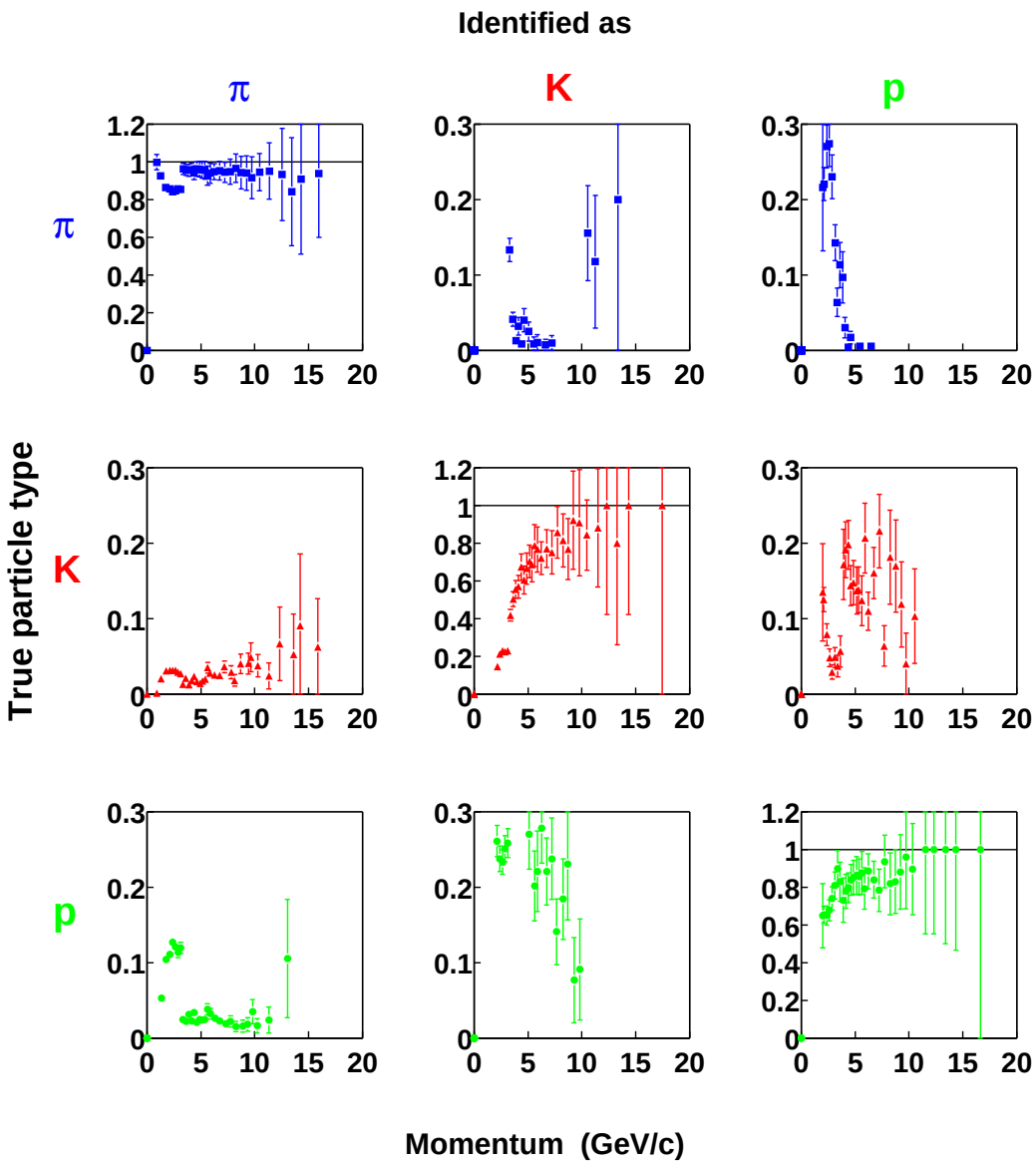

Figure F.3: Purities and contaminations; $Qp > 0.0$,$N_{trk} > 2$

Appendix G

Comparison DIS MC and Decaying Particle Analysis

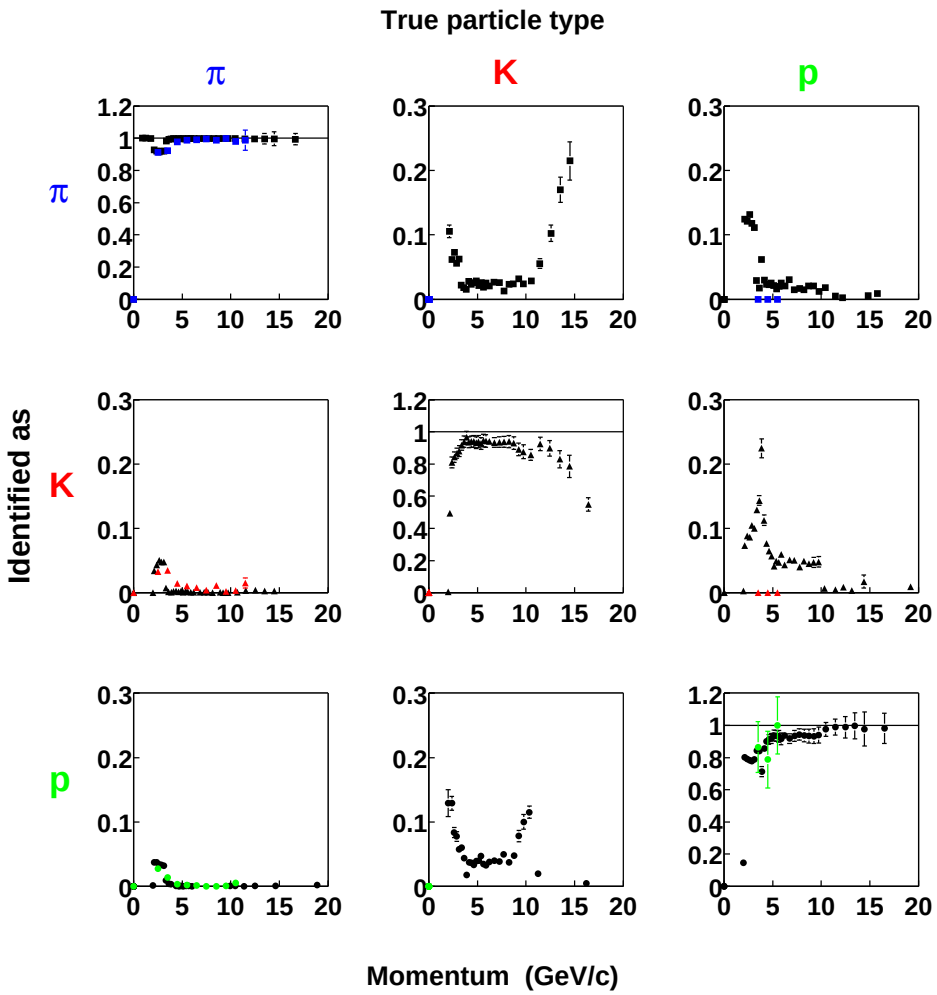

Figure G.1: Momentum distributions of the P-matrix (the number of tracks per a detector half is 1.); the colored points denote results of the experimental data, and those of MC are superimposed as the black points.

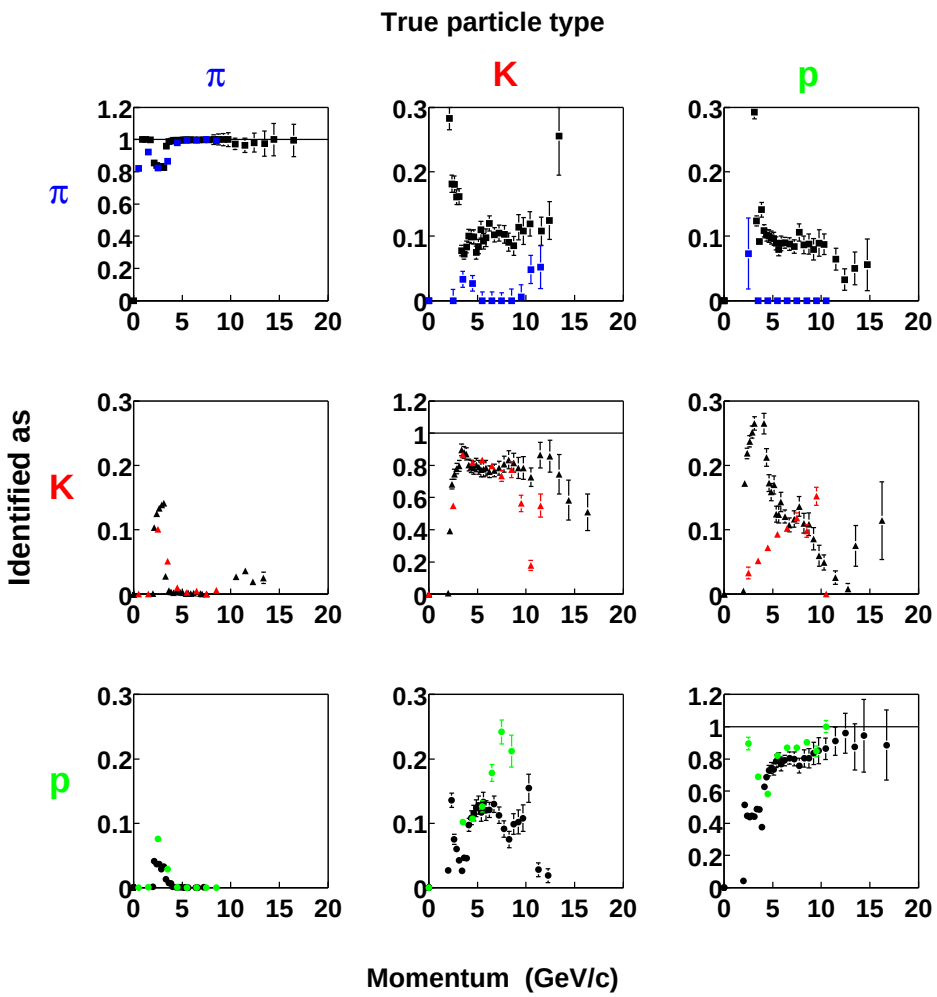

Figure G.2: Momentum distributions of the P-matrix (the number of tracks per a detector half is 2.); the colored points denote results of the experimental data, and those of MC are superimposed as the black points.

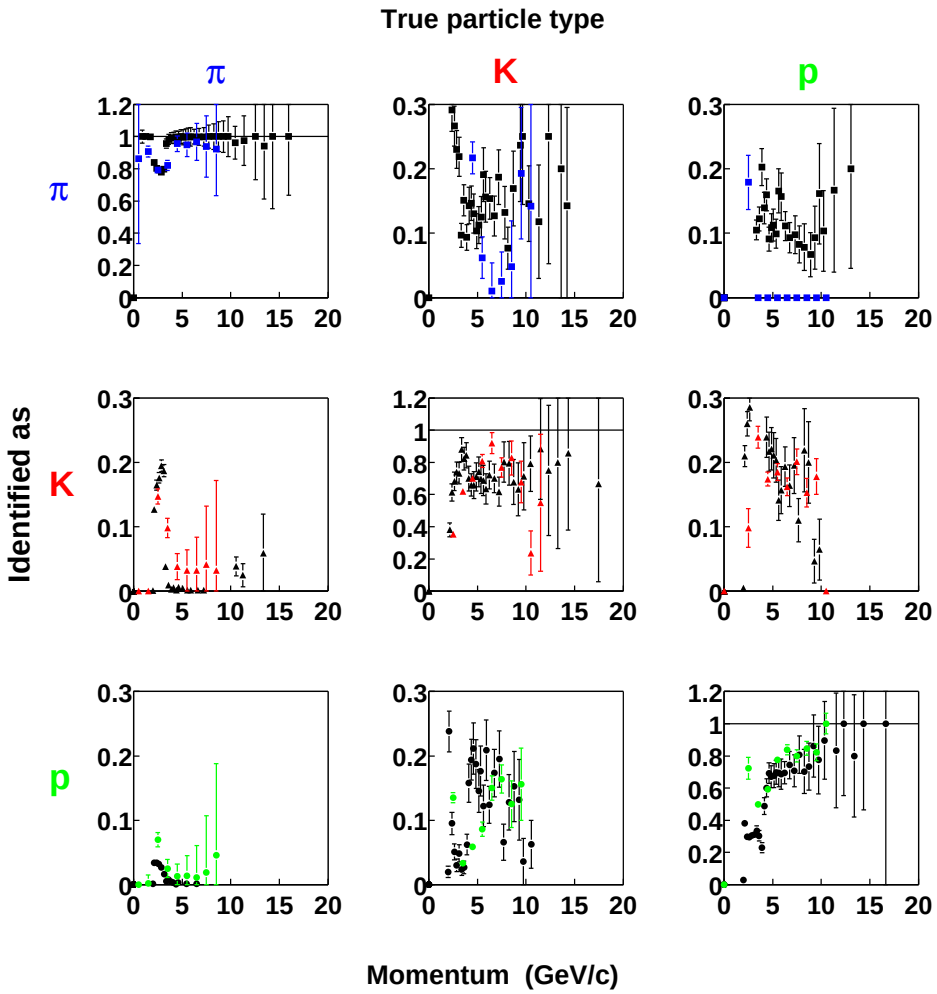

Figure G.3: Momentum distributions of the P-matrix (the number of tracks per a detector half is bigger than 2.); the colored points denote results of the experimental data, and those of MC are superimposed as the black points.

Bibliography

[1] A. A. Sokolov and I. M. Ternov, *On polarization and spin effects in the theory of synchrotron radiation*, Phys. Dokl. **8** (1964) 1203–1205.

[2] K. Ackerstaff et al., *Hermes spectrometer*, Nucl. Instrum. Meth. **A417** (1998) 230–265.

[3] T. Ypsilantis and J. Seguinot, *Theory of ring imaging cerenkov counters*, Nucl. Instrum. Meth. **A343** (1994) 30.

[4] E.Cisbani et.al, *Proposal for a dual radiator rich for hermes*, HERMES Internal Report **97-003**.

[5] V. Dzhordzhadze and R. Kaiser, *A dual radiator rich detector for the hermes experiment.* In *Protvino 1998, High energy spin physics* 609-611.

[6] E. Cisbani, *The dual radiator rich for the hermes experiment at desy*, Nucl. Phys. Proc. Suppl. **78** (1999) 366–371.

[7] M. Yokoyama H. Yokogawa, *Hydrophobic silica aerogel*, Journal of Non-Crystalline Solids **186** (1995) 23.

[8] H. Kawai et al., *Tests of a silica aerogel cerenkov counter*, Nucl. Instrum. Meth. **A228** (1985) 314–322.

[9] G. Poelz and R. Riethmuller, *Preparation of silica aerogel for cerenkov counters*, Nucl. Instr. Meth. **195** (1982) 491.

[10] I. Adachi et al., *Study of a threshold cerenkov counter based on silica aerogels with low refractive indices*, Nucl. Instrum. Meth. **A355** (1995) 390–398.

[11] J. Kanesaka, *Measurements of the properties of silica aerogel tiles for hermes rich*, HERMES Internal Report **98-061**.

[12] E. Aschenauer et al., *Optical characterization of n = 1.03 silica aerogel used as radiator in the rich of hermes*, Nucl. Instrum. Meth. **A440** (2000) 338.

[13] P. Geiger, *Measurement of fragmentation functions at hermes*, HERMES Internal Report **98-005**.

[14] F. Sato, *Study of the rich mirror reflectivity – non-linearity between the reflectivity and the pmt hit numbers*, HERMES Internal Report **00-011**.

[15] N. Akopov et al., *The hermes dual-radiator ring imaging cerenkov detector.* DESY-00-190.

[16] Y. Sakemi, *Dual radiator rich of hermes for pi, k, p identification*, Nucl. Instrum. Meth. **A453** (2000) 284–288.

[17] Dirk De Schepper, *Particle identification with the hermes rich detector: Description of the different approaches.*, HERMES Internal Report **98-008**.

[18] P. Carter, *The aerogel radiator of the hermes rich*, Nucl. Instrum. Meth. **A433** (1999) 392.

[19] D. Ryckbosch, *The hermes rich detector*, Nucl. Instrum. Meth. **A433** (1999) 98.

[20] R. Kaiser, *Conventions for the hermes rich particle identification*, HERMES Internal Report **99-010**.

[21] S. Bernreuther, *private communication* (2001).

[22] K. Negodaeva, *The pid efficiency of the hermes rich and the irt method*, HERMES Internal Report **00-028**.